

NUMERICAL COMPUTATION OF ELECTROMAGNETIC SCATTERING BY INHOMOGENEOUS PENETRABLE BODIES

AD A 073143

DDC FILE COPY

RADC-TR-79-172
Phase Report
July 1979

12



LEVEL H

NUMERICAL COMPUTATION OF ELECTROMAGNETIC SCATTERING BY INHOMOGENEOUS PENETRABLE BODIES

University of Mississippi

S. Govind
D. R. Wilton

APPROVED FOR PUBLIC RELEASE; DISTRIBUTION UNLIMITED

DDC
RECEIVED
AUG 27 1979
RECEIVED
A

ROME AIR DEVELOPMENT CENTER
Air Force Systems Command
Griffiss Air Force Base, New York 13441

79 08 27 038

This report has been reviewed by the RADC Information Office (OI) and is releasable to the National Technical Information Service (NTIS). At NTIS it will be releasable to the general public, including foreign nations.

RADC-TR-79-172 has been reviewed and is approved for publication.

APPROVED:



* JOHN H. EDWARDS, Jr.
Project Engineer

APPROVED:



JOSEPH J. NARESKY
Chief, Reliability & Compatibility Division

FOR THE COMMANDER:



JOHN P. HUSS
Acting Chief, Plans Office

If your address has changed or if you wish to be removed from the RADC mailing list, or if the addressee is no longer employed by your organization, please notify RADC (RBCA) Griffiss AFB NY 13441. This will assist us in maintaining a current mailing list.

Do not return this copy. Retain or destroy.

UNCLASSIFIED

SECURITY CLASSIFICATION OF THIS PAGE (When Data Entered)

REPORT DOCUMENTATION PAGE		READ INSTRUCTIONS BEFORE COMPLETING FORM	
1. REPORT NUMBER RADC-TR-79-172	2. GOVT ACCESSION NO.	3. RECIPIENT'S CATALOG NUMBER 19	
4. TITLE (and Subtitle) NUMERICAL COMPUTATION OF ELECTROMAGNETIC SCATTERING BY INHOMOGENEOUS PENETRABLE BODIES.		5. TYPE OF REPORT & PERIOD COVERED Phase Report	
7. AUTHOR(s) S./Govind D. R./Wilton		8. CONTRACT OR GRANT NUMBER(s) F30602-78-C-0148	
9. PERFORMING ORGANIZATION NAME AND ADDRESS University of Mississippi University MS 38677		10. PROGRAM ELEMENT, PROJECT, TASK AREA & WORK UNIT NUMBERS 62702F 233803PH	
11. CONTROLLING OFFICE NAME AND ADDRESS Rome Air Development Center (RBCA) Griffiss AFB NY 13441		12. REPORT DATE July 1979	
14. MONITORING AGENCY NAME & ADDRESS (if different from Controlling Office) Same		13. NUMBER OF PAGES 209	
		15. SECURITY CLASS. (of this report) UNCLASSIFIED	
		15a. DECLASSIFICATION DOWNGRADING SCHEDULE N/A	
16. DISTRIBUTION STATEMENT (of this Report) Approved for public release; distribution unlimited.			
17. DISTRIBUTION STATEMENT (of the abstract entered in Block 20, if different from Report) Same			
18. SUPPLEMENTARY NOTES RADC Project Engineer: John H. Edwards, Jr. (RBCA)			
19. KEY WORDS (Continue on reverse side if necessary and identify by block number) Antenna Theory Mathematics Electrical Engineering Radio Frequency Currents			
20. ABSTRACT (Continue on reverse side if necessary and identify by block number) Different approaches for studying scattering by inhomogeneous dielectric bodies are considered. The unimoment method, a differential equation approach, and the integral equation approach are discussed in detail. The integral equation approach with unknown equivalent surface currents is selected for further study. For this formulation layered inhomogeneities result in an overall system matrix which is block-tridiagonal, the solution of which can be obtained through an iterative procedure. Such an iterative procedure reduces the computer core storage requirement as compared to a simultaneous solution of the unknown			

DD FORM 1 JAN 73 1473

UNCLASSIFIED

SECURITY CLASSIFICATION OF THIS PAGE (When Data Entered)

79 08 27 038

UNCLASSIFIED

SECURITY CLASSIFICATION OF THIS PAGE(When Data Entered)

Item 20 (Cont'd)

surface currents on the interfaces. The procedure is tested by applying it first to solve for the surface currents on layered spheres and comparing the results to an exact eigen-function solution. The procedure is then extended to permit the determination of the current on a missile in the presence of a trailing inhomogeneous exhaust plume. The resultant system matrix in this case, though not strictly block-tridiagonal, is again transformed by suitable matrix partitioning into a block-tridiagonal form. The currents on the missile are obtained for selected plume inhomogeneities at various frequencies and angles of incidence.

In the appendix, various possible surface current formulations and the uniqueness of corresponding solutions are discussed.

UNCLASSIFIED

SECURITY CLASSIFICATION OF THIS PAGE(When Data Entered)

TABLE OF CONTENTS

	Page
LIST OF FIGURES	v
Chapter	
I. INTRODUCTION	1
II. SCATTERING BY INHOMOGENEOUS DIELECTRIC CYLINDERS	8
2.1 Unimoment Method for Scattering by Dielectric Cylinders	8
2.2 Interior Problem	14
2.3 Numerical Results of Unimoment Method	30
2.4 A Comparison of Numerical Methods for Application to Missile Plume Problems	33
III. NUMERICAL SOLUTION PROCEDURE FOR SCAT- TERING BY LAYERED DIELECTRIC BODY OF REVOLUTION	43
3.1 Formulation of the Integral Equations	43
3.2 Eigenfunction Solution for a Three-layered Dielectric Sphere	77
3.3 Numerical Results	88
IV. MISSILE PLUME SCATTERING	110
4.1 Block Tridiagonal Formulation for Missile Plume Scattering	110

Chapter	Page
4.2 Boundary Conditions at the Missile-Plume Junction	114
4.3 Numerical Results	121
V. CONCLUSION	161
APPENDIX A. SURFACE CURRENT FORMULATIONS FOR DIELECTRIC SCATTERING PROBLEMS	165
A.1 Surface Integral Equation Formulation	166
A.2 H-Field Formulation	169
A.3 E-Field Formulation	173
A.4 Combined Field Formulation	174
A.5 Application of Various Surface Integral Formulations to TM Scattering by Dielectric Cylinders	181
REFERENCES	196

LIST OF FIGURES

Figure	Page
2.1. Geometry of the scattering problem	9
2.2. Finite element grid scheme for the interior region	16
2.3. Area coordinate representation	19
2.4. Interconnecting nodal arrangement and definition of the connection matrix.	24
2.5. Vector definitions of nodes in an element	27
2.6. Scattering cross-section of a two- layered dielectric circular cylinder	31
2.7. Scattering cross-section of a two- layered dielectric elliptic cylinder	32
2.8. A homogeneous scatterer	36
2.9. A five-layered dielectric scatterer	37
3.1. Two layers of a N-layered dielectric body of revolution	44
3.2. Equivalent problems in the various regions	47
3.3. Linear segmentation of the generating arcs	65
3.4. A three-layered dielectric sphere	78
3.5. Electric and magnetic surface cur- rent distribution on a "vacuum dielectric" sphere. $a_1 = 0.4m$, $a_2 = 0.75m$, $a_3 = 1.0m$, $\lambda_0 = 1.0m$	91

Figure	Page
3.6a. Electric surface current distribution on a homogeneous dielectric sphere. $a_1 = 0.5\text{m}$, $a_2 = 0.75\text{m}$, $a_3 = 1.0\text{m}$, $\lambda_0 = 1.0\text{m}$, $\epsilon_r = 2.0$	92
3.6b. Magnetic current distribution on the homogeneous dielectric sphere in Figure 3.6a	93
3.7a. Electric currents on a sphere for various conductivities	94
3.7b. Magnetic currents for the sphere in Figure 3.7a	95
3.8a. Electric currents on a sphere of high dielectric constant. $k_0 a_1 = 0.06$, $k_0 a_2 = 0.12$, $k_0 a_3 = 0.2$, $\epsilon_r = 80$, $\sigma = 0$, $\lambda_0 = 1.0\text{m}$	96
3.8b. Magnetic currents on the homogeneous sphere of Figure 3.8a	97
3.9a. Electric currents on an inhomogeneous sphere. $k_0 a_1 = 0.4$, $k_0 a_2 = 0.75$, $k_0 a_3 = 1.0$, $\epsilon_{r1} = \epsilon_{r2} = \epsilon_{r3} = 4.0$, $\sigma_1 = 1.0 \text{ S/m}$, $\sigma_2 = 2.0 \text{ S/m}$, $\sigma_3 = 4.0 \text{ S/m}$	99
3.9b. Magnetic currents on the inhomogeneous sphere of Figure 3.9a	100
3.10a. Electric surface current distribution on an inhomogeneous sphere. $a_1 = 0.4\text{m}$, $a_2 = 0.75\text{m}$, $a_3 = 1.0\text{m}$, $\epsilon_{r1} = 2.0$, $\epsilon_{r2} = 3.0$, $\epsilon_{r3} = 4.0$, $\sigma_1 = \sigma_2 = \sigma_3 = 0.0$, $\lambda_0 = 1.0\text{m}$	101
3.10b. Magnetic currents on the inhomogeneous sphere of Figure 3.10a	102

Figure	Page
3.11a. Electric surface current distribution on an inhomogeneous dielectric sphere, $a_1 = 0.5\text{m}$, $a_2 = 0.95\text{m}$, $a_3 = 1.0\text{m}$, $\epsilon_1 = \epsilon_2 = \epsilon_3 = \epsilon_0$, $\sigma_1 = 0.2 \text{ S/m}$, $\sigma_2 = 0.3 \text{ S/m}$, $\sigma_3 = 0.4 \text{ S/m}$, $\lambda_0 = 2\pi\text{m}$	104
3.11b. Magnetic currents on the inhomogeneous sphere in Figure 3.11a.	105
3.12a. Electric surface current distribution on a finite homogeneous dielectric cylinder	106
3.12b. Magnetic surface current distribution on the finite dielectric cylinder of Figure 3.12a	107
3.13a. Electric surface current distribution on a homogeneous dielectric cone-sphere.	108
3.13b. Magnetic currents on the homogeneous cone-sphere of Figure 3.13a.	109
4.1. Geometry of a missile with a trailing plume.	111
4.2a. External equivalence and current expansion scheme for the missile/plume configuration	116
4.2b. Internal equivalence and current expansion scheme for the missile/plume configuration	117
4.3a. Electric current distribution along a missile with a trailing plume of uniform conductivity $\sigma = 0 \text{ S/m}$	122
4.3b. Electric current distribution along a missile with a surrounded plume of uniform conductivity $\sigma = 0 \text{ S/m}$	124
4.4a. Electric current distribution along a missile and trailing plume of uniform conductivity $\sigma = 1000 \text{ S/m}$ under broadside illumination	125

Figure	Page
4.4b. Electric current distribution along a missile and trailing plume of uniform conductivity $\sigma = 1000$ S/m under oblique incidence, $\theta^{\text{inc}} = 30^\circ$	126
4.5. Electric current distribution along a missile and trailing plume of uniform conductivity $\sigma = 0.2$ S/m under broadside illumination	128
4.6. Constant conductivity contours of Chaparral missile plume	131
4.7. Layered approximation to the plume of the Chaparral missile	132
4.8 a-e Electric current distribution on a Chaparral missile, $f = 30$ MHz, $\theta^{\text{inc}} = 30^\circ - 150^\circ$	133- 137
4.9 a-e Electric current distribution on a Chaparral missile, $f = 50$ MHz, $\theta^{\text{inc}} = 30^\circ - 150^\circ$	138- 142
4.10 a-e Electric current distribution on a Chaparral missile, $f = 70$ MHz, $\theta^{\text{inc}} = 30^\circ - 150^\circ$	143- 147
4.11 a-e Electric current distribution on a Chaparral missile, $f = 90$ MHz, $\theta^{\text{inc}} = 30^\circ - 150^\circ$	148- 152
4.12 a-e Electric current distribution on a Chaparral missile, $f = 100$ MHz, $\theta^{\text{inc}} = 30^\circ - 150^\circ$	153- 157
4.13. Equivalent admittance variation along the axis of the plume	160

Figure	Page
A.1. A homogeneous dielectric scatterer	167
A.2. External equivalence	167
A.3. Internal equivalence	167
A.4. Exterior equivalence with assumed non-zero fields in the exterior region	180
A.5. Interior equivalence with assumed non-zero fields in the interior region	180
A.6. Exterior equivalence with interior medium parameters (μ_d, ϵ_d)	180
A.7. Interior equivalence with exterior medium parameters (μ_e, ϵ_e)	180
A.8. Circuit analogy and permissible values of α/η_e for exterior equivalence	182
A.9. Circuit analogy and permissible values of β/η_d for interior equivalence	183
A.10. Geometry of a homogeneous dielectric cylinder	185
A.11. Linear segmentation of the cross-section of the cylinder	187
A.12. Electric and magnetic current distribution along a circular cylinder excited by a TM polarized incident wave, $a = 0.1\lambda_0, \epsilon_r = 2.0$. . .	192
A.13. Electric and magnetic current distribution along a square cylinder excited by a TM polarized wave, $k_0(2a) = 2.0, \epsilon_r = 2.56$	193
A.14. Determinant of the moment matrix vs. ka of a square cylinder	194

CHAPTER I

INTRODUCTION

The object of this work is to use numerical methods to solve electromagnetic field problems involving scattering from rather arbitrarily shaped inhomogeneous penetrable bodies. While our aim is to analyze a missile in the presence of an electrically inhomogeneous exhaust plume, the techniques discussed here are useful in other areas of electromagnetics, such as scattering by rain drops, power absorption in biological tissues, dielectric lenses, etc. A primary requirement of any numerical method is that the technique should be capable of simulating the actual physical situation as closely as possible, while simultaneously providing an efficient method of solution. For a numerical study of scattering by inhomogeneous dielectric bodies, one must choose among a variety of techniques, all of which can be said to fall into one of the following two categories: (a) Integral equation formulations and (b) Differential equation methods. The usual surface and volume integral equation formulations with numerical solution by the method of moments [1] and the extended boundary condition approach [2] fall

into the category of (a) while finite difference methods and the unimoment method [3] fall into (b). Thus a wide variety of approaches are available. Some of the main features of each of these methods are given in the following.

The volume integral equation is based on relating the polarization current in terms of the total field, comprising the incident field and the scattered field. By associating an unknown current coefficient with each point inside the region, the integral equation is converted into a matrix equation which can be easily solved for the unknown coefficients. Since the region of the scatterer is represented point by point, an arbitrary inhomogeneity and shape is easily handled in this approach. The approach, however, leads to very large matrices which makes the method unattractive due to the limited core storage on the computer.

The integral equation approach is well suited either for homogeneous penetrable bodies or for a body either modeled by or made up of layers of homogeneous regions. The usual procedure in this case is to set up the coupled integral equations in terms of equivalent electric and magnetic currents on the surfaces of the homogeneous region. By expanding the unknown currents in terms of suitable basis functions and adopting suitable testing functions, the coupled integral equations are reduced to a matrix equation for the unknown coefficients of the basis functions.

For a body made up of a large number of layers or for an inhomogeneous body modeled as being made up of layers of homogeneous regions, the above approach can lead to very large-sized matrices due to a simultaneous solution of the equivalent currents on all the layers. Since the fields induced in any region between two layers are due to the equivalent currents on adjacent layers, the resulting matrix is block tridiagonal. This property, as recognized by Pogorzelski [4], yields an iterative procedure for solving for the currents on the outermost layer in terms of the currents on the inner layers. Such an iterative procedure has the advantage that the sizes of the matrices involved in the iteration are much smaller than the overall matrix size that would be required if the currents on all layers were to be solved simultaneously. The surface equivalence approach is, in principle, applicable to all (layered) inhomogeneous scatterers, regardless of shape.

The extended boundary condition approach proposed by Waterman [2] expresses the fields in terms of integrals over surfaces separating the homogeneous regions around the scatterer. However, one uses here the fact that in all regions complementary to those in which the equivalence is valid, the fields must vanish. Within these null field regions, the integral expressions for the fields are expanded in spherical

(cylindrical) harmonics of the standing wave type for interior three-dimensional (two-dimensional) regions and of the outgoing type for exterior regions. Since the fields vanish, the coefficients of the harmonics must also vanish and one obtains a set of equations, each of which involves integrals over the equivalent sources on the surface. The surface sources, both electric and magnetic, are usually expanded in spherical (cylindrical) harmonics as well and this eliminates one of the surface sources, thus reducing the number of unknowns. In the literature, the extended boundary condition approach is also known as the T-matrix approach. Peterson and Ström [5] have extended this approach to multilayered dielectric scatterers and Ström [6] has further extended the approach to multiple inhomogeneous scatterers. Since the method depends on the object having an interior region in which a circumscribed sphere (circle) can be placed, the method is better suited for nearly spherical (cylindrical) bodies than for thin scatterers.

The unimoment technique developed by Mei [3] and extended by Chang [7] and Morgan [8] essentially studies the scattering problem through a differential equation formulation. According to this approach, a spherical (cylindrical) region surrounds the three-dimensional (two-dimensional) scatterer. The minimum radius of this region should be so

as to totally enclose the scatterer so that the scattered fields in the exterior region can be expanded in terms of outgoing spherical (cylindrical) harmonics. The incident field, of course, may be expanded in terms of incoming harmonics. A wave equation for an appropriate field quantity is next solved for in the interior region. The boundary conditions for the tangential fields are then enforced across the spherical (cylindrical) boundary. This results in a set of equations which determine the coefficients of the unknown scattered fields. As one notes, the major effort involved in this approach is in solving the differential equation in the interior region. Either a finite difference approach or the finite element method [9], a numerical approach for solving differential equations that has been highly developed by structural engineers, can then be utilized to solve this differential equation. In the latter approach, the interior region is typically divided into a number of triangular sections called elements. Over each element the field is represented by suitable expansion functions that express the field within an element as a function which interpolates the value of the field at the nodes of the element. By minimizing a stationary formula associated with the differential operator with respect to the nodal coefficients, one obtains a matrix equation for the nodal field values on the interior

in terms of the field values at the nodes lying on the spherical (cylindrical) boundary. Then using the spherical (cylindrical) modes as basis functions to excite the electric fields at the boundary, one obtains interior fields for each distinct mode of the harmonics. Orthogonality of the basis functions enables one to determine the interior fields in terms of the scattered fields. Equating the exterior and interior tangential magnetic fields at the boundary yields a matrix equation which determines the scattered field coefficients. An inherent feature of the matrix so obtained is that it is banded and an efficient utilization of this property allows one to solve problems involving a rather large number of unknowns. Furthermore, just as one can express the interior fields in terms of interpolatory functions over each element, one can similarly approximate the spatial variation of the physical parameters viz., the permittivity and permeability, by means of the same interpolatory functions. This latter feature of the unimoment method enables one to solve for fields from arbitrary inhomogeneous (i.e. not necessarily layered) scatterers. As with the extended boundary condition approach, the unimoment method is more suitable for scatterers which are almost circular or spherical in shape.

From the above discussion it is apparent that the choice

of a method should be made from the point of view of simplicity, accuracy, and efficiency of the method as it applies to the geometry and scatterer in question. In order to more clearly define some of the considerations involved in the choice of the method, we consider the application of the unimoment method to scattering from two-dimensional layered dielectric cylinders in Chapter II. We also note some of the advantages of a local as compared to a global coordinate formulation. In Chapter II the unimoment method approach is compared with the iterative solution procedure for the surface integral formulation for scattering by layered dielectric cylinders. Chapter III deals with the application of the iterative solution procedure for the surface integral equation to layered bodies of revolution. In Chapter IV, the approach is extended to treat missile-plume problems, which are also reduced to a block-tridiagonal form.

In the course of this work, the equivalence principle is used extensively. One normally uses the equivalence principle to set up coupled integral equations for unknown electric and/or magnetic currents. In Appendix A, different types of integral equation formulations are considered. The discussions there parallel and extend slightly the work in this area by Harrington and Mautz [10].

CHAPTER II

SCATTERING BY INHOMOGENEOUS DIELECTRIC CYLINDERS

In this chapter, we present a comparative study of the unimoment method and the iterative solution procedure. Since the principal features of the methods when applied to a general problem can be illustrated through specific examples for which alternative solutions are available, we consider herein scattering by layered dielectric cylinders. In Section 2.1 a brief description of the unimoment method is given. While we follow essentially the approach of [7], we do, however, present a simpler representation of the unimoment matrix than is found there. Sec. 2.2 gives some insight into the iterative solution of the surface integral method which leads to a block-tridiagonal moment matrix. A comparison with the unimoment method is then made to point out the applicability and limitations of the two techniques for general problems involving inhomogeneous dielectric bodies.

2.1 Unimoment Method for Scattering from Dielectric Cylinders

Fig. 2.1 shows an arbitrary cylindrical scatterer upon which a plane wave is incident. We shall restrict our

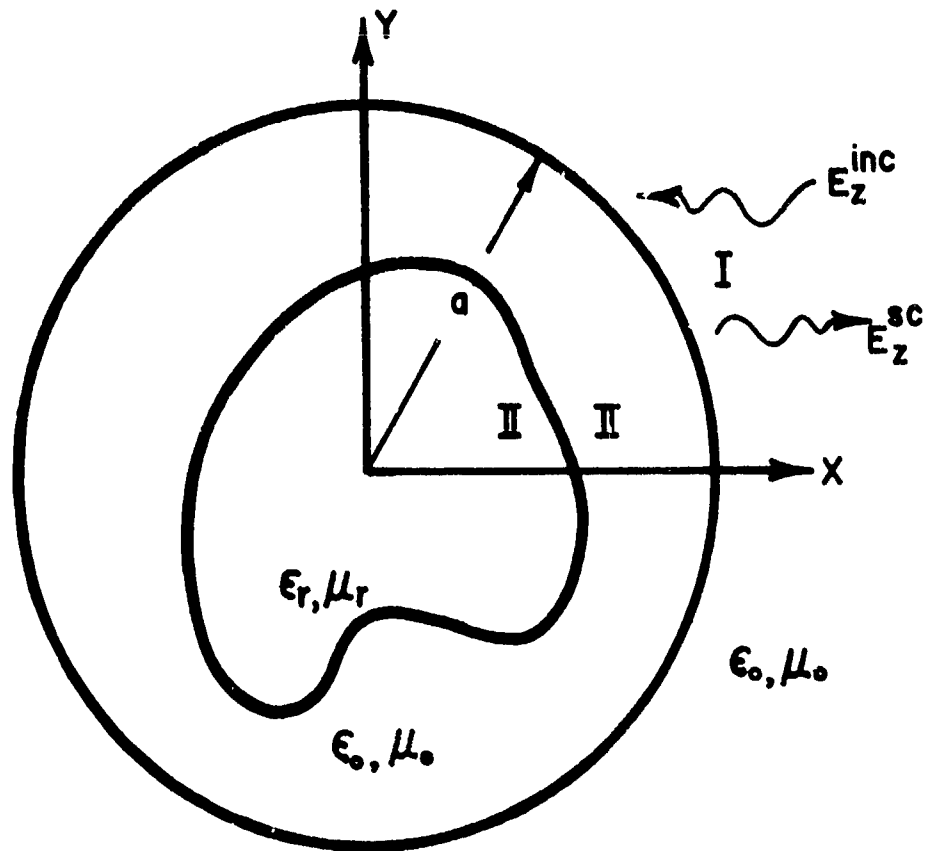


Figure 2.1. Geometry of the scattering problem.

discussions herein to a TM polarized incident wave. The reader is referred to [7] for the TE polarization case. The scatterer is enclosed by a circle of radius a . Assuming that the axis of the cylinder is in the z direction, let $E_z^{II}(r, \phi)$ be the total field inside the circle, $E_z^{inc}(r, \phi)$ the incident field, and $E_z^{sc}(r, \phi)$ the scattered field outside the circle. The tangential components of the fields must be continuous across the circular boundary. Thus, we have

$$E_z^{II}(a, \phi) = E_z^{inc}(a, \phi) + E_z^{sc}(a, \phi), \quad (2.1)$$

$$\left. \frac{\partial E_z^{II}}{\partial r} \right|_{r=a} = \left. \frac{\partial E_z^{inc}}{\partial r} \right|_{r=a} + \left. \frac{\partial E_z^{sc}}{\partial r} \right|_{r=a}. \quad (2.2)$$

Since $E_z^{sc}(r, \phi)$ is a scattered field, we express it in terms of outgoing cylindrical harmonics as

$$E_z^{sc}(r, \phi) = \sum_{n=0}^{\infty} H_n^{(2)}(k_0 r) \left\{ A_n \cos n\phi + B_n \sin n\phi \right\}, \quad (2.3)$$

where $H_n^{(2)}(x)$ is the Hankel function of the second kind, $k_0 = \omega \sqrt{\mu_0 \epsilon_0}$, is the free space propagation constant, A_n and B_n are arbitrary constants to be determined. Since the incident field can also be expanded in a series of cylindrical harmonics, let us therefore express the field of

region II evaluated on the circular boundary in terms of cylindrical harmonics. Thus, we have

$$E_z^{II}(a, \phi) = \sum_{n=0}^{\infty} (C_n \cos n\phi + D_n \sin n\phi). \quad (2.4)$$

Each Fourier harmonic in (2.4) can be thought of as representing the evaluation on the boundary of one term of a complete set of linear independent partial fields, $\psi_n^{(c)}(r, \phi)$ which satisfy

$$\nabla^2 \psi_n^{(c)}(r, \phi) + k_o^2 \epsilon_r(r, \phi) \psi_n^{(c)}(r, \phi) = 0, \quad (2.5)$$

and the boundary conditions

$$\psi_n^c(a, \phi) = \cos n\phi, \quad (2.6a)$$

$$\psi_n^s(a, \phi) = \sin n\phi. \quad (2.6b)$$

Thus the interior field is given by

$$E_z^{II}(r, \phi) = \sum_{n=0}^{\infty} C_n \psi_n^c(r, \phi) + D_n \psi_n^s(r, \phi). \quad (2.7)$$

We may determine $\psi_n^{(c)}(r, \phi)$ with the above boundary conditions by solving (2.5) through any of the standard techniques of

solving the second-order differential equation. We shall be adopting the finite element method, a discussion of which is reserved until the next section. Using (2.3) and (2.4) in (2.1), we get

$$\sum_{n=0}^{\infty} (C_n \cos n\phi + D_n \sin n\phi) = E_z^{\text{inc}}(a, \phi) + \sum_{n=0}^{\infty} H_n^{(2)}(k_0 a) [A_n \cos n\phi + B_n \sin n\phi]. \quad (2.8)$$

With the use of (2.3) and (2.7) in (2.2), we obtain

$$\sum_{n=0}^{\infty} \left[C_n \frac{\partial \psi_n^c}{\partial r} \Big|_{r=a} + D_n \frac{\partial \psi_n^s}{\partial r} \Big|_{r=a} \right] = \frac{E_z^{\text{inc}}}{\partial r} \Big|_{r=a} + \sum_{n=1}^{\infty} k_0 H_n^{(2)'}(k_0 a) [A_n \cos n\phi + B_n \sin n\phi]. \quad (2.9)$$

Invoking standard orthogonality relationships we obtain from (2.8)

$$C_n = A_n H_n^{(2)}(k_0 a) + f_n^c, \quad (2.10a)$$

$$D_n = B_n H_n^{(2)}(k_0 a) + f_n^s, \quad (2.10b)$$

where

$$f_n^c = \frac{1}{\pi} \int_0^{2\pi} E_z^{\text{inc}}(a, \phi) \cos n\phi \, d\phi, \quad (2.11)$$

$$f_n^s = \frac{1}{\pi} \int_0^{2\pi} E_z^{\text{inc}}(a, \phi) \sin n\phi \, d\phi. \quad (2.12)$$

Substituting (2.10) - (2.12) in (2.9), we obtain finally

$$\begin{aligned} & \sum_{n=0}^{\infty} \left[A_n \left\{ H_n^{(2)}(k_0 a) \frac{\partial \psi_n^c}{\partial r} \Big|_{r=a} - k_0 H_n^{(2)'}(k_0 a) \cos n\phi \right\} \right. \\ & \quad \left. + B_n \left\{ H_n^{(2)}(k_0 a) \frac{\partial \psi_n^s}{\partial r} \Big|_{r=a} - k_0 H_n^{(2)'}(k_0 a) \sin n\phi \right\} \right] \\ & = \frac{\partial E_z^{\text{inc}}}{r} \Big|_{r=a} - \sum_{n=0}^{\infty} \left[f_n^c \frac{\partial \psi_n^c}{\partial r} \Big|_{r=a} + f_n^s \frac{\partial \psi_n^s}{\partial r} \Big|_{r=a} \right]. \end{aligned} \quad (2.13)$$

In computations, the summation in (2.13) must be truncated to N terms. The choice of N is generally slightly greater than $k_0 a$. To obtain a matrix equation for the unknown coefficients A_n , B_n , (2.13) may be multiplied by $\cos n\phi$ ($n = 0, 1, 2, \dots, N$) and $\sin n\phi$ ($n = 1, 2, \dots, N$), integrated over the interval 0 to 2π . (Note that this is equivalent to

expanding the continuity equation (2.2) into Fourier modes). Once A_n , B_n have been computed the scattered field is easily computed from (2.3).

2.2 Interior Problem

The interior field satisfies the differential equation (2.5). Since the exact solution to the inhomogeneous equation is possible only for limited types of inhomogeneity, we resort to the so-called finite element method [9] for solving for ψ_n . In this approach, the solution for ψ_n is obtained by minimizing a variational functional associated with the differential equation. The interior of the circle of radius a is usually divided into a number of triangular subregions which are known as "elements". The function ψ_n is expanded over each element in terms of suitable functions called "trial functions". The values of the trial functions are specified at certain points (nodes) on the triangles. Typically these nodes are at the vertices of the triangular elements, but in higher order schemes [9], may also be at, say, the mid-points of the sides of the triangles. By using the trial functions over each element and minimizing the functional with respect to the nodal values within an element, one obtains a matrix equation. This matrix equation may be then solved to determine ψ_n at the nodal points.

For TM polarized waves, ψ_n satisfies

$$\nabla^2 \psi_n(r, \phi) + k_0^2 \epsilon_r(r, \phi) \psi_n(r, \phi) = 0,$$

where $\psi_n(r, \phi) = E_z(r, \phi)$. The solution to this equation is the same as one would obtain by minimizing the functional

$$I = \iint_S [|\nabla \psi_n|^2 - k_0^2 \epsilon_r(r, \phi) \psi_n^2(r, \phi)] ds, \quad (2.14)$$

where S corresponds to the region over which (2.5) is valid. We divide the region S into a number of triangular regions (Fig. 2.2). Let ψ_{n_i} , $i = 1, 2, \dots, K + K'$, be the nodal values, where K is the total number of nodes inside the region S and K' is the total number of nodes on the artificial circle. Approximate ψ_n by a linear function over each triangle. Minimizing the functional I in (2.14) with respect to ψ_{n_i} , $i = 1, 2, \dots, K$, one obtains

$$QU = TU', \quad (2.15)$$

where

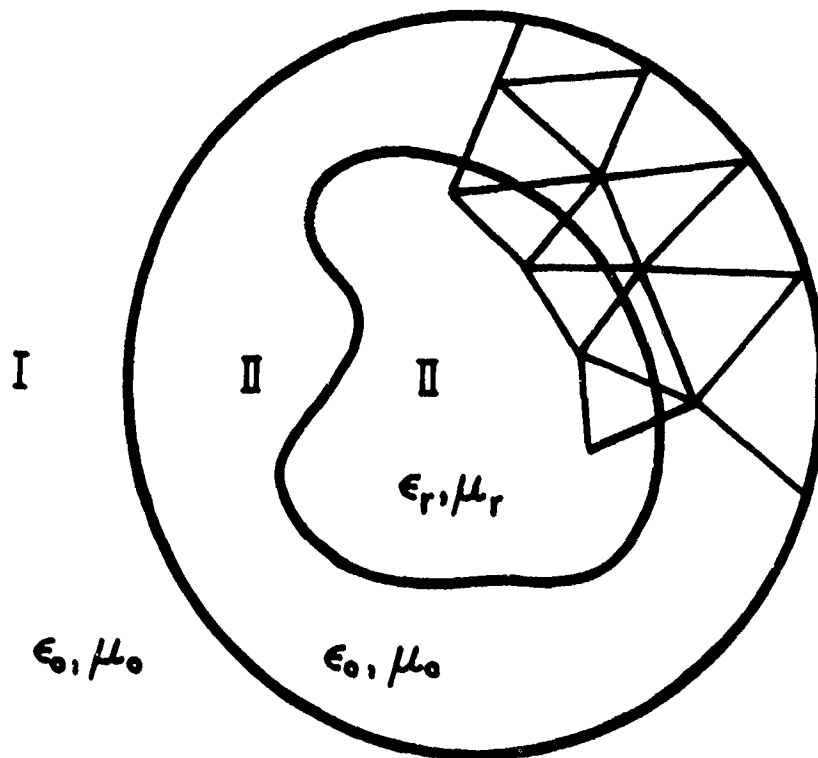


Figure 2.2. Finite element grid scheme for the interior region.

$$U = \begin{bmatrix} \psi_{n_1} \\ \psi_{n_2} \\ \vdots \\ \psi_{n_K} \end{bmatrix}, \quad U' = \begin{bmatrix} \psi_{n_{K+1}} \\ \psi_{n_{K+2}} \\ \vdots \\ \psi_{n_{K+K'}} \end{bmatrix}$$

and Q and T are the coefficient matrices obtained from (2.14) over each element. Since ψ_{n_i} , $i = K+1, K+2, \dots, K+K'$, are known for each mode n , one can solve for U from (2.15). Once ψ_n is known, $\left. \frac{\partial \psi_n}{\partial r} \right|_{r=a}$ is evaluated along the artificial circle. Having obtained the numerical derivative of ψ_n on the circle ($r = a$), we may then evaluate the scattered field coefficients A_n, B_n from (2.13).

The remaining problem is thus the evaluation of the elements of the matrices Q and T . It is in this step that we follow a slightly different derivation than that of Chang and Mei [7]. If $\phi = \psi_n$ is the field in any element corresponding to the n^{th} mode, Chang and Mei express the assumed linear variation of this field in terms of a fixed global (x, y, z) coordinate system as

$$\phi = ax + by + c, \quad (2.16)$$

where $a, b,$ and c are the expansion coefficients to be

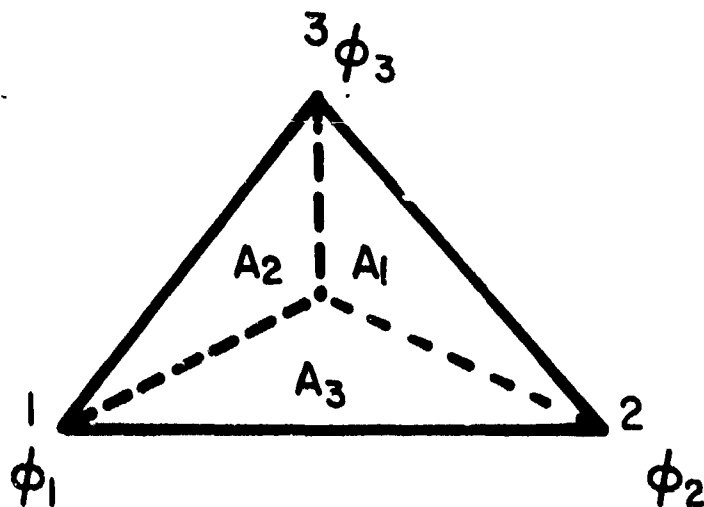
determined. If (1,2,3) are the nodes of the triangular element and ϕ_1, ϕ_2, ϕ_3 are the respective nodal values, then the expansion coefficients a, b, c for this element can be easily found in terms of ϕ_1, ϕ_2, ϕ_3 as

$$\begin{bmatrix} a \\ b \\ c \end{bmatrix} = \begin{bmatrix} x_1 & y_1 & 1 \\ x_2 & y_2 & 1 \\ x_3 & y_3 & 1 \end{bmatrix}^{-1} \begin{bmatrix} \phi_1 \\ \phi_2 \\ \phi_3 \end{bmatrix}. \quad (2.17)$$

An alternative and simpler representation for ϕ is in terms of a local coordinate system, wherein ϕ is expressed in terms of area coordinates [9]. Referring to Fig. 2.3, the field in the element is written in terms of area coordinates as

$$\phi = \frac{1}{A}(\phi_1 A_1 + \phi_2 A_2 + \phi_3 A_3), \quad (2.18)$$

where A is the total area of the triangle and $A_m, m = 1, 2, 3$ are the sub-areas shown in Fig. 2.3. It should be noted herein that the global coordinate and local coordinate representations are two different ways of expressing the assumed linear variation. The two representations themselves can be related to one another. The relationship between the two can be obtained as



$$A = A_1 + A_2 + A_3$$

Figure 2.3. Area coordinate representation.

$$\begin{bmatrix} 1 \\ x \\ y \end{bmatrix} = \begin{bmatrix} 1 & 1 & 1 \\ x_1 & x_2 & x_3 \\ y_1 & y_2 & y_3 \end{bmatrix} \begin{bmatrix} \frac{A_1}{A} \\ \frac{A_2}{A} \\ \frac{A_3}{A} \end{bmatrix}, \quad (2.19)$$

$$\begin{bmatrix} \frac{A_1}{A} \\ \frac{A_2}{A} \\ \frac{A_3}{A} \end{bmatrix} = \begin{bmatrix} P_{23} & Y_{23} & -X_{23} \\ P_{31} & Y_{31} & -X_{31} \\ P_{12} & Y_{12} & -X_{12} \end{bmatrix} \begin{bmatrix} 1 \\ x \\ y \end{bmatrix}, \quad (2.20)$$

where $P_{mn} = P_\ell = \frac{1}{2A} [x_m y_n - x_n y_m]$,

$$Y_{mn} = Y_\ell = \frac{1}{2A} [y_m - y_n]$$

$$X_{mn} = X_\ell = \frac{1}{2A} [x_m - x_n], \quad \ell, m, n = 1, 2, 3$$

and (x_i, y_i) , $i = 1, 2, 3$, are the coordinates of the nodes of the element. Since the integrand of the functional I in (2.14) involves derivatives, we note

$$\frac{\partial}{\partial x} \left[f \left(\frac{A_1}{A}, \frac{A_2}{A}, \frac{A_3}{A} \right) \right] = \sum_{i=1}^3 \frac{1}{A} y_i \frac{\partial f}{\partial A_i}, \quad (2.21)$$

$$\frac{\partial}{\partial y} \left[f \left(\frac{A_1}{A}, \frac{A_2}{A}, \frac{A_3}{A} \right) \right] = \sum_{i=1}^3 -\frac{1}{A} X_i \frac{\partial f}{\partial A_i}, \quad (2.22)$$

The functional I in (2.14) over the element is

$$I_{\Delta_{123}} = \iint_{\Delta_{123}} [|\nabla\phi|^2 - k_o^2 \epsilon_r \phi^2] ds. \quad (2.23)$$

We note that

$$\nabla\phi = \frac{\partial\phi}{\partial x} \hat{x} + \frac{\partial\phi}{\partial y} \hat{y}.$$

Using (2.18), (2.21) and (2.22), we get

$$\nabla\phi = \left[\sum_{i=1}^3 \frac{\phi_i}{A} Y_i \right] \hat{x} + \left[\sum_{i=1}^3 \frac{\phi_i}{A} X_i \right] \hat{y}. \quad (2.24a)$$

Hence

$$|\nabla\phi|^2 = \left[\sum_{i=1}^3 \frac{\phi_i}{A} Y_i \right]^2 + \left[\sum_{i=1}^3 \frac{\phi_i}{A} X_i \right]^2 \quad (2.24b)$$

Minimizing $I_{\Delta_{123}}$ with respect to ϕ_1 , one has

$$\frac{\partial I_{\Delta_{123}}}{\partial \phi_1} = \frac{\partial}{\partial \phi_1} \iint_{\Delta_{123}} [|\nabla\phi|^2 - k_o^2 \epsilon_r \phi^2] ds. \quad (2.25)$$

Substituting (2.24) and (2.18) into the above and noting the following integrals,

$$\iint_{\Delta_{123}} \frac{A_i}{A} ds = \frac{A}{3}, \quad i = 1, 2, 3$$

$$\iint_{\Delta_{123}} A_i A_j ds = \frac{A^3}{12}, \quad i \neq j$$

$$\iint_{\Delta_{123}} (A_i)^2 ds = \frac{A^3}{6}, \quad i = 1, 2, 3$$

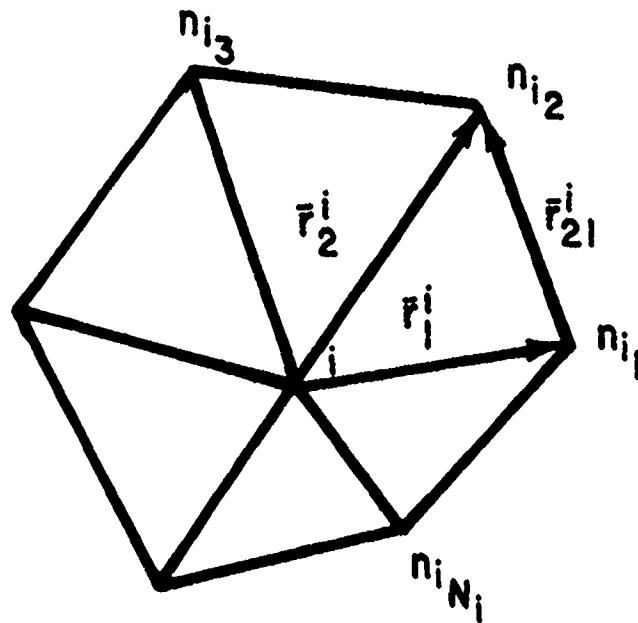
one obtains

$$\begin{aligned} \frac{\partial I_{\Delta_{123}}}{\partial \phi_1} &= 2 \left(\sum_{m=1}^3 \frac{\phi_m}{A} Y_m \right) Y_1 + 2 \left(\sum_{m=1}^3 \frac{\phi_m}{A} X_m \right) X_1 \\ &\quad - \frac{k_o^2 A \epsilon_r}{6} (2\phi_1 + \phi_2 + \phi_3). \end{aligned} \quad (2.26)$$

Herein we have assumed that ϵ_r is constant over the element. If ϵ_r varies over the element, then one can expand ϵ_r in terms of a suitable polynomial (in the area coordinates) and proceed as above to evaluate the second term in (2.25).

If there are p triangles around node 1, then one has to evaluate the integral in (2.25) over each of these p triangles to obtain a single element of the matrix Q or T .

From the above it is clear that a proper bookkeeping of the nodes that make up an element of the finite element mesh is mandatory. However, it is the nodes which correspond to the elements of the matrices Q and T . Accordingly, it is the interconnecting nodal arrangement which plays a key role as compared to the nodes that make up each element. Computationally, one could search through a matrix which lists the nodes making up an element and find which elements of the mesh contribute to which elements of the matrix. This appears to be the procedure adopted in [7]. An alternative approach that is computationally more efficient, however, is to define the elements through a connection matrix $N = [n_{ij}]$, whose elements are the nodal numbers of the j^{th} node (numbered counter-clockwise) connected to node i (see Fig. 2.4). Such an approach has the advantage of immediately identifying the interconnecting nodes. It also makes the numbering of the elements superfluous, as we shall see. Expanding out the terms in (2.26), we obtain



i th row
of connection
matrix

$$\left[\begin{array}{ccccccc} n_{i1} & n_{i2} & n_{i3} & \cdots & n_{iN_i} & 0 & \cdots & 0 \end{array} \right]$$

Figure 2.4. Interconnecting nodal arrangement and definition of the connection matrix.

$$\begin{aligned}
\frac{\partial I_{123}}{\partial \phi_1} &= \frac{2}{A} (x_1^2 + y_1^2) \phi_1 \\
&+ \frac{2}{A} [(x_1 x_2 + y_1 y_2) \phi_2 + \frac{2}{A} (x_1 x_3 + y_1 y_3) \phi_3] \\
&- \frac{k_o^2 \epsilon_r}{3} [A \phi_1 + \frac{A}{2} \phi_2 + \frac{A}{2} \phi_3] .
\end{aligned} \tag{2.27}$$

Define the vector location of node i , with coordinates (x_i, y_i) as

$$\bar{r}_i = x_i + jy_i$$

and the vector from node i to node j as

$$\bar{r}_{ij} = \bar{r}_j - \bar{r}_i .$$

Note that

$$A = \frac{1}{2} \hat{z} \cdot \bar{r}_{12} \times \bar{r}_{23} = \frac{1}{2} \hat{z} \cdot \bar{r}_{23} \times \bar{r}_{31} = \frac{1}{2} \hat{z} \cdot \bar{r}_{31} \times \bar{r}_{12} .$$

With the above convention, (2.27) reduces to

$$\frac{\partial I_{\Lambda_{123}}}{\partial \phi_1} = \frac{|\bar{r}_{23}|^2}{2A} \phi_1 + \frac{\bar{r}_{23} \cdot \bar{r}_{31}}{2A} \phi_2 + \frac{\bar{r}_{23} \cdot \bar{r}_{12}}{2A} \phi_3 - \frac{k_o^2 \epsilon_r}{3} [A\phi_1 + \frac{A}{2} \phi_2 + \frac{A}{2} \phi_3] , \quad (2.28)$$

wherein the various vectors are shown in Fig. 2.5 . We note here that the self-node contribution of the Laplacian term is proportional to the ratio of the square of the distance of the side opposite to a node to the area of the element, while the coefficients of the mutual terms in the Laplacian are proportional to the cotangent of the angle formed by the sides at the opposite non-self node

One can obtain the Laplacian term above in an alternative way. Expanding ϕ in area coordinates as in (2.18) and noting that $\nabla \phi$ is given by (2.24a), one can use $\nabla^2 \phi = \nabla \cdot \nabla \phi$ and approximate the divergence as

$$\nabla \cdot \bar{A} \approx \frac{1}{\text{Area}} \int_C \bar{A} \cdot \hat{n} \, dl, \quad (2.29)$$

where \hat{n} is the normal to the contour C (in the plane of C) enclosing the triangles. Using (2.24a) in (2.29), one obtains exactly the Laplacian term given in (2.27). Such an observation is very useful when dealing with surfaces

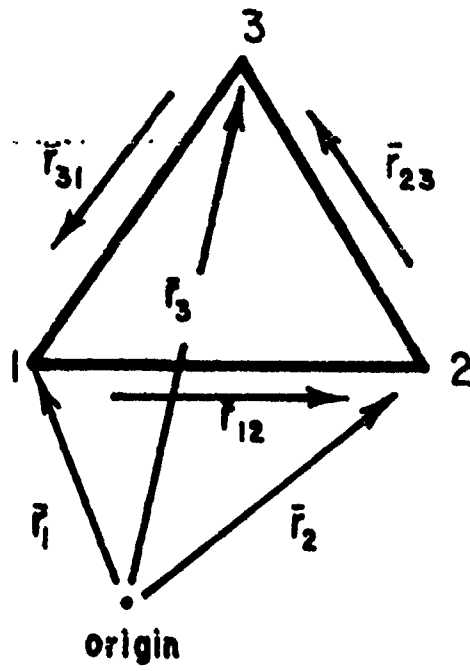


Figure 2.5. Vector definitions of nodes in an element.

that may be irregularly shaped or for problems wherein the functional I cannot be easily formulated.

In general, if there are N_i nodes around node i , as shown in Fig. 2.4, differentiating the variational form with respect to each of the nodal values ϕ_i , yields

$$\begin{aligned} \frac{\partial I}{\partial \phi_i} = & \phi_i \sum_{j=1}^{N_i} \left| \frac{\bar{r}_{j,j+1}^{-i}}{2\Lambda_j^i} \right|^2 \\ & + \sum_{j=1}^{N_i} \left[\frac{\bar{r}_{j,j-1}^{-i} \cdot \bar{r}_{j-1}^{-i}}{2\Lambda_{j-1}^i} + \frac{\bar{r}_{j+1,j}^{-i} \cdot \bar{r}_j^{-i}}{2\Lambda_j^i} \right] \phi_{n_{ij}} \\ & - \frac{k_o^2 \epsilon_r}{3} \left[\phi_i \sum_{j=1}^{N_i} \Lambda_j^i + \sum_{n=1}^{N_i} \frac{1}{2} (\Lambda_j^i + \Lambda_{j-1}^i) \phi_{n_{ij}} \right], \end{aligned}$$

$$i = 1, 2, \dots, K, \quad (2.30)$$

where

$$\begin{aligned} \bar{r}_j^{-i} &= \bar{r}_{n_{ij}} - \bar{r}_i \\ \bar{r}_{j+1,j}^{-i} &= \bar{r}_{n_{i,j+1}} - \bar{r}_{n_{ij}} \end{aligned}$$

$$A_j^i = \frac{1}{2} \epsilon \cdot (\bar{r}_{j+1}^i \times \bar{r}_j^i)$$

$$j \equiv 1 + (j - 1)_{\text{mod } N_1} .$$

Equating (2.30) to zero so as to satisfy the stationarity property, we obtain the elements q_{nm} and t_{nm} of the matrices Q and T of (2.15) as

$$q_{nn} = \sum_{j=1}^{N_n} \left| \frac{\bar{r}_{j,j+1}^n}{2A_j^n} \right|^2 - \frac{k_0^2 \epsilon_r}{3} \sum_{j=1}^{N_n} A_j^n , \quad (2.31)$$

$$\begin{aligned} \begin{pmatrix} q_{nm} \\ -t_{nm} \end{pmatrix} &= \frac{\bar{r}_{m,m-1}^n \cdot \bar{r}_{m-1}^n}{2A_{m-1}^n} + \frac{\bar{r}_{m+1,m}^n \cdot \bar{r}_m^n}{2A_m^n} \\ &- \frac{k_0^2 \epsilon_r}{3} \left[\frac{1}{2} (A_m^n + A_{m-1}^n) \right] , \quad \begin{cases} m < K \\ m > K \end{cases} . \end{aligned} \quad (2.32)$$

Using (2.31) and (2.32), we may calculate the interior fields from (2.15) for each mode specified on the artificial circle. Once the interior fields are known, a finite difference scheme yields $\frac{\partial \psi_n}{\partial r} \Big|_{r=a}$. With ψ_n and $\frac{\partial \psi_n}{\partial r} \Big|_{r=a}$ known, the scattered field coefficients A_n , B_n are determined from (2.13).

2.3 Numerical Results of Unimoment Method

A computer program was first written using the procedure in [7] which uses the global coordinate representation. Later, a separate program using the local coordinate representation discussed here was written. Accuracy of the programs was checked by comparing with the exact solutions for a dielectric circular cylinder. Figs. 2.6 and 2.7 show the scattered field patterns for a two-layered circular cylinder and a two-layered elliptical cylinder, respectively. The agreement between the exact solution in Fig. 2.6 and the moment method solution in Fig. 2.7 is quite good. The minor difference one notices in the backscatter direction is attributed primarily to inaccuracies introduced by equating the analytically exact normal derivative of the exterior field with the numerically derived value for the interior field which was computed by a backward difference at the boundary.

A few additional comments concerning the use of the local coordinate representation are in order. The use of the connection matrix simplifies inputting the data to a computer code as well as saves significantly the time spent in searching through a list of element numbers to determine the connecting nodes. This fact becomes more apparent if one realizes that the element numbers are superfluous as

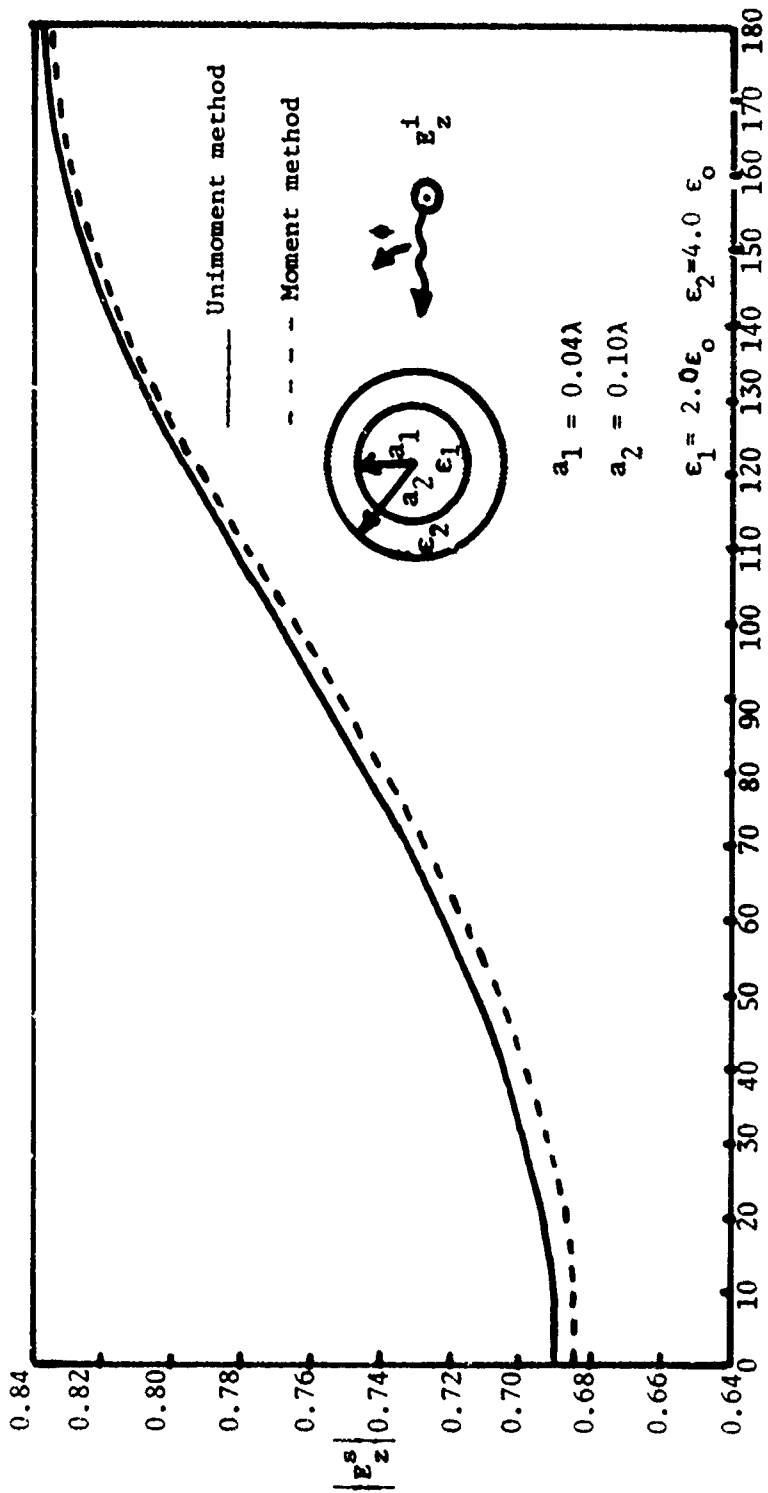


Figure 2.6. Scattering cross-section of a two-layered dielectric circular cylinder.

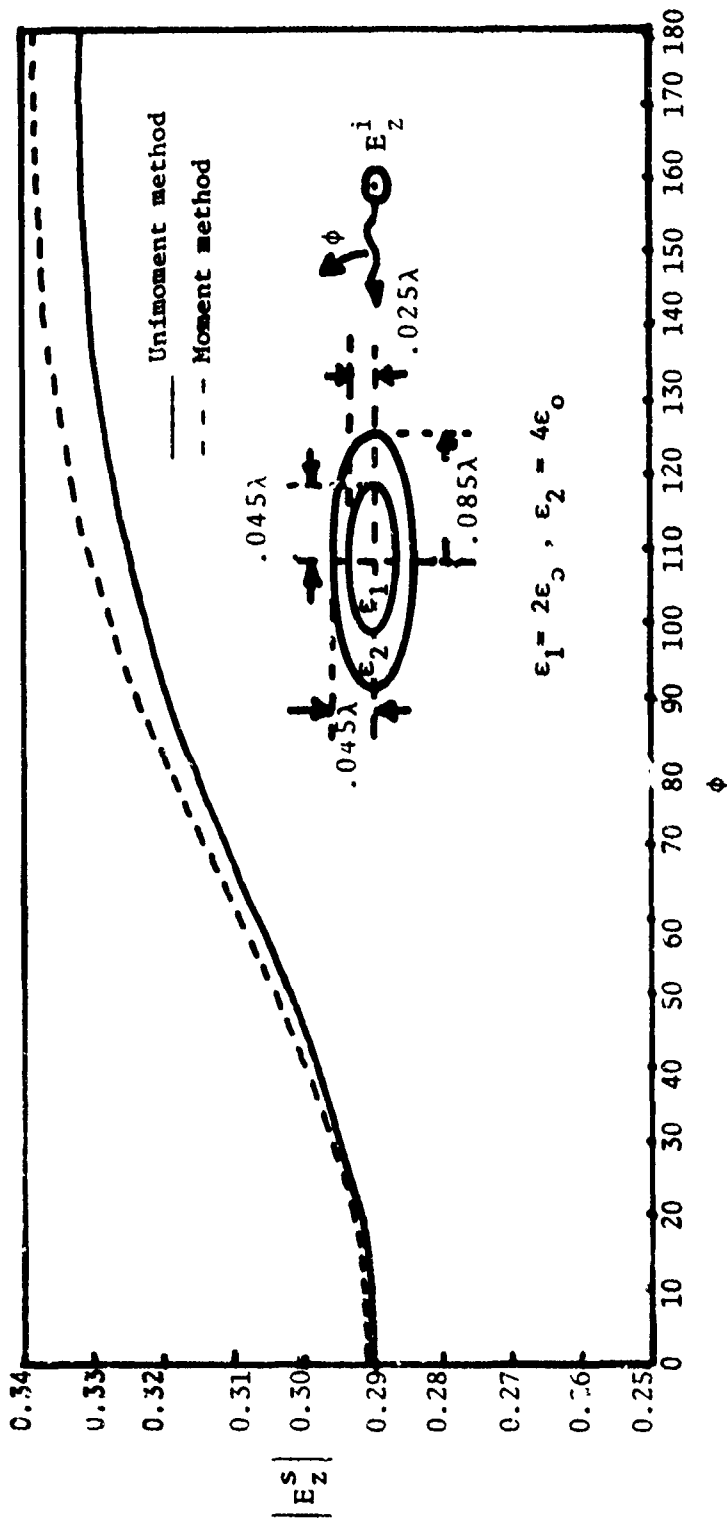


Figure 2.7. Scattering cross-section of a two-layered dielectric elliptic cylinder.

compared to the nodes that make up the elements. Further, the use of the area coordinate representation allows one to explicitly write the matrix elements in a simple form. These two aids to the organization of the finite element method have resulted in a saving by a factor as large as twenty in the computation time over that required by the method described in [7], even though the two approaches can be verified to be analytically and numerically identical.

2.4 A Comparison of Numerical Methods for Application to Missile Plume Problems

In this section we take a closer look at some of the features of the various methods indicated earlier, as they apply to the specific application we have in mind, namely, the calculation of the current induced on a missile with an attached electrically inhomogeneous exhaust plume.

We may immediately rule out the use of the extended boundary condition or T-matrix approach [2] for two reasons. First, the method is slowly convergent when the scatterer is not nearly spherical and hence is not suitable for application to the thin missile/plume configuration. Secondly, the entire domain basis representation of the fields (typically in terms of spherical harmonics) used in the method

is also numerically unstable whenever there are geometrical singularities such as would occur near the tip of the missile and at the missile-plume junction point near the rocket nozzle.

By contrast to the T-matrix approach, the volume polarization current approach [1] is a very numerically stable approach. However, it generally requires a large number of unknowns since the method requires one to solve for all three components of an effective polarization current. In the missile/plume problem, which can be treated as a body of revolution, if only the circumferentially uniform Fourier component of the missile current is desired, the number of vector components in the polarization current is reduced to two. Nevertheless, several other factors weigh heavily against this approach. The first is that the matrix that must be solved is full (i.e. not sparse). Not only does this fact mean that matrix fill time becomes expensive, but also because of the large storage requirement, out-of-core matrix solution techniques would be necessary. Secondly, the density of points at which the polarization current must be sampled is related to the local wavelength and skin depth in the medium and the rate at which the local medium parameters are changing. Thus the method is not suitable for layered inhomogeneous bodies or regions where the

parameters vary slow enough that layers can be used to approximate the scatterer.

This leaves for our consideration the unimoment method, discussed in detail in the previous section, and the surface integral equation formulation, both of which are numerically stable and result in banded matrices. Before comparing the methods, we consider the surface formulation in further detail. The approach for layered inhomogeneities is closely related to the surface field approach for homogeneous lossy dielectric scatterers. For homogeneous scatterers, the approach proceeds as follows. Referring to Fig. 2.8, one postulates surface currents \bar{J} and \bar{M} on the surface S . By relating the electric and magnetic fields to \bar{J} and \bar{M} and applying the boundary condition on S that the tangential fields have to be continuous across S , one obtains a pair of coupled integral equations in \bar{J} and \bar{M} . Using numerical methods, one may then solve the coupled integral equations for \bar{J} and \bar{M} . To extend the approach to layered inhomogeneous scatterers, such as the five-layer scatterer shown in Fig. 2.9, one may simultaneously solve for postulated surface currents on each of the surfaces, using the coupled integral equations derived by matching the fields at all the interfaces. The dimensions of the resultant matrix are such that a full matrix of those dimensions would quickly exceed the

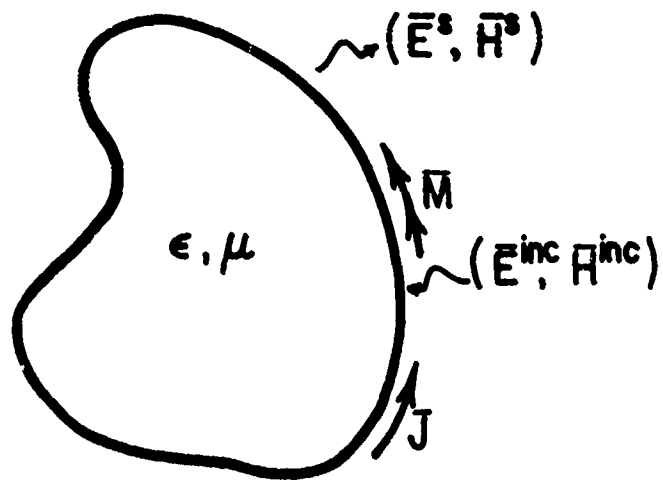


Figure 2.8. A homogeneous scatterer.

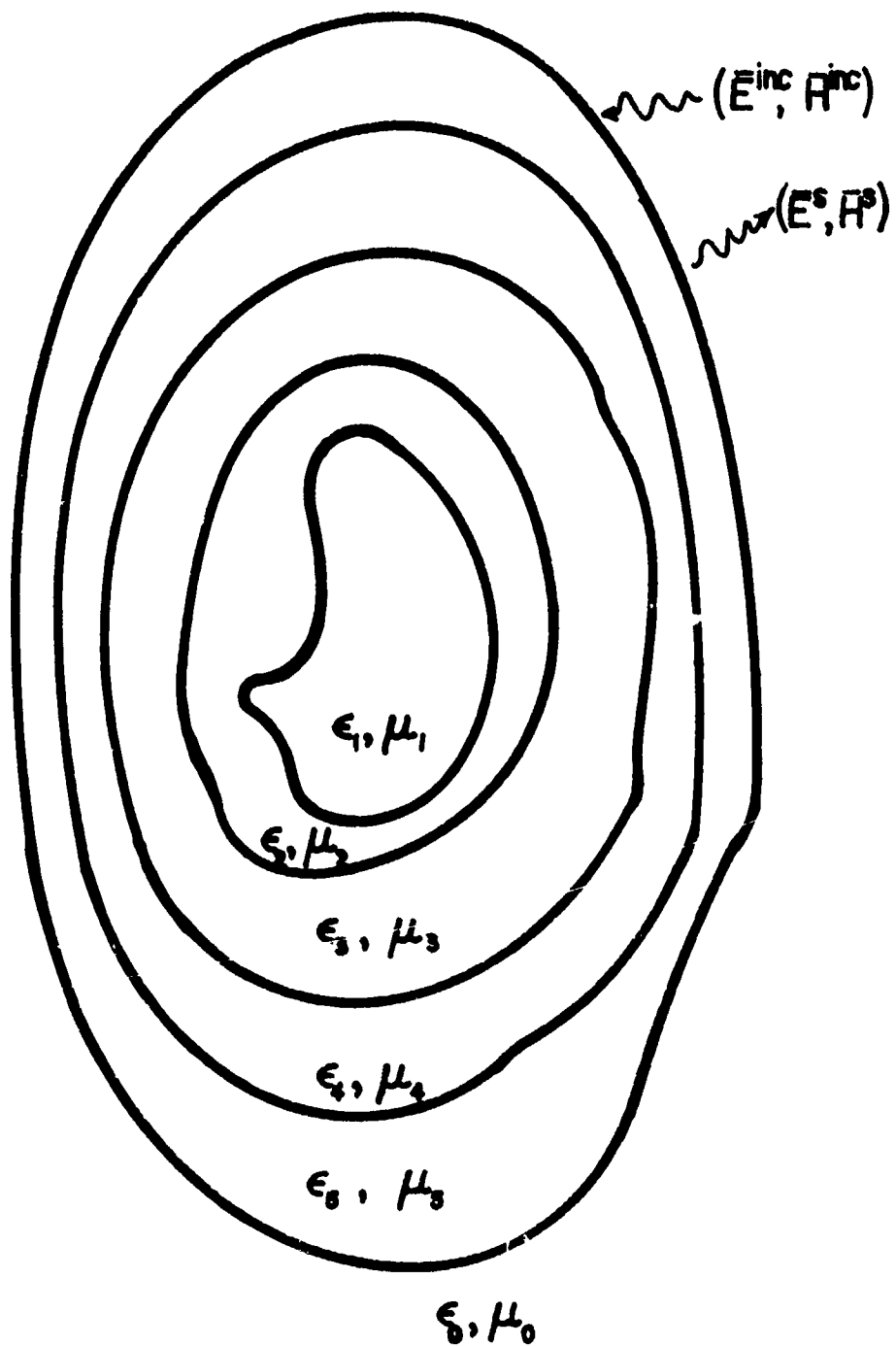


Figure 2.9. A five-layered dielectric scatterer.

storage available on most computers for most problems. However, if one recognizes the fact that a body with a layered inhomogeneity has a moment matrix which is block tridiagonal, one needs only to simultaneously store three of the much smaller blocks making up the matrix [4]. To illustrate this, we consider in some detail the example of the five-layered inhomogeneous scatterer shown in Fig. 2.9. If L_{ij} is the moment matrix for sources on layer j and field points on layer i , then the overall moment matrix equation is of the form

$$\begin{bmatrix} L_{11} & L_{12} & 0 & 0 & 0 \\ L_{21} & L_{22} & L_{23} & 0 & 0 \\ 0 & L_{32} & L_{33} & L_{34} & 0 \\ 0 & 0 & L_{43} & L_{44} & L_{45} \\ 0 & 0 & 0 & L_{54} & L_{55} \end{bmatrix} \begin{bmatrix} I_1 \\ I_2 \\ I_3 \\ I_4 \\ I_5 \end{bmatrix} = \begin{bmatrix} 0 \\ 0 \\ 0 \\ 0 \\ v^{inc} \end{bmatrix}, \quad (2.33)$$

where I_i is the column vector of unknown expansion coefficients of the postulated currents \bar{J}_i, \bar{M}_i on surface S_i and v^{inc} is related to the tangential incident field on the outermost layer. We note that the matrix is block tridiagonal in form. Beginning with the equation obtained from the first row of (2.33), repeated elimination results in

$$\begin{aligned}
 I_n &= -[L_{nn} - L_{n,n-1} M_{n-1} L_{n-1,n}]^{-1} L_{n,n+1} I_{n+1} \\
 &= M_n I_{n+1}, \quad n = 1, 2, 3, 4,
 \end{aligned} \tag{2.34}$$

with $M_0 = 0$, $L_{5,6} = I$, the identity matrix, and $I_{n+1} = -V^{inc}$ for $n=5$. We note immediately that the dimensions of the matrices which need to be in core at each stage of the iteration are much smaller than that of the overall matrix in (2.33). It should be further noted that the iterative approach in (2.34) uses only the non-zero sub-matrices in (2.33), thus avoiding storage of any of the zero sub-matrices in (2.33).

In order to compare the accuracy and efficiency of the surface current formulation approach with the unimoment method, a few test cases were tried. Figs. 2.6 and 2.7 show the scattered fields computed by the two methods for various two dimensional objects. Based on our experience of testing both approaches, we offer a list of observations presented in Table 2.1 as a guide to choosing between the two methods.

We note that a number of variations on the approaches considered here are possible and these can significantly affect our conclusions. For example, Morgan [8] uses a homogeneous core region in his unimoment method application and obtains a significant saving in the number of unknowns

required. Some of the features of the various methods discussed here can be combined. For example, one might use a finite element mesh, as in the unimoment method, to determine the fields interior to the inhomogeneous region and use a surface current formulation to simultaneously determine the fields at the boundary of the region and to enforce the radiation condition. Such an approach seems to combine many of the most desirable features of all the methods discussed here, but, unfortunately, has never been tested!

Of the two methods compared in Table 2.1, we choose to use the surface integral equation approach to treat the missile/plume problem. This choice is made because the missile/plume configuration is a thin structure and therefore not so suitable for the unimoment approach. Furthermore, we are primarily interested in surface currents and not with scattered fields. For these reasons, together with some of the complexities associated with extending the unimoment approach to bodies of revolution, we have chosen to employ the surface current formulation in the following chapters, which formulate the missile/plume problem.

Table 2.1

A Comparison of Features of Unimoment Method and Surface
Integral Equation Approach for Inhomogeneous Scatterers

Surface Integral Equation Approach	Unimoment Approach
1. Matrix elements are complex	1. The largest matrix, which must be inverted, is real if the medium is lossless.
2. The matrix is block-tridiagonal; matrices in each block are full.	2. Matrix is banded and sparse within a band. Nodes must be numbered in some optimal manner in order to achieve minimum bandwidth.
3. The $(m+1)$ -th surface must always enclose the m -th surface to retain the block-tridiagonal matrix feature.	3. The same finite element mesh can be used regardless of the nature of the inhomogeneity in the mesh region.
4. Method is very suitable for layered inhomogeneity or for regions which can be well modeled by layers.	4. Arbitrary inhomogeneous regions can be treated.
5. Method is equally well suited for thin or circular regions.	5. Method is more efficient and more accurate for nearly circular regions.

6. Method directly computes surface fields. Far fields must be computed by a separate integration.
6. Method directly computes scattered fields. Interior or surface fields must be computed as a separate step.
7. Generalization from two dimensional to three dimensional body of revolution is straightforward.
7. Generalization from two dimensions to body of revolution is non-trivial. A new set of potentials is necessary for a simplified implementation [8].

CHAPTER III
NUMERICAL SOLUTION PROCEDURE FOR SCATTERING
BY LAYERED DIELECTRIC BODY OF REVOLUTION

In this chapter, the integral equations are formulated for the surface currents induced by a plane wave incident on a dielectric layered body of revolution. The equivalence formulation results in interactions only between adjacent surfaces and hence we formulate the interactions for only two such surfaces, the p th and $(p-1)$ th. Many of the details of the numerical solution procedure essentially parallel those described in [11] and hence are not explained in detail. Numerical results for various configurations of layered bodies are obtained and compared with other results where available.

3.1 Formulation of the Integral Equations

Fig. 3.1 shows two layers of a N -layered dielectric body of revolution. These layers are formed by revolving the generator arcs ABC and PQR about the z -axis (assumed to be the axis of the body of revolution). The regions bounded by surfaces S_p and S_{p-1} are labelled as regions $p-1$, p , $p+1$ going from the inner to the outer layer. Note that there

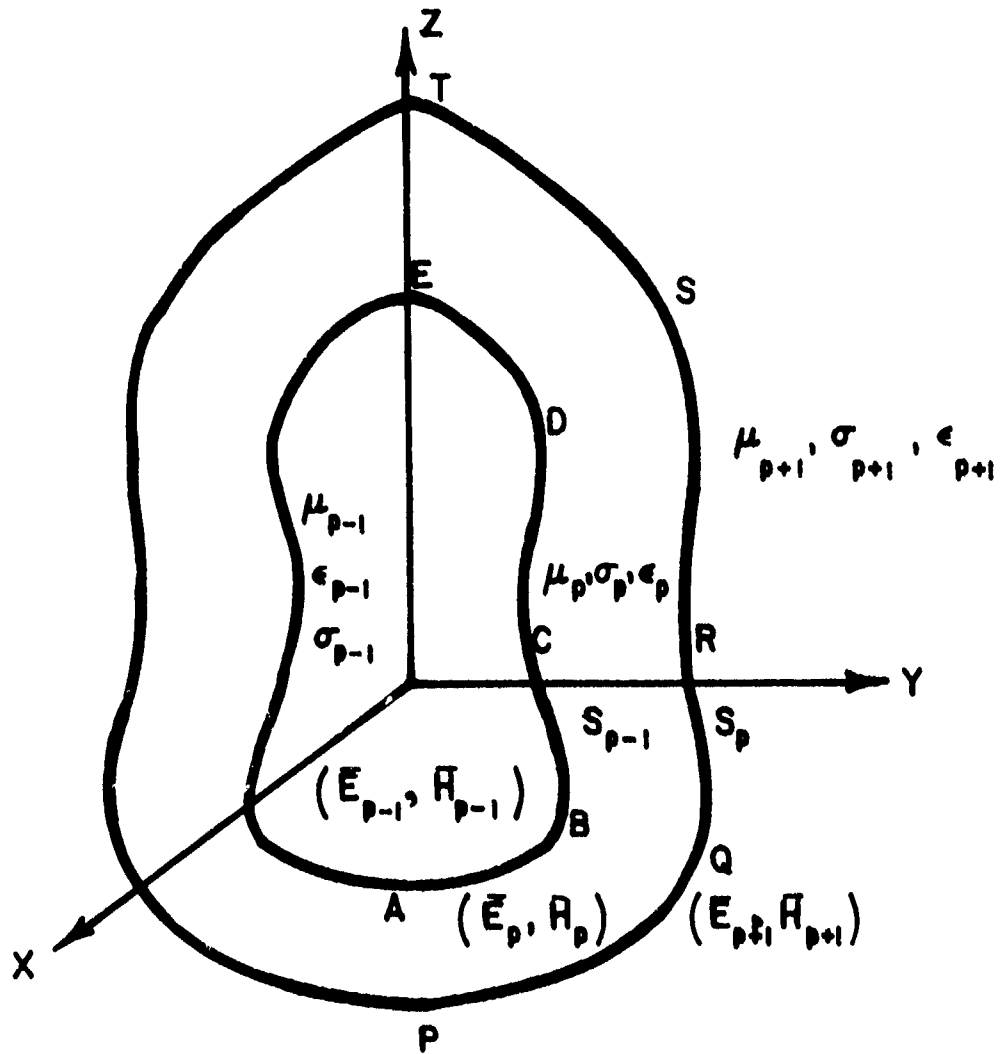


Figure 3.1. Two layers of a N - layered dielectric body of revolution.

may be other regions interior to $p-1$ and/or exterior to $p+1$. The physical parameters of the regions shown are $\mu_i, \epsilon_i, \sigma_i$, $i = p-1, p, p+1$.

Boundary conditions require that the total fields tangential to the two interface surfaces be continuous. This implies that

$$\left. \begin{aligned} \hat{n}_{p-1} \times \bar{E}_{p-1} &= \hat{n}_{p-1} \times \bar{E}_p \\ \hat{n}_{p-1} \times \bar{H}_{p-1} &= \hat{n}_{p-1} \times \bar{H}_p \end{aligned} \right\} \bar{r} \in S_{p-1} \quad \begin{array}{l} (3.1a) \\ (3.1b) \end{array}$$

$$\left. \begin{aligned} \hat{n}_p \times \bar{E}_p &= \hat{n}_p \times \bar{E}_{p+1} \\ \hat{n}_p \times \bar{H}_p &= \hat{n}_p \times \bar{H}_{p+1} \end{aligned} \right\} \bar{r} \in S_p \quad \begin{array}{l} (3.2a) \\ (3.2b) \end{array}$$

where (\bar{E}_i, \bar{H}_i) , $i = p-1, p, p+1$ are the total fields inside the respective regions, and $\hat{n}_i = \hat{\phi}_i \times \hat{t}_i$ is the outward unit vector normal to the i^{th} surface, with \hat{t}_i being the unit vector along the generator arc. On the N -th layer, we have similarly,

$$\hat{n}_N \times (\bar{E}_N - \bar{E}_{N+1}) = \hat{n}_N \times \bar{E}^{\text{inc}} \quad (3.3a)$$

$$\hat{n}_N \times (\bar{H}_N - \bar{H}_{N+1}) = \hat{n}_N \times \bar{H}^{\text{inc}} \quad (3.3b)$$

Using the equivalence principle, we divide the problem into three parts, one each for the evaluation of the fields in the three regions. Thus, if we assume equivalent electric and magnetic currents \bar{J}_i, \bar{M}_i , $i = p-1, p$, on the two surfaces, the three equivalences are obtained as shown in Fig. 3.2. Note that the currents all radiate in a homogeneous medium in each of the cases depicted in Fig. 3.2. The equivalent currents on the interior of a given surface are merely the negative of those on the exterior to the surface in view of the continuity of the tangential fields at the surfaces. The fields in (3.1) and (3.2) can thus be written as

$$\bar{E}_i(\bar{r}) = -j\omega\bar{A}_i(\bar{r}) - \nabla\phi_i^e(\bar{r}) - \frac{1}{\epsilon_i} \nabla\times\bar{F}_i(\bar{r}) \quad (3.4a)$$

$$\bar{H}_i(\bar{r}) = -j\omega\bar{F}_i(\bar{r}) - \nabla\phi_i^m(\bar{r}) + \frac{1}{\mu_i} \nabla\times\bar{A}_i(\bar{r}) \quad (3.4b)$$

$$i = p-1, p, p+1, \quad (3.4b)$$

where the potentials are defined as follows:

$$\bar{A}_{p-1}(\bar{r}) = -\frac{\mu_{p-1}}{4\pi} \iint_{S_{p-1}} \bar{J}_{p-1}(\bar{r}') G_{p-1}(\bar{r}, \bar{r}') ds' \quad (3.5a)$$

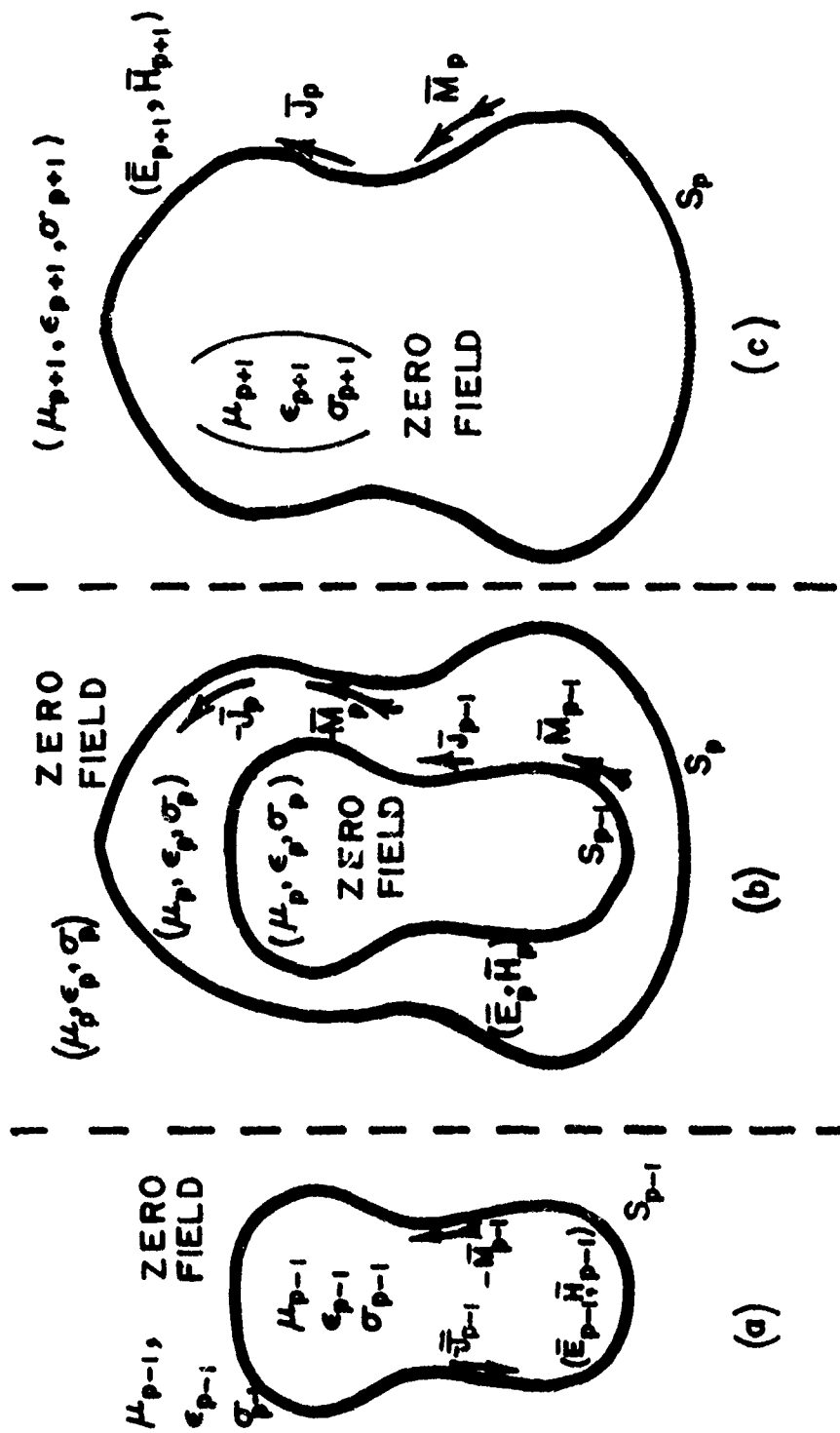


Figure 3.2. Equivalent problems in the various regions.

$$\bar{F}_{p-1}(\bar{r}) = -\frac{\epsilon_{p-1}}{4\pi} \iint_{S_{p-1}} \bar{M}_{p-1}(\bar{r}') G_{p-1}(\bar{r}, \bar{r}') ds' \quad (3.5b)$$

$$\phi_{p-1}^e(\bar{r}) = -\frac{1}{4\pi\epsilon_{p-1}} \iint_{S_{p-1}} \rho_{p-1}^e(\bar{r}') G_{p-1}(\bar{r}, \bar{r}') ds' \quad (3.5c)$$

$$\phi_{p-1}^m(\bar{r}) = -\frac{1}{4\pi\mu_{p-1}} \iint_{S_{p-1}} \rho_{p-1}^m(\bar{r}') G_{p-1}(\bar{r}, \bar{r}') ds' \quad (3.5d)$$

$$\begin{aligned} \bar{A}_p(\bar{r}) &= \frac{\mu_p}{4\pi} \iint_{S_{p-1}} \bar{J}_{p-1}(\bar{r}') G_p(\bar{r}, \bar{r}') ds' \\ &\quad - \frac{\mu_p}{4\pi} \iint_{S_p} \bar{J}_p(\bar{r}') G_p(\bar{r}, \bar{r}') ds' \end{aligned} \quad (3.6a)$$

$$\begin{aligned} \bar{F}_p(\bar{r}) &= \frac{\epsilon_p}{4\pi} \iint_{S_{p-1}} \bar{M}_{p-1}(\bar{r}') G_p(\bar{r}, \bar{r}') ds' \\ &\quad - \frac{\epsilon_p}{4\pi} \iint_{S_p} \bar{M}_p(\bar{r}') G_p(\bar{r}, \bar{r}') ds' \end{aligned} \quad (3.6b)$$

$$\begin{aligned}\phi_p^e(\bar{r}) &= \frac{1}{4\pi\epsilon_p} \iint_{S_{p-1}} \rho_{p-1}^e(\bar{r}') G_{p-1}(\bar{r}, \bar{r}') ds' \\ &- \frac{1}{4\pi\epsilon_p} \iint_{S_p} \rho_p^e(\bar{r}') G_p(\bar{r}, \bar{r}') ds'\end{aligned}\quad (3.6c)$$

$$\begin{aligned}\phi_p^m(\bar{r}) &= \frac{1}{4\pi\mu_p} \iint_{S_{p-1}} \rho_{p-1}^m(\bar{r}') G_p(\bar{r}, \bar{r}') ds' \\ &- \frac{1}{4\pi\mu_p} \iint_{S_p} \rho_p^m(\bar{r}') G_p(\bar{r}, \bar{r}') ds'\end{aligned}\quad (3.6d)$$

$$\bar{A}_{p+1}(\bar{r}) = \frac{\mu_{p+1}}{4\pi} \iint_{S_p} \bar{J}_p(\bar{r}') G_{p+1}(\bar{r}, \bar{r}') ds' \quad (3.7a)$$

$$\bar{F}_{p+1}(\bar{r}) = \frac{\epsilon_{p+1}}{4\pi} \iint_{S_p} \bar{M}_p(\bar{r}') G_{p+1}(\bar{r}, \bar{r}') ds' \quad (3.7b)$$

$$\phi_{p+1}^e(\bar{r}) = \frac{1}{4\pi\epsilon_{p+1}} \iint_{S_p} \rho_p^e(\bar{r}, \bar{r}') G_{p+1}(\bar{r}, \bar{r}') ds' \quad (3.7c)$$

$$\phi_{p+1}^m(\bar{r}) = \frac{1}{4\pi\mu_{p+1}} \iint_{S_p} \rho_p^m(\bar{r}, \bar{r}') G_{p+1}(\bar{r}, \bar{r}') ds' \quad (3.7d)$$

and where

$$G_i(\bar{r}, \bar{r}') = \frac{e^{-jk_i R}}{R} \quad (3.8)$$

$$i = p-1, p, p+1$$

$$R = |\bar{r} - \bar{r}'| = [\rho^2 + \rho'^2 - 2\rho\rho' \cos(\phi - \phi') + (z - z')^2]^{\frac{1}{2}}$$

Using the continuity equation, one can express the charge densities in terms of the current densities as

$$\rho_i^e = \frac{1}{\omega} [\nabla'_s \cdot \bar{J}_i(\bar{r}')] \quad (3.9a)$$

$$\rho_i^n = \frac{j}{\omega} [\nabla'_s \cdot \bar{M}_i(\bar{r}')] \quad (3.9b)$$

$$i = p-1, p.$$

Using (3.4) through (3.9) in (3.1) and (3.2), one obtains the integro-differential equations for the unknown electric and magnetic currents, shown on the following pages.

$$\begin{aligned}
\hat{n}_{p-1} \times & \left\{ \frac{j\omega}{4\pi} \iint_{S_{p-1}} \bar{J}_{p-1} (\mu_{p-1} G_{p-1} + \mu_p G_p) ds' \right. \\
& + \frac{j}{4\pi\omega} \nabla \iint_{S_{p-1}} (\nabla'_s \cdot \bar{J}_{p-1}) \left\{ \frac{G_{p-1}}{\epsilon_{p-1}} + \frac{G_p}{\epsilon_p} \right\} ds' \\
& + \frac{1}{4\pi} \nabla \times \iint_{S_{p-1}} \bar{M}_p (G_{p-1} + G_p) ds' - \frac{j\omega}{4\pi} \iint_{S_p} \bar{J}_p \mu_p G_p ds' \\
& \left. - \frac{1}{4\pi\omega} \nabla \iint_{S_p} (\nabla'_s \cdot \bar{J}_p) \frac{G_p}{\epsilon_p} ds' - \frac{1}{4\pi} \nabla \times \iint_{S_p} \bar{M}_p G_p ds' \right\} \\
& = 0, \quad \bar{r} \in S_{p-1} \qquad (3.10a)
\end{aligned}$$

$$\begin{aligned}
\hat{n}_{p-1} \times & \left\{ \frac{j\omega}{4\pi} \iint_{S_{p-1}} \bar{M}_{p-1} (\epsilon_{p-1} G_{p-1} + \epsilon_p G_p) ds' \right. \\
& + \frac{j}{4\pi\omega} \nabla \iint_{S_{p-1}} (\nabla'_s \cdot \bar{M}_{p-1}) \left\{ \frac{G_{p-1}}{\mu_{p-1}} + \frac{G_p}{\mu_p} \right\} ds' \\
& - \frac{1}{4\pi} \nabla \times \iint_{S_{p-1}} \bar{J}_{p-1} (G_{p-1} + G_p) ds' - \frac{j\omega}{4\pi} \iint_{S_p} \bar{M}_p \epsilon_p G_p ds' \\
& \left. - \frac{j}{4\pi\omega} \nabla \iint_{S_p} (\nabla'_s \cdot \bar{M}_p) \frac{G_p}{\mu_p} ds' + \frac{1}{4\pi} \nabla \times \iint_{S_p} \bar{J}_p G_p ds' \right\} = 0, \\
& \qquad \qquad \qquad \bar{r} \in S_{p-1} \qquad (3.10b)
\end{aligned}$$

$$\begin{aligned}
\hat{n}_p \times & \left\{ \frac{j\omega}{4\pi} \iint_{S_p} \bar{J}_p (\mu_p G_p + \mu_{p+1} G_{p+1}) ds' \right. \\
& + \frac{j}{4\pi\omega} \nabla \iint_{S_p} (\nabla'_s \cdot \bar{J}_p) \left(\frac{G_p}{\epsilon_p} + \frac{G_{p+1}}{\epsilon_{p+1}} \right) ds' \\
& + \frac{1}{4\pi} \nabla \times \iint_{S_p} \bar{M}_p (G_p + G_{p+1}) ds' - \frac{j\omega}{4\pi} \iint_{S_{p-1}} \bar{J}_{p-1} \mu_p G_p ds' \\
& \left. - \frac{j}{4\pi\omega} \iint_{S_{p-1}} (\nabla'_s \cdot \bar{J}_{p-1}) \frac{G_p}{\epsilon_p} ds' - \frac{1}{4\pi} \nabla \times \iint_{S_{p-1}} \bar{M}_{p-1} G_p ds' \right\} = 0, \\
& \bar{r} \in S_p \quad (3.11a)
\end{aligned}$$

$$\begin{aligned}
\hat{n}_p \times & \left\{ \frac{j\omega}{4\pi} \iint_{S_p} \bar{M}_p (\epsilon_p G_p + \epsilon_{p+1} G_{p+1}) ds' \right. \\
& + \frac{j}{4\pi\omega} \nabla \iint_{S_p} (\nabla'_s \cdot \bar{M}_p) \left(\frac{G_p}{\mu_p} + \frac{G_{p+1}}{\mu_{p+1}} \right) ds' \\
& - \frac{1}{4\pi} \nabla \times \iint_{S_p} \bar{J}_p (G_p + G_{p+1}) ds' - \frac{j\omega}{4\pi} \iint_{S_{p-1}} \bar{M}_{p-1} \epsilon_p G_p ds' \\
& \left. - \frac{j}{4\pi\omega} \iint_{S_{p-1}} (\nabla'_s \cdot \bar{M}_{p-1}) \frac{G_p}{\mu_p} ds' + \frac{1}{4\pi} \nabla \times \iint_{S_{p-1}} \bar{J}_{p-1} G_p ds' \right\} = 0, \\
& \bar{r} \in S_p, (3.11b)
\end{aligned}$$

In (3.10) and (3.11), the dependence of the various quantities on source and/or field coordinates is implicitly understood. We next note that, for $i \neq j$,

$$\nabla \times \iint_{S_j} \bar{u}_j G(\bar{r}_i, \bar{r}'_j) ds' = - \iint_{S_j} \bar{u}_j \times \nabla G(\bar{r}_i, \bar{r}'_j) ds' \quad (3.12a)$$

$$\bar{u}_j = \bar{J}_j \text{ or } \bar{M}_j,$$

wherein the curl has been taken inside the integral since the field point \bar{r}_i and source point \bar{r}'_j are on different surfaces and hence $G(\bar{r}_i, \bar{r}'_j)$ is non-singular, assuming that the layers do not touch one another. However when \bar{r} and \bar{r}' are on the same surface, then it can be shown [12] that on the surface S_i

$$\nabla \times \iint_{S_i} \bar{u}_i (G_i + G_{i+1}) ds' = - \iint_{S_i} \bar{u}_i \times \nabla (G_i + G_{i+1}) ds' \quad (3.12b)$$

where \iint indicates a deleted integral around \bar{r} . Equations (3.10) and (3.11) can be written in compact form as

$$S_{p-1,p-1}(\bar{J}_{p-1}, \bar{M}_{p-1}) + C_{p-1,p}(\bar{J}_p, \bar{M}_p) = 0 \quad (3.13a)$$

$$C_{p,p-1}(\bar{J}_{p-1}, \bar{M}_{p-1}) + S_{p,p}(\bar{J}_p, \bar{M}_p) = 0 \quad (3.13b)$$

where $S_{ii}(\bar{J}_i, \bar{M}_i)$ represents the contribution to both electric and magnetic fields on surface i from currents existing on surface i , while $C_{ij}(\bar{J}_j, \bar{M}_j)$ represents the electric and magnetic fields evaluated on surface i due to currents existing on surface j . Such a compact form is necessary in order to generalize the procedure to an arbitrary number of layers. We can write (3.10) and (3.11) in component operator form as follows:

$$S_{ii}(\bar{J}_i, \bar{M}_i) = \begin{bmatrix} s_{11}(J_{i_t}) & s_{12}(J_{i_\phi}) & s_{13}(M_{i_t}) & s_{14}(M_{i_\phi}) \\ s_{21}(J_{i_t}) & s_{22}(J_{i_\phi}) & s_{23}(M_{i_t}) & s_{24}(M_{i_\phi}) \\ s_{31}(J_{i_t}) & s_{32}(J_{i_\phi}) & s_{33}(M_{i_t}) & s_{34}(M_{i_\phi}) \\ s_{41}(J_{i_t}) & s_{42}(J_{i_\phi}) & s_{43}(M_{i_t}) & s_{44}(M_{i_\phi}) \end{bmatrix} \quad (3.14)$$

$$C_{ij}(\bar{J}_j, \bar{M}_j) = \begin{bmatrix} c_{11}(J_{j_t}) & c_{12}(J_{j_\phi}) & c_{13}(M_{j_t}) & c_{14}(M_{j_\phi}) \\ c_{21}(J_{j_t}) & c_{22}(J_{j_\phi}) & c_{23}(M_{j_t}) & c_{24}(M_{j_\phi}) \\ c_{31}(J_{j_t}) & c_{32}(J_{j_\phi}) & c_{33}(M_{j_t}) & c_{34}(M_{j_\phi}) \\ c_{41}(J_{j_t}) & c_{42}(J_{j_\phi}) & c_{43}(M_{j_t}) & c_{44}(M_{j_\phi}) \end{bmatrix} \quad (3.15)$$

with $i = j+1$ or $j-1$. Herein the first and third row of operators yield the t -directed component of the tangential electric and magnetic fields, respectively, while the second and fourth row of operators yield the ϕ -component of the tangential electric and magnetic fields. The dependence of the operators s_{ij} and c_{ij} on the various current components is clearly indicated. We next express all the operators in (3.14) and (3.15) in terms of the local coordinates (t, ϕ) on the surfaces. An orthogonal system of unit vectors $(\hat{n}_i, \hat{\phi}_i, \hat{t}_i)$, $i = p-1, p$, are associated with each point (t_i, ϕ_i) , $i = p-1, p$ on the surface S_i . These unit vectors are defined as follows:

$$\hat{n}_i = \cos \gamma_i \cos \phi_i \hat{x} + \cos \gamma_i \sin \phi_i \hat{y} - \sin \gamma_i \hat{z} \quad (3.16a)$$

$$\hat{\phi}_i = -\sin \phi_i \hat{x} + \cos \phi_i \hat{y} \quad (3.16b)$$

$$\hat{t}_i = \sin \gamma_i \cos \phi_i \hat{x} + \sin \gamma_i \sin \phi_i \hat{y} + \cos \gamma_i \hat{z} \quad (3.16c)$$

$i = p-1, p$, where γ_i is the angle between the tangent to the generating arc, \hat{t}_i , and the z -axis, defined to be positive if \hat{t}_i points away from the z -axis and negative if \hat{t}_i points toward the z -axis. The surface divergence can now be written as

$$\nabla'_{s_i} \cdot \bar{U}_i = \frac{1}{\rho'_i} \frac{\partial}{\partial t'_i} (\rho'_i U_{t'_i}) + \frac{1}{\rho'_i} \frac{\partial}{\partial \phi'_i} (U_{\phi'_i}), \quad (3.17)$$

$$\bar{U}_i = \bar{J}_i \text{ or } \bar{M}_i, \quad i = p-1, p.$$

Expanding (3.10) and (3.11) into component form and comparing with (3.14) and (3.15), one can easily obtain the expressions for s_{ij} and c_{ij} . For notational simplicity, we introduce the following operators:

$$\beta_{11}(U; \mu, \epsilon, t_i, t'_j, \phi_i, \phi'_j)$$

$$= \frac{j\omega}{4\pi} \iint_{S_j} U [\sin \gamma_i \sin \gamma'_j \cos(\phi'_j - \phi_i)$$

$$+ \cos \gamma_i \cos \gamma'_j] \mu G(t_i, t'_j) ds'$$

$$+ \frac{j}{4\pi\omega} \frac{\partial}{\partial t_i} \iint_{S_j} \frac{1}{\rho'_j} \frac{\partial}{\partial t'_j} (\rho'_j U) \frac{G(t_i, t'_j)}{\epsilon} ds' \quad (3.18a)$$

$$\begin{aligned}
& \beta_{12}(U; \mu, \epsilon, t_1, t'_j, \phi_1, \phi'_j) \\
&= -\frac{j\omega}{4\pi} \iint_{S_j} U \sin \gamma_1 \sin(\phi'_j - \phi_1) \mu G(t_1, t'_j) ds' \\
&+ \frac{j}{4\pi\omega} \frac{\partial}{\partial t_1} \iint_{S_j} \frac{1}{\rho'_j} \frac{\partial}{\partial \phi'_j} (U) \frac{G(t_1, t'_j)}{\epsilon} ds' \quad (3.18b)
\end{aligned}$$

$$\begin{aligned}
& \beta_{13}(U; \mu, \epsilon, t_1, t'_j, \phi_1, \phi'_j) \\
&= -\frac{1}{4\pi} \iint_{S_j} \frac{U}{R} [(\rho'_j \sin \gamma_1 \cos \gamma'_j - \rho_1 \cos \gamma_1 \sin \gamma'_j) \\
&\times \sin(\phi'_j - \phi_1) + (z_1 - z'_j) \sin \gamma_1 \sin \gamma'_j \sin(\phi'_j - \phi_1)] \\
&\cdot \frac{d}{dR} G(t_1, t'_j) ds' \quad (3.18c)
\end{aligned}$$

$$\begin{aligned}
& \beta_{14}(U; \mu, \epsilon, t_1, t'_j, \phi_1, \phi'_j) \\
&= -\frac{1}{4\pi} \iint_{S_j} \frac{U}{R} [\rho'_j \cos \gamma_1 - \rho_1 \cos \gamma_1 \cos(\phi'_j - \phi_1) \\
&+ (z_1 - z'_j) \sin \gamma_1 \cos(\phi'_j - \phi_1)] \frac{d}{dR} G(t_1, t'_j) ds' \quad (3.18d)
\end{aligned}$$

$$\begin{aligned}
& \beta_{21}(U; \mu, \epsilon, t_i, t'_j, \phi_i, \phi'_j) \\
&= \frac{j\omega}{4\pi} \iint_{S_j} U \sin \gamma'_j \sin(\phi'_j - \phi_i) \mu G(t_i, t'_j) ds' \\
&+ \frac{j}{4\pi\omega\rho_i} \frac{\partial}{\partial\phi_i} \iint_{S_j} \frac{1}{\rho'_j} \frac{\partial}{\partial t'_j} (\rho'_j U) \left(\frac{G(t_i, t'_j)}{\epsilon} \right) ds' \quad (3.18e)
\end{aligned}$$

$$\begin{aligned}
& \beta_{22}(U; \mu, \epsilon, t_i, t'_j, \phi_i, \phi'_j) \\
&= \frac{j\omega}{4\pi} \iint_{S_j} U \cos(\phi'_j - \phi_i) \mu G(t_i, t'_j) ds' \\
&+ \frac{j}{4\pi\omega\rho_i} \frac{\partial}{\partial\phi_j} \iint_{S_j} \frac{1}{\rho'_j} \frac{\partial}{\partial\phi'_j} (U) \left(\frac{G(t_i, t'_j)}{\epsilon} \right) ds' \quad (3.18f)
\end{aligned}$$

$$\begin{aligned}
& \beta_{23}(U; \mu, \epsilon, t_i, t'_j, \phi_i, \phi'_j) \\
&= - \frac{1}{4\pi} \iint_{S_j} \frac{U}{R} [\rho_i \cos \gamma'_j - \rho'_j \cos \gamma'_j \cos(\phi'_j - \phi_i) \\
&- (z_i - z'_j) \sin \gamma'_j \cos(\phi'_j - \phi_i)] \frac{d}{dR} G(t_i, t'_j) ds' \quad (3.18g)
\end{aligned}$$

$$\beta_{24}(U; \mu, \epsilon, t_i, t'_j, \phi_i, \phi'_j)$$

$$= -\frac{1}{4\pi} \iint_{S_j} \frac{U}{R} (z_i - z'_j) \sin(\phi'_j - \phi_i) \frac{d}{dR} G(t_i, t'_j) ds' \quad (3.18h)$$

where

$$G(t_i, t'_j) = \frac{e^{-jkR}}{R} \quad (3.19a)$$

$$R = |r_i - r'_j| = [\rho_i^2 + \rho_j'^2 - 2\rho_i \rho_j' \cos(\phi_i - \phi'_j) + (z_i - z'_j)^2]^{\frac{1}{2}}. \quad (3.19b)$$

With the above definitions we have the various s_{ij} and c_{ij} as:

$$s_{11}(J_{p-1}_t) = \beta_{11}(J_{p-1}_t; \mu_{p-1}, \epsilon_{p-1}, t_{p-1}, t'_{p-1}, \phi_{p-1}, \phi'_{p-1})$$

$$+ \beta_{11}(J_{p-1}_t; \mu_p, \epsilon_p, t_{p-1}, t'_{p-1}, \phi_{p-1}, \phi'_{p-1}) \quad (3.20a)$$

$$s_{12}(J_{p-1}_\phi) = \beta_{12}(J_{p-1}_\phi; \mu_{p-1}, \epsilon_{p-1}, t_{p-1}, t'_{p-1}, \phi_{p-1}, \phi'_{p-1})$$

$$+ \beta_{12}(J_{p-1}_\phi; \mu_p, \epsilon_p, t_{p-1}, t'_{p-1}, \phi_{p-1}, \phi'_{p-1}) \quad (3.20b)$$

$$\begin{aligned}
s_{13}(M_{p-1}_t) &= \beta_{13}(M_{p-1}_t; \mu_{p-1}, \varepsilon_{p-1}, t_{p-1}, t'_{p-1}, \phi_{p-1}, \phi'_{p-1}) \\
&+ \beta_{13}(M_{p-1}_t; \mu_p, \varepsilon_p, t_{p-1}, t'_{p-1}, \phi_{p-1}, \phi'_{p-1})
\end{aligned}
\tag{3.20c}$$

$$\begin{aligned}
s_{14}(M_{p-1}_\phi) &= \beta_{14}(M_{p-1}_\phi; \mu_{p-1}, \varepsilon_{p-1}, t_{p-1}, t'_{p-1}, \phi_{p-1}, \phi'_{p-1}) \\
&+ \beta_{14}(M_{p-1}_\phi; \mu_p, \varepsilon_p, t_{p-1}, t'_{p-1}, \phi_{p-1}, \phi'_{p-1})
\end{aligned}
\tag{3.20d}$$

$$\begin{aligned}
s_{21}(J_{p-1}_t) &= \beta_{21}(J_{p-1}_t; \mu_{p-1}, \varepsilon_{p-1}, t_{p-1}, t'_{p-1}, \phi_{p-1}, \phi'_{p-1}) \\
&+ \beta_{21}(J_{p-1}_t; \mu_p, \varepsilon_p, t_{p-1}, t'_{p-1}, \phi_{p-1}, \phi'_{p-1})
\end{aligned}
\tag{3.20e}$$

$$\begin{aligned}
s_{22}(J_{p-1}_\phi) &= \beta_{22}(J_{p-1}_\phi; \mu_{p-1}, \varepsilon_{p-1}, t_{p-1}, t'_{p-1}, \phi_{p-1}, \phi'_{p-1}) \\
&+ \beta_{22}(J_{p-1}_\phi; \mu_p, \varepsilon_p, t_{p-1}, t'_{p-1}, \phi_{p-1}, \phi'_{p-1})
\end{aligned}
\tag{3.20f}$$

$$\begin{aligned}
s_{23}(M_{p-1}_t) &= \beta_{23}(M_{p-1}_t; \mu_{p-1}, \varepsilon_{p-1}, t_{p-1}, t'_{p-1}, \phi_{p-1}, \phi'_{p-1}) \\
&+ \beta_{23}(M_{p-1}_t; \mu_p, \varepsilon_p, t_{p-1}, t'_{p-1}, \phi_{p-1}, \phi'_{p-1})
\end{aligned}
\tag{3.20g}$$

$$\begin{aligned}
s_{24}(M_{p-1}_\phi) &= \beta_{24}(M_{p-1}_\phi; \mu_{p-1}, \epsilon_{p-1}, t_{p-1}, t'_{p-1}, \phi_{p-1}, \phi'_{p-1}) \\
&+ \beta_{24}(M_{p-1}_\phi; \mu_p, \epsilon_p, t_{p-1}, t'_{p-1}, \phi_{p-1}, \phi'_{p-1})
\end{aligned}
\tag{3.20h}$$

$$s_{31}(J_{p-1}_t) = -s_{13}(J_{p-1}_t) \tag{3.20i}$$

$$s_{32}(J_{p-1}_\phi) = -s_{14}(J_{p-1}_\phi) \tag{3.20j}$$

$$\begin{aligned}
s_{33}(M_{p-1}_t) &= \beta_{11}(M_{p-1}_t; \epsilon_{p-1}, \mu_{p-1}, t_{p-1}, t'_{p-1}, \phi_{p-1}, \phi'_{p-1}) \\
&+ \beta_{11}(M_{p-1}_t; \epsilon_p, \mu_p, t_{p-1}, t'_{p-1}, \phi_{p-1}, \phi'_{p-1})
\end{aligned}
\tag{3.20k}$$

$$\begin{aligned}
s_{34}(M_{p-1}_\phi) &= \beta_{12}(M_{p-1}_\phi; \epsilon_{p-1}, \mu_{p-1}, t_{p-1}, t'_{p-1}, \phi_{p-1}, \phi'_{p-1}) \\
&+ \beta_{12}(M_{p-1}_\phi; \epsilon_p, \mu_p, t_{p-1}, t'_{p-1}, \phi_{p-1}, \phi'_{p-1})
\end{aligned}
\tag{3.20l}$$

$$s_{41}(J_{p-1}_t) = -s_{23}(J_{p-1}_t) \tag{3.20m}$$

$$s_{42}(J_{p-1}_\phi) = -s_{24}(J_{p-1}_\phi) \tag{3.20n}$$

$$\begin{aligned}
s_{43}(M_{p-1_t}) &= \beta_{21}(M_{p-1_t}; \epsilon_{p-1}, \mu_{p-1}, t_{p-1}, t'_{p-1}, \phi_{p-1}, \phi'_{p-1}) \\
&\quad + \beta_{21}(M_{p-1_t}; \epsilon_p, \mu_p, t_{p-1}, t'_{p-1}, \phi_{p-1}, \phi'_{p-1}) \\
&\hspace{15em} (3.20o)
\end{aligned}$$

$$\begin{aligned}
s_{44}(M_{p-1_\phi}) &= \beta_{22}(M_{p-1_\phi}; \epsilon_{p-1}, \mu_{p-1}, t_{p-1}, t'_{p-1}, \phi_{p-1}, \phi'_{p-1}) \\
&\quad + \beta_{22}(M_{p-1_\phi}; \epsilon_p, \mu_p, t_{p-1}, t'_{p-1}, \phi_{p-1}, \phi'_{p-1}) \\
&\hspace{15em} (3.20p)
\end{aligned}$$

$$c_{11}(J_{p_t}) = -\beta_{11}(J_{p_t}; \mu_p, \epsilon_p, t_{p-1}, t'_p, \phi_{p-1}, \phi'_p) \quad (3.21a)$$

$$c_{12}(J_{p_\phi}) = -\beta_{12}(J_{p_\phi}; \mu_p, \epsilon_p, t_{p-1}, t'_p, \phi_{p-1}, \phi'_p) \quad (3.21b)$$

$$c_{13}(M_{p_t}) = -\beta_{13}(M_{p_t}; \mu_p, \epsilon_p, t_{p-1}, t'_p, \phi_{p-1}, \phi'_p) \quad (3.21c)$$

$$c_{14}(M_{p_\phi}) = -\beta_{14}(M_{p_\phi}; \mu_p, \epsilon_p, t_{p-1}, t'_p, \phi_{p-1}, \phi'_p) \quad (3.21d)$$

$$c_{21}(J_{p_t}) = -\beta_{21}(J_{p_t}; \mu_p, \epsilon_p, t_{p-1}, t'_p, \phi_{p-1}, \phi'_p) \quad (3.21e)$$

$$c_{22}(J_{p_\phi}) = -\beta_{22}(J_{p_\phi}; \mu_p, \epsilon_p, t_{p-1}, t'_p, \phi_{p-1}, \phi'_p) \quad (3.21f)$$

$$c_{23}(M_{p_t}) = -\beta_{23}(M_{p_t}; \mu_p, \epsilon_p, t_{p-1}, t'_p, \phi_{p-1}, \phi'_p) \quad (3.21g)$$

$$c_{24}(M_{p\phi}) = -\beta_{24}(M_{p\phi}; \mu_p, \epsilon_p, t_{p-1}, t'_p, \phi_{p-1}, \phi'_p) \quad (3.21h)$$

$$c_{31}(J_{pt}) = -c_{13}(J_{pt}) \quad (3.21i)$$

$$c_{41}(J_{p\phi}) = -c_{14}(J_{p\phi}) \quad (3.21j)$$

$$c_{33}(M_{pt}) = -\beta_{11}(M_{pt}; \epsilon_p, \mu_p, t_{p-1}, t'_p, \phi_{p-1}, \phi'_p) \quad (3.21k)$$

$$c_{34}(M_{p\phi}) = -\beta_{12}(M_{p\phi}; \epsilon_p, \mu_p, t_{p-1}, t'_p, \phi_{p-1}, \phi'_p) \quad (3.21l)$$

$$c_{41}(J_{pt}) = -c_{23}(J_{pt}) \quad (3.21m)$$

$$c_{42}(J_{p\phi}) = -c_{24}(J_{p\phi}) \quad (3.21n)$$

$$c_{43}(M_{pt}) = -\beta_{21}(M_{pt}; \epsilon_p, \mu_p, t_{p-1}, t'_p, \phi_{p-1}, \phi'_p) \quad (3.21o)$$

$$c_{44}(M_{p\phi}) = -\beta_{22}(M_{p\phi}; \epsilon_p, \mu_p, t_{p-1}, t'_p, \phi_{p-1}, \phi'_p). \quad (3.21p)$$

We note (3.20) and (3.21) define $S_{p-1,p-1}(\bar{J}_{p-1}, \bar{M}_{p-1})$ and $C_{p-1,p}(\bar{J}_p, \bar{M}_p)$ in (3.13a). To find similar expressions for $S_{p,p}(\bar{J}_p, \bar{M}_p)$ in (3.13b), we replace $(p-1)$ by p and p by $(p+1)$ in (3.19). However, we replace $(p-1)$ by p and p by $(p-1)$ in (3.20) only for the field and source coordinate variables,

maintaining the medium parameters to be μ_p, ϵ_p , to obtain $C_{p,p-1}(\bar{J}_{p-1}, \bar{M}_{p-1})$ in (3.13b).

We next turn our attention to the numerical evaluation of the various quantities in (3.14) and (3.15). For this, we divide the generating arcs into a number of linear segments as shown in Fig. 3.3. The points $t_{i_0}, t_{i_1}, \dots, t_{i_n}, \dots, i = p-1, p$ specify the end points of the linear segments. The half-points, $t_{i_{1/2}}, t_{i_{1 1/2}}, \dots, t_{i_{n+1/2}}, \dots, i = p-1, p$, are defined by

$$t_{i_{n-1/2}} = \frac{(t_{i_n} + t_{i_{n-1}})}{2} \begin{cases} i = p-1, 1 \leq n \leq N_{p-1} + 1 \\ i = p, 1 \leq n \leq N_p + 1 \end{cases} \quad (3.22).$$

We next define expansion functions for the electric and magnetic currents. Since the scatterer is a body of revolution, we choose the ϕ -variation of the currents to be the Fourier modes in ϕ , while the t -variation is expanded in a pulse basis set. Thus we have

$$\begin{aligned} \bar{J}_i(t'_i, \phi'_i) &= \frac{\hat{t}_i}{2\pi\rho'_i} \sum_{m=-\infty}^{\infty} \sum_{n=1}^{N_i} I_{i_t}^{mn} P_1^n(t'_i) e^{jm\phi'_i} \\ &+ \hat{\phi}_i \sum_{m=-\infty}^{\infty} \sum_{n=1}^{N_i+1} J_{i_\phi}^{mn} P_2^n(t'_i) e^{jm\phi'_i} \end{aligned} \quad (3.23)$$

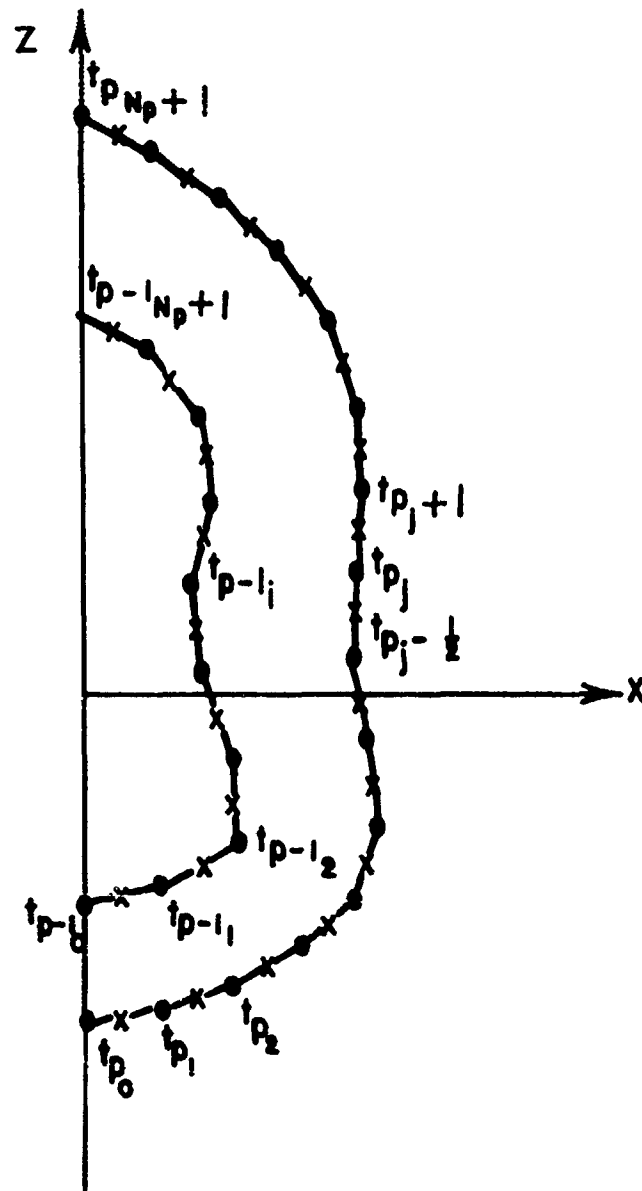


Figure 3.3. Linear segmentation of the generating arcs.

where $N_i = N_{p-1}$ or N_p for $i = p-1, p$. The derivative of J_{i_t} with respect to t_i is approximated as

$$\frac{\partial}{\partial t_i'} [\rho_i' J_{i_t}(t_i', \phi_i')] = \frac{1}{2\pi} \sum_{m=-\infty}^{\infty} \sum_{n=1}^{N_i+1} \left\{ \frac{I_{i_t}^{mn} - I_{i_t}^{m,n-1}}{\Delta t_{i_n}} \right\} \times P_2^n(t_i') e^{jm\phi_i'} \quad (3.24)$$

with $I_{i_t}^{m,0} = I_{i_t}^{m,N_i+1} = 0$. Herein $P_1^n(t_i')$ and $P_2^n(t_i')$ are defined as follows, for $i = p-1, p$:

$$P_1^n(t_i') = \begin{cases} 1, & t_{i_{n-\frac{1}{2}}} \leq t_i' \leq t_{i_{n+\frac{1}{2}}} \\ 0, & \text{otherwise} \end{cases} \quad (3.25a)$$

$$P_2^n(t_i') = \begin{cases} 1, & t_{i_{n-1}} \leq t_i' \leq t_n \\ 0, & \text{otherwise} \end{cases} \quad (3.25b)$$

$$\begin{aligned} \text{with } \Delta t_{i_n} &= |t_{i_n} - t_{i_{n-1}}| \\ &= [(\rho_{i_n} - \rho_{i_{n-1}})^2 + (z_{i_n} - z_{i_{n-1}})^2]^{\frac{1}{2}}. \end{aligned} \quad (3.26)$$

$I_{i_t}^{mn}$ and $J_{i_\phi}^{mn}$ are the unknown expansion coefficients of the "total modal current" ($2\pi \rho_{i_n} J_{i_t}^{mn}$) in the t -direction and

the actual modal current density in the ϕ -direction. The expansion of t - and ϕ -components in terms of the "total" current and current density, respectively, arises as a natural choice, particularly when one applies the surface divergence to the current representation. One observes further that $J_{i_t}(t'_i, \phi'_i)$, $i = \phi-1, p$, appears in all integrals with an associated factor ρ'_i , thus making it natural to consider the product $\rho'_i J_{i_t}(t'_i, \phi'_i)$ the unknown current. $J_{i_\phi}(t'_i, \phi'_i)$, on the other hand, does not appear this way and the artificial introduction of ρ'_i factor would introduce unwanted singularities in some of the integrals. Hence we expand J_{i_ϕ} alone. The magnetic currents $M_i(t'_i, \phi'_i)$ and their derivatives are expanded similarly with $K_{i_t}^{mn} = 2\pi\rho'_i M_{i_t}^{mn}$ and $M_{i_\phi}^{mn}$ replacing $I_{i_t}^{mn}$ and $J_{i_\phi}^{mn}$ respectively.

Features of the current expansion scheme in (3.23) and (3.24) are further discussed in [11]. The salient points are that since the Fourier modes are decoupled, one can solve for the Fourier components mode by mode. The staggered pulse basis set in the t -direction permits the modeling of open and closed (conducting) bodies and bodies with sharp edges without the placement of observation points for potential quantities at points wherein the corresponding sources (current or charge) may be singular.

We next define the testing functions

$$T_{j_1}^{pq} = P_1^q(t_j) e^{-jp\phi_j} \quad (3.27a)$$

$$T_{j_2}^{pq} = P_2^q(t_j) e^{-jp\phi_j} \quad (3.27b)$$

The t -component equations in (3.13a) and (3.13b) are tested with (3.27a) while the ϕ -component equations in (3.13a) and (3.13b) are tested with (3.27b). In order to perform the integrations analytically, we expand the Green's functions in Fourier series, as

$$\frac{e^{-jk_i R_o}}{R_o} = \frac{1}{2\pi} \sum_{m=-\infty}^{\infty} G_{i_m}(t_i, t'_j) e^{jm(\phi_i - \phi'_j)}$$

$$\frac{1}{R_o} \frac{d}{dR_o} \left(\frac{e^{-jk_i R_o}}{R_o} \right) = \frac{1}{2\pi} \sum_{m=-\infty}^{\infty} G'_{i_m}(t_i, t'_j) e^{jm(\phi_i - \phi'_j)}$$

where $i = p-1, p, p+1$ and

$$G_{i_m}(t_i, t'_j) = \int_{-\pi}^{\pi} \frac{e^{-jk_i R_o}}{R_o} \cos m\zeta \, d\zeta \quad (3.28a)$$

$$G'_{i_m}(t_i, t'_j) = \int_{-\pi}^{\pi} \frac{1}{R_o} \frac{d}{dR_o} \left\{ \frac{e^{-jk_i R_o}}{R_o} \right\} \cos m\xi \, d\xi \quad (3.28b)$$

$$R_o = [\rho_i^2 + \rho_j'^2 - 2\rho_i \rho_j' \cos \xi + (z_i - z_j')^2]^{\frac{1}{2}}. \quad (3.28c)$$

where $\xi = \phi_i - \phi_j'$. The form of the integrand in the above is obtained by noting that $\exp(-jk_i R_o)/R_o$ is even in ξ . With this, the surface integrals now reduce to a single integral over t . Following the procedures similar to those used for a homogeneous body of revolution [11], we can write the expressions for the elements $\beta_{ij_m}^{qn}$, where m refers to the m^{th} Fourier mode, while q and n refer to the field and source indices respectively. For notational simplicity, we define

$$\psi_i(t_{j_1}, t_{j_2}; t_{i_q}; m) = \int_{t_{j_1}}^{t_{j_2}} G_{i_m}(t_{i_q}, t'_j) dt'_j \quad (3.29a)$$

$$\psi_i^{\rho_j}(t_{j_1}, t_{j_2}; t_{i_q}; m) = \int_{t_{j_1}}^{t_{j_2}} G_{i_m}(t_{i_q}, t'_j) \rho_j' dt'_j \quad (3.29b)$$

where $G_{i_m}(t_i, t'_j)$ are defined in (3.28). We introduce next the weight functions arising due to the testing in the t -direction,

$$\chi_s(\Delta t_{i_q}, \gamma_{i_q}) = \frac{\Delta t_{i_{q+1}} \sin \gamma_{i_q} + \Delta t_{i_q} \sin \gamma_{i_q}}{2} \quad (3.30a)$$

$$\chi_c(\Delta t_{i_q}, \gamma_{i_q}) = \frac{\Delta t_{i_{q+1}} \cos \gamma_{i_q} + \Delta t_{i_q} \sin \gamma_{i_q}}{2} \quad (3.30b)$$

The various $\beta_{ij_m}^{qn}$ can now be written explicitly. One notes that the $\beta_{ij_m}^{qn}$ defined in the following pages are of the same form as the $\beta_{ij_m}^{qn}$ defined in (5.25) of [11], except that the elements there contain contributions from both sides of a surface and therefore involve two medium properties. The reason for defining the $\beta_{ij_m}^{qn}$ in terms of the parameters of a single medium is that s_{ij} involves the computation of β_{ij_m} for two media, while c_{ij} involves the computation of β_{ij} for only one medium. Thus the same computer subroutine for computing β_{ij} can be used either for the computation of s_{ij} or c_{ij} . Hence we finally write the $\beta_{ij_m}^{qn}$ as follows:

$$\begin{aligned}
\beta_{11}^{qn} = & \frac{j\omega}{8\pi} \sin \gamma_{j_n} \chi_s(\Delta t_{i_q}, \gamma_{i_q}) [\mu\psi_i(t_{j_{n-\frac{1}{2}}}, t_{j_n}; t_{i_q}; m+1) \\
& + \mu\psi_i(t_{j_{n-\frac{1}{2}}}, t_{j_n}, t_{i_q}; m-1)] \\
& + \frac{j\omega}{8\pi} \sin \gamma_{j_{n+1}} \chi_s(\Delta t_{i_q}, \gamma_{i_q}) [\mu\psi_i(t_{j_n}, t_{j_{n+\frac{1}{2}}}; t_{i_q}; m+1) \\
& + \mu\psi_i(t_{j_n}, t_{j_{n+\frac{1}{2}}}; t_{i_q}; m-1)] \\
& + \frac{j\omega}{4\pi} \cos \gamma_{j_n} \chi_c(\Delta t_{i_q}, \gamma_{i_q}) [\mu\psi_i(t_{j_{n-\frac{1}{2}}}, t_{j_n}; t_{i_q}; m)] \\
& + \frac{j\omega}{4\pi} \cos \gamma_{j_{n+1}} \chi_c(\Delta t_{i_q}, \gamma_{i_q}) [\mu\psi_i(t_{j_n}, t_{j_{n+\frac{1}{2}}}; t_{i_q}; m)] \\
& + \frac{j}{4\pi\omega\Delta t_{j_n}} \left[\frac{1}{\epsilon} \psi_i(t_{j_{n-1}}, t_{j_n}; t_{i_{q+\frac{1}{2}}}; m) \right. \\
& - \left. \frac{1}{\epsilon} \psi_i(t_{j_{n-1}}, t_{j_n}; t_{i_{q-\frac{1}{2}}}; m) \right] \\
& - \frac{j}{4\pi\omega\Delta t_{j_{n+1}}} \left[\frac{1}{\epsilon} \psi_i(t_{j_n}, t_{j_{n+1}}; t_{i_{q+\frac{1}{2}}}; m) \right. \\
& - \left. \frac{1}{\epsilon} \psi_i(t_{j_n}, t_{j_{n+1}}; t_{i_{q-\frac{1}{2}}}; m) \right], \tag{3.31a}
\end{aligned}$$

$$q = 1, 2, \dots, N_i$$

$$n = 1, 2, \dots, N_j$$

$$\begin{aligned}
\beta_{12m}^{qn} = & -\frac{1}{4}\omega \chi_s(\Delta t_{i_q}, \gamma_{i_q}) [\mu \psi_i^{\rho j}(t_{j_{n-1}}, t_{j_n}; t_{i_q}; m+1) \\
& - \mu \psi_i^{\rho j}(t_{j_{n-1}}, t_{j_n}; t_{i_q}; m-1)] \\
& - \frac{m}{2\omega} \left[\frac{1}{\epsilon} \psi_i(t_{j_{n-1}}, t_{j_n}; t_{i_{q+\frac{1}{2}}}; m) \right. \\
& \left. - \frac{1}{\epsilon} \psi_i(t_{j_{n-1}}, t_{j_n}; t_{i_{q-\frac{1}{2}}}; m) \right], \tag{3.31b}
\end{aligned}$$

$$q = 1, 2, \dots, N_i$$

$$n = 1, 2, \dots, N_j$$

$$\begin{aligned}
\beta_{21m}^{qn} = & \frac{\omega}{8\pi} \Delta t_{i_q} \sin \gamma_{j_n} [\mu \psi_i(t_{j_{n-\frac{1}{2}}}, t_{j_n}; t_{i_{q-\frac{1}{2}}}; m+1) \\
& - \mu \psi_i(t_{j_{n-\frac{1}{2}}}, t_{j_n}; t_{i_{q-\frac{1}{2}}}; m-1)] \\
& + \frac{\omega}{8\pi} \Delta t_{i_q} \sin \gamma_{j_{n+1}} [\mu \psi_i(t_{j_n}, t_{j_{n+\frac{1}{2}}}; t_{i_{q-\frac{1}{2}}}; m+1) \\
& - \mu \psi_i(t_{j_n}, t_{j_{n+\frac{1}{2}}}; t_{i_{q-\frac{1}{2}}}; m-1)] \\
& - \frac{m \Delta t_{i_q}}{4\pi\omega\rho_{i_{q-\frac{1}{2}}}} \left[\frac{1}{\epsilon} \psi_i(t_{j_{n-1}}, t_{j_n}; t_{i_{q-\frac{1}{2}}}; m) \right] \\
& + \frac{m \Delta t_{i_q}}{4\pi\omega\rho_{i_{q-\frac{1}{2}}}} \left[\frac{1}{\epsilon} \psi_i(t_{j_n}, t_{j_{n+1}}; t_{i_{q-\frac{1}{2}}}; m) \right], \tag{3.31c}
\end{aligned}$$

$$q = 1, 2, \dots, N_i$$

$$n = 1, 2, \dots, N_j$$

$$\begin{aligned}
\beta_{22}^{qn} = & \frac{1}{4} j\omega\Delta t_{i_q} [\mu\psi_i^{\rho_j}(t_{j_{n-1}}, t_{j_n}; t_{i_{q-\frac{1}{2}}}; m+1) \\
& + \mu\psi_i^{\rho_j}(t_{j_{n-1}}, t_{j_n}; t_{i_{q-\frac{1}{2}}}; m-1)] \\
& - \frac{j m^2 \Delta t_{i_q}}{2\omega\rho_{i_{q-\frac{1}{2}}}} \left[\frac{1}{\epsilon} \psi_i(t_{j_{n-1}}, t_{j_n}; t_{i_{q-\frac{1}{2}}}; m) \right], \quad (3.31d)
\end{aligned}$$

$$q = 1, 2, \dots, N_i + 1$$

$$n = 1, 2, \dots, N_j + 1$$

$$\begin{aligned}
\beta_{13}^{qn} = & -j \frac{\cos \gamma_{j_n}}{4\pi} \chi_s(\Delta t_{i_q}, \gamma_{i_q}) U_3^{\rho_j}(t_{j_{n-\frac{1}{2}}}, t_{j_n}; t_{i_q}; m) \\
& - j \frac{\cos \gamma_{j_{n+1}}}{4\pi} \chi_s(\Delta t_{i_q}, \gamma_{i_q}) U_3^{\rho_j}(t_{j_n}, t_{j_{n+\frac{1}{2}}}; t_{i_q}; m) \\
& + j\rho_{i_q} \frac{\sin \gamma_{j_n}}{4\pi} \chi_c(\Delta t_{i_q}, \gamma_{i_q}) U_0(t_{j_{n-\frac{1}{2}}}, t_{j_n}; t_{i_q}; m) \\
& + j\rho_{i_q} \frac{\sin \gamma_{j_{n+1}}}{4\pi} \chi_c(\Delta t_{i_q}, \gamma_{i_q}) U_0(t_{j_n}, t_{j_{n+\frac{1}{2}}}; t_{i_q}; m) \\
& - j \frac{\sin \gamma_{j_n}}{4\pi} \chi_s(\Delta t_{i_q}, \gamma_{i_q}) U_1(t_{j_{n-\frac{1}{2}}}, t_{j_n}; t_{i_q}; n) \\
& - j \frac{\sin \gamma_{j_{n+1}}}{4\pi} \chi_s(\Delta t_{i_q}, \gamma_{i_q}) U_1(t_{j_n}, t_{j_{n+\frac{1}{2}}}; t_{i_q}; m) \quad (3.31e)
\end{aligned}$$

$$q = 1, 2, \dots, N_i$$

$$n = 1, 2, \dots, N_j$$

$$\begin{aligned}
\beta_{14m}^{qn} &= \frac{1}{2} \chi_c(\Delta t_{i_q}, \gamma_{i_q}) U_4^{\rho_j}(t_{j_{n-1}}, t_{j_n}; t_{i_q}; m) \\
&- \rho_{i_q} \chi_c(\Delta t_{i_q}, \gamma_{i_q}) U_5^{\rho_j}(t_{j_{n-1}}, t_{j_n}; t_{i_q}; m) \\
&- \frac{1}{2} \chi_s(\Delta t_{i_q}, \gamma_{i_q}) U_2^{\rho_j}(t_{j_{n-1}}, t_{j_n}; t_{i_q}; m), \quad (3.31f)
\end{aligned}$$

$$q = 1, 2, \dots, N_i$$

$$n = 1, 2, \dots, N_j + 1$$

$$\begin{aligned}
\beta_{23m}^{qn} &= -\frac{\rho_{i_{q-\frac{1}{2}}}}{2\pi} \cos \gamma_{j_n} \Delta t_{i_q} U_5(t_{j_{n-\frac{1}{2}}}, t_{j_n}; t_{i_{q-\frac{1}{2}}}; m) \\
&- \frac{\rho_{i_{q-\frac{1}{2}}}}{2\pi} \cos \gamma_{j_{n+1}} \Delta t_{i_q} U_5(t_{j_n}, t_{j_{n+\frac{1}{2}}}; t_{i_{q-\frac{1}{2}}}; m) \\
&- \frac{1}{2\pi} \cos \gamma_{j_n} \Delta t_{i_q} U_6(t_{j_{n-\frac{1}{2}}}, t_{j_n}; t_{i_{q-\frac{1}{2}}}; m) \\
&- \frac{1}{2\pi} \cos \gamma_{j_{n+1}} \Delta t_{i_q} U_6(t_{j_n}, t_{j_{n+\frac{1}{2}}}; t_{i_{q-\frac{1}{2}}}; m) \\
&+ \frac{1}{2\pi} \sin \gamma_{j_n} \Delta t_{i_q} U_2(t_{j_{n-\frac{1}{2}}}, t_{j_n}; t_{i_{q-\frac{1}{2}}}; m) \\
&+ \frac{1}{2\pi} \sin \gamma_{j_{n+1}} \Delta t_{i_q} U_2(t_{j_n}, t_{j_{n+\frac{1}{2}}}; t_{i_{q-\frac{1}{2}}}; m), \quad (3.31g)
\end{aligned}$$

$$q = 1, 2, \dots, N_i + 1$$

$$n = 1, 2, \dots, N_j$$

$$\beta_{24_m}^{qn} = -\frac{1}{2} j \Delta t_{i_q} U_1^{oi}(t_{j_{n-1}}, t_{j_n}; t_{i_{q-\frac{1}{2}}}; m), \quad (3.31h)$$

$$q = 1, 2, \dots, N_i + 1$$

$$n = 1, 2, \dots, N_j + 1.$$

The U's in (3.31) are defined as in (5.26) of [11] with (t_1, t_2) replaced by (t_{j_1}, t_{j_2}) , t_q replaced by t_{i_q} , the field points (ρ, ϕ, z) replaced by (ρ_i, ϕ_i, z_i) , the source points (ρ', ϕ', z') replaced by (ρ'_j, ϕ'_j, z'_j) and (5.27) of [11] is replaced by

$$G = \frac{e^{-jkR_o}}{R_o} \quad (3.32)$$

where k corresponds to the medium $p-1$, p , or $p+1$, as the case may be. This completes the definition of the elements of the self-impedance and mutual impedance matrices.

The incident plane wave fields are incident on the N^{th} or the outermost interface. These can be expressed as,

$$\bar{E}^{\text{inc}} = (E_{\theta}^i \hat{\theta}^i + E_{\phi}^i \hat{\phi}^i) e^{-jk_{N+1} \hat{n} \cdot \bar{r}_N} \quad (3.33a)$$

$$\bar{H}^{\text{inc}} = \frac{1}{\bar{n}_{N+1}} (E_{\phi}^i \hat{\phi}^i - E_{\theta}^i \hat{\theta}^i) e^{-jk_{N+1} \hat{n} \cdot \bar{r}_N} \quad (3.33b)$$

where

$$\hat{e}^i = \cos \theta^i \cos \phi^i \hat{x} + \cos \theta^i \sin \phi^i \hat{y} - \sin \theta^i \hat{z} \quad (3.34a)$$

$$\hat{\phi}^i = -\sin \phi^i \hat{x} + \cos \phi^i \hat{y} \quad (3.34b)$$

$$\hat{n} = -\sin \theta^i \cos \phi^i \hat{x} - \sin \theta^i \sin \phi^i \hat{y} - \cos \theta^i \hat{z} \quad (3.34c)$$

$$\vec{r}_N = \rho_N \cos \phi_N \hat{x} + \rho_N \sin \phi_N \hat{y} + z_N \hat{z} \quad (3.34d)$$

and η_{N+1} is the characteristic wave impedance of the (N+1) or outermost region. The tangential components of (3.33) are the forcing functions of (3.3). The corresponding elements of the drive vector are given by (5.30) of [11], where the field coordinates refer to the N^{th} or outermost interface.

After computing the matrix elements, the iteration procedure given in (2.34) can now be used to solve for the currents on the N^{th} or outermost surface. If one requires the currents on all the layers, then one has to carry out a back substitution process beginning with the currents computed on the outermost layer. However, if one is interested only in the fields on the exterior of the scatterer, then the currents on the outermost layer are sufficient.

The above procedure must in principle be carried out for each of the modes m , $-\infty \leq m \leq \infty$. In practice, however, one achieves convergence with only a finite number of modes.

Further, as shown in [11], computation of only the positive modes is sufficient to obtain the total contribution from all modes, positive and negative. This is because of various symmetry relationships between the matrix elements and currents for the negative modes and those for positive modes.

3.2 Eigenfunction Solution for a Three-layered Dielectric Sphere

In this section, we obtain expressions for the induced currents on a three-layered dielectric sphere illuminated by a plane wave. This is done to obtain a check on the formulation and computer code for the layered body of revolution discussed in the previous section. The procedure is similar to that for the case of a homogeneous sphere [13] which results in the well-known Mie series solution.

Consider the inhomogeneous sphere shown in Fig. 3.4. The various media are characterized by parameters $(\mu_i, \epsilon_i, \sigma_i)$, $i = 1, 4$. An incident plane wave, assumed to be polarized in the x-direction and travelling in the positive z-direction, can be expressed as

$$E_x^i = E_o e^{-jk_4 z} = E_o e^{-jk_4 r \cos \theta} \quad (3.35a)$$

$$H_y^i = \frac{E_o}{\eta_4} e^{-jk_4 z} = \frac{E_o}{\eta_4} e^{-jk_4 r \cos \theta} \quad (3.35b)$$

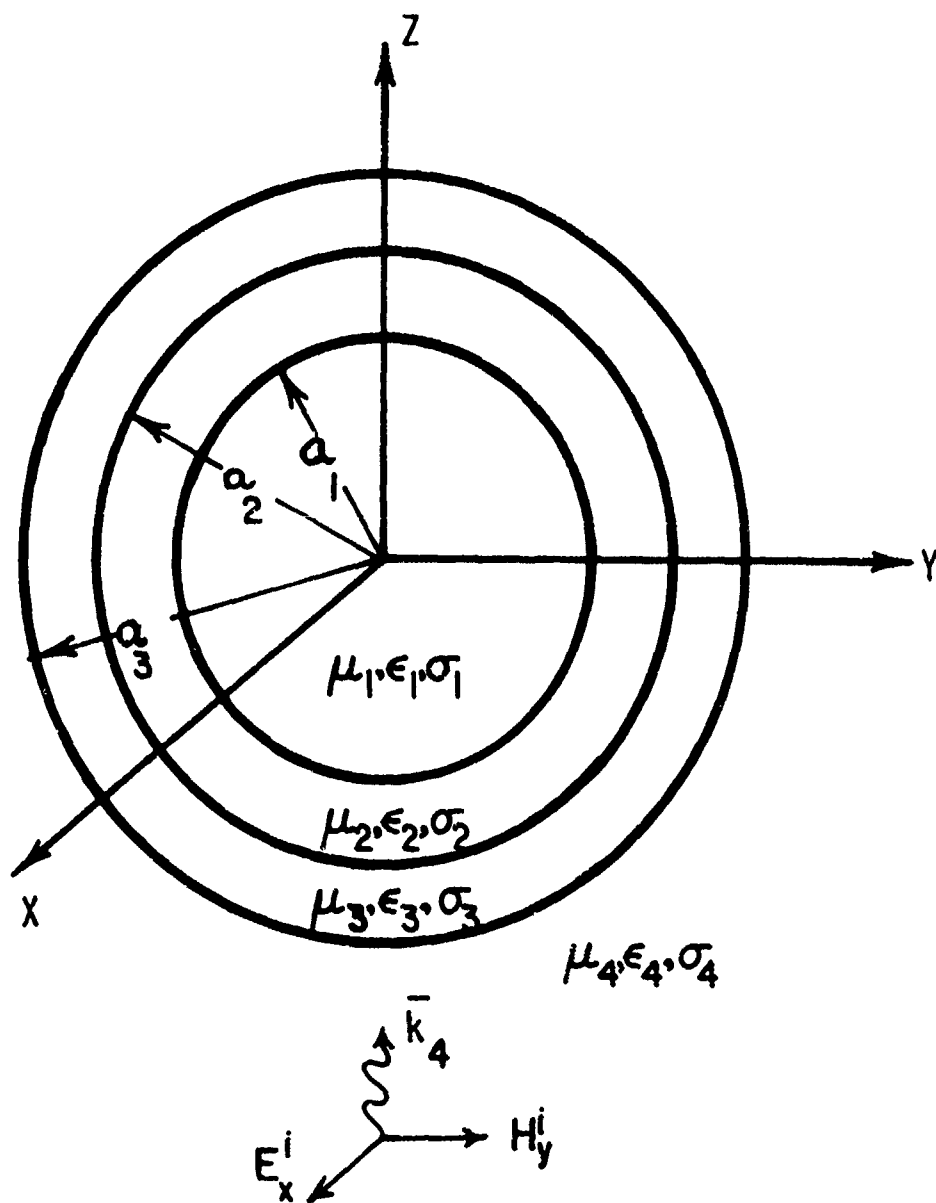


Figure 3.4. A three layered dielectric sphere.

where η_4 is the characteristic wave impedance of medium 4. For convenience in applying boundary conditions, we express the fields in terms of TM to r and TE to r problems. Thus we have associated incident electric and magnetic vector potentials, F_r^i , A_r^i , respectively, associated with the incident fields in (3.35) as [13],

$$A_r^i = \frac{E_0 \cos \phi}{\omega \mu_4} \sum_{n=1}^{\infty} a_n \hat{J}_n(k_4 r) P_n^1(\cos \theta) \quad (3.36a)$$

$$F_r^i = \frac{E_0 \sin \phi}{k_4} \sum_{n=1}^{\infty} a_n \hat{J}_n(k_4 r) P_n^1(\cos \theta) \quad (3.36b)$$

where

$$a_n = \frac{j^{-n}(2n+1)}{n(n+1)} \quad (3.36c)$$

Here

$$\hat{J}_n(kr) = kr j_n(kr) = \sqrt{\frac{kr}{2}} J_{n+\frac{1}{2}}(kr) \quad (3.37)$$

where $j_n(x)$ is the spherical Bessel function of order n , $J_n(x)$ is the ordinary cylindrical Bessel function, $P_n^1(\cos \theta)$

is the associated Legendre polynomial of degree n , order one. We next expand the fields in the various regions in terms of potentials of the same form as those expressing the incident field. Thus the fields in the various regions are expressed in terms of the following potentials:

$$A_{r_1} = \frac{E_o \cos \phi}{\omega \mu_4} \sum_{n=1}^{\infty} b_n \hat{J}_n(k_1 r) P_n^1(\cos \theta), \quad r < a_1 \quad (3.38a)$$

$$F_{r_1} = \frac{E_o \sin \phi}{k_4} \sum_{n=1}^{\infty} c_n \hat{J}_n(k_1 r) P_n^1(\cos \theta), \quad r < a_1 \quad (3.38b)$$

$$A_{r_2} = \frac{E_o \cos \phi}{\omega \mu_4} \sum_{n=1}^{\infty} \left\{ d_n \hat{J}_n(k_2 r) + e_n \hat{N}_n(k_2 r) \right\} P_n^1(\cos \theta),$$

$$a_1 < r < a_2 \quad (3.38c)$$

$$F_{r_2} = \frac{E_o \sin \phi}{k_4} \sum_{n=1}^{\infty} \left\{ f_n \hat{J}_n(k_2 r) + g_n \hat{N}_n(k_2 r) \right\} P_n^1(\cos \theta),$$

$$a_1 < r < a_2 \quad (3.38d)$$

$$A_{r_3} = \frac{E_o \cos \phi}{\omega \mu_4} \sum_{n=1}^{\infty} \left\{ t_n \hat{J}_n(k_3 r) + u_n \hat{N}_n(k_3 r) \right\} P_n^1(\cos \theta),$$

$$a_2 < r < a_3 \quad (3.38e)$$

$$F_{r_3} = \frac{E_o \sin \phi}{k_4} \sum_{n=1}^{\infty} \left\{ v_n \hat{J}_n(k_3 r) + w_n \hat{N}_n(k_3 r) \right\} P_n^1(\cos \theta),$$

$$a_2 < r < a_3 \quad (3.38f)$$

$$A_r^S = \frac{E_o \cos \phi}{\omega \mu_4} \sum_{n=1}^{\infty} r_n \hat{H}_n^{(2)}(k_4 r) P_n^1(\cos \theta), \quad r > a_3 \quad (3.38g)$$

$$F_r^S = \frac{E_o \sin \phi}{k_4} \sum_{n=1}^{\infty} s_n \hat{H}_n^{(2)}(k_4 r) P_n^1(\cos \theta), \quad r > a_3. \quad (3.38h)$$

Herein, $\hat{N}_n(kr)$ and $\hat{H}_n^{(2)}(kr)$ denote kr times the ordinary spherical Neumann and spherical Hankel function of the second kind, respectively. Note that the fields in region 1 are finite while the scattered fields are represented in terms of outgoing waves. The electric and magnetic fields can be determined from the potentials as follows [13]:

$$E_{\theta_i} = -\frac{1}{r} \frac{\partial F_{r_i}}{\partial \phi} + \frac{1}{j\omega \epsilon_i r} \frac{\partial^2 A_{r_i}}{\partial r \partial \theta} \quad (3.39a)$$

$$E_{\phi_i} = \frac{1}{r} \frac{\partial F_{r_i}}{\partial \theta} + \frac{1}{j\omega\epsilon_i r \sin \theta} \frac{\partial^2 A_{r_i}}{\partial r \partial \phi} \quad (3.39b)$$

$$H_{\theta_i} = \frac{1}{r \sin \theta} \frac{\partial A_{r_i}}{\partial \phi} + \frac{1}{j\omega\mu_i r} \frac{\partial^2 F_{r_i}}{\partial r \partial \theta} \quad (3.39c)$$

$$H_{\phi_i} = -\frac{1}{r} \frac{\partial A_{r_i}}{\partial \theta} + \frac{1}{j\omega\mu_i r \sin \theta} \frac{\partial^2 F_{r_i}}{\partial r \partial \phi} \quad (3.39d)$$

$$i = 1, 4.$$

The boundary conditions to be met are

$$E_{\theta_i}(r, \theta, \phi) = E_{\theta_{i+1}}(r, \theta, \phi), \text{ at } r = a_i \quad (3.40a)$$

$$H_{\theta_i}(r, \theta, \phi) = H_{\theta_{i+1}}(r, \theta, \phi), \text{ at } r = a_i \quad (3.40b)$$

$$E_{\phi_i}(r, \theta, \phi) = E_{\phi_{i+1}}(r, \theta, \phi), \text{ at } r = a_i \quad (3.40c)$$

$$H_{\phi_i}(r, \theta, \phi) = H_{\phi_{i+1}}(r, \theta, \phi), \text{ at } r = a_i \quad (3.40d)$$

$$0 \leq \theta \leq \pi, \quad -\pi \leq \phi \leq \pi, \quad i = 1, 2, 3.$$

In view of the independence of the TE_r and TM_r modes, we simply require

$$E_{\theta_i} \Big|_{TE_r} = E_{\theta_{i+1}} \Big|_{TE_r} \quad \text{at } r = a_i \quad (3.41a)$$

$$E_{\theta_i} \Big|_{TM_r} = E_{\theta_{i+1}} \Big|_{TM_r} \quad \text{at } r = a_i \quad (3.41b)$$

$$H_{\theta_i} \Big|_{TE_r} = H_{\theta_{i+1}} \Big|_{TE_r} \quad \text{at } r = a_i \quad (3.41c)$$

$$H_{\theta_i} \Big|_{TM_r} = H_{\theta_{i+1}} \Big|_{TM_r} \quad \text{at } r = a_i \quad (3.41d)$$

$$i = 1, 2, 3 .$$

Application of (3.41) automatically ensures the continuity of the ϕ -components of the fields as well. Use of (3.38) and (3.39) in (3.41) thus yields

$$c_n \hat{J}_n(k_1 a_1) = f_n \hat{J}_n(k_2 a_1) + g_n \hat{N}_n(k_2 a_1) \quad (3.42a)$$

$$b_n k_2 \mu_1 \hat{J}'_n(k_1 a_1) = \mu_2 k_1 \left\{ d_n \hat{J}'_n(k_2 a_1) + e_n \hat{N}'_n(k_2 a_1) \right\} \quad (3.42b)$$

$$k_2 \omega \epsilon_1 c_n \hat{J}'_n(k_1 a_1) = k_1 \omega \epsilon_2 \left\{ f_n \hat{J}'_n(k_2 a_1) + g_n \hat{N}'_n(k_2 a_1) \right\} \quad (3.42c)$$

$$b_n \hat{J}_n(k_1 a_1) = d_n \hat{J}_n(k_2 a_1) + e_n \hat{N}_n(k_2 a_1) \quad (3.42d)$$

$$f_n \hat{J}_n(k_2 a_2) + g_n \hat{N}_n(k_2 a_2) = v_n \hat{J}_n(k_3 a_2) + w_n \hat{N}_n(k_3 a_2) \quad (3.42e)$$

$$k_3 \mu_2 \left\{ d_n \hat{J}'_n(k_2 a_2) + e_n \hat{N}'_n(k_2 a_2) \right\} = k_2 \mu_3 \left\{ t_n \hat{J}'_n(k_3 a_2) + u_n \hat{N}'_n(k_3 a_2) \right\} \quad (3.42f)$$

$$k_3 \omega \epsilon_2 \left\{ f_n \hat{J}'_n(k_2 a_2) + g_n \hat{N}'_n(k_2 a_2) \right\} = k_2 \omega \epsilon_3 \left\{ v_n \hat{J}'_n(k_3 a_2) + w_n \hat{N}'_n(k_3 a_2) \right\} \quad (3.42g)$$

$$d_n \hat{J}_n(k_2 a_2) + e_n \hat{N}_n(k_2 a_2) = t_n \hat{J}_n(k_3 a_2) + u_n \hat{N}_n(k_3 a_2) \quad (3.42h)$$

$$v_n \hat{J}_n(k_3 a_3) + w_n \hat{N}_n(k_3 a_3) = a_n \hat{J}_n(k_4 a_3) + s_n \hat{H}_n^{(2)}(k_4 a_3) \quad (3.42i)$$

$$k_4 \mu_3 \left\{ t_n \hat{J}'_n(k_3 a_3) + u_n \hat{N}'_n(k_3 a_3) \right\} = k_3 \mu_4 \left\{ a_n \hat{J}'_n(k_4 a_3) \right. \\ \left. + r_n \hat{H}_n^{(2)'}(k_4 a_3) \right\} \quad (3.42j)$$

$$k_4 \omega \epsilon_3 \left\{ v_n \hat{J}'_n(k_3 a_3) + w_n \hat{N}'_n(k_3 a_3) \right\} = k_3 \omega \epsilon_4 \left\{ a_n J'_n(k_4 a_3) \right. \\ \left. + s_n \hat{H}_n^{(2)'}(k_4 a_3) \right\} \quad (3.42k)$$

$$t_n \hat{J}'_n(k_3 a_3) + u_n \hat{N}'_n(k_3 a_3) = a_n \hat{J}'_n(k_4 a_3) + r_n \hat{H}_n^{(2)'}(k_4 a_3) \quad (3.42l)$$

wherein the orthogonality amongst the modes has been utilized. Equations (3.42) are 12 equations in the 12 unknown coefficients. The coefficients were numerically determined by solving the system of linear equations (3.42). One notes that if (3.42) is written in matrix form, the matrix can be partitioned into two independent matrices (involving TE_r and TM_r coefficients) which are individually block tridiagonal. Hence an iteration scheme, similar to the one used for the layered body of revolution, can be developed. Equation (3.42) is to be solved for each of the modes n . (Note that only the θ -dependence of the fields varies from mode to mode, whereas the ϕ -dependence of the fields is fixed. Because we have considered axial incidence, only the

$e^{j\phi}$ Fourier mode in ϕ exists as indicated in (3.38)).

The number of modes is truncated at a finite number after convergence has been achieved.

Having determined the coefficients, we can compute the surface current on the outermost layer. We have

$$\bar{M}_3 = -\hat{r} \times \bar{E}_4 = -\bar{E}_{\theta 4} \hat{\phi} + \bar{E}_{\phi 4} \hat{\theta} \quad \text{at } r = a_3 \quad (3.43a)$$

$$\bar{J}_3 = \hat{r} \times \bar{H}_4 = H_{\theta 4} \hat{\phi} - H_{\phi 4} \hat{\theta} \quad \text{at } r = a_3. \quad (3.43b)$$

Using (3.38) and (3.39) in (3.43), we get the various components of the currents:

$$\begin{aligned} J_{\theta 3} = -H_{\phi 4} \Big|_{r=a_3} = & \frac{E_0 \cos \phi}{\omega \mu_4 a_3} \sum_{n=1}^{\infty} \left\{ a_n \hat{J}_n(k_4 a_3) \right. \\ & \left. + r_n \hat{H}_n^{(2)}(k_4 a_3) \right\} \frac{d}{d\theta} P_n^1(\cos \theta) \\ & - \frac{E_0 \cos \phi}{j \omega \mu_4 a_3 \sin \theta} \sum_{n=1}^{\infty} a_n J_n'(k_4 a_3) \\ & \left. + s_n \hat{H}_n^{(2)'}(k_4 a_3) \right\} P_n^1(\cos \theta) \end{aligned} \quad (3.44a)$$

$$\begin{aligned}
J_{\phi_3} &= H_{\theta_4} \Big|_{r=a_3} = -\frac{E_0 \sin \phi}{\omega \mu_4 a_3 \sin \theta} \sum_{n=1}^{\infty} \left\{ a_n J_n(k_4 a_3) \right. \\
&\quad \left. + r_n \hat{H}_n^{(2)}(k_4 a_3) \right\} P_n^1(\cos \theta) \\
&\quad + \frac{E_0 \sin \phi}{j \omega \mu_4 a_3} \sum_{n=1}^{\infty} \left\{ a_n \hat{J}'_n(k_4 a_3) + s_n \hat{H}_n^{(2)'}(k_4 a_3) \right\} \frac{d}{d\theta} P_n^1(\cos \theta)
\end{aligned}
\tag{3.44b}$$

$$\begin{aligned}
M_{\theta_3} &= E_{\phi_4} \Big|_{r=a_3} = \frac{E_0 \sin \phi}{k_4 a_3} \sum_{n=1}^{\infty} \left\{ a_n \hat{J}_n(k_4 a_3) \right. \\
&\quad \left. + s_n \hat{H}_n^{(2)}(k_4 a_3) \right\} \frac{d}{d\theta} P_n^1(\cos \theta) \\
&\quad - \frac{E_0 \sin \phi}{j k_4 a_3 \sin \theta} \sum_{n=1}^{\infty} \left\{ a_n \hat{J}'_n(k_4 a_3) \right. \\
&\quad \left. + r_n \hat{H}_n^{(2)'}(k_4 a_3) \right\} P_n^1(\cos \theta)
\end{aligned}
\tag{3.44c}$$

$$\begin{aligned}
M_{\phi_3} = -E_{\theta_4} \Big|_{r=a_3} &= \frac{E_0 \cos \phi}{r_4 a_3 \sin \theta} \sum_{n=1}^{\infty} \left\{ a_n \hat{J}_n(k_4 a_3) \right. \\
&+ s_n \hat{H}_n^{(2)}(k_4 a_3) \left. \right\} P_n^1(\cos \theta) \\
&- \frac{E_0 \cos \phi}{j k_4 a_3} \sum_{n=1}^{\infty} \left\{ a_n \hat{J}'_n(k_4 a_3) \right. \\
&+ r_n \hat{H}_n^{(2)'}(k_4 a_3) \left. \right\} \frac{d}{d\theta} P_n^1(\cos \theta). \tag{3.44d}
\end{aligned}$$

Equations (3.44) thus give the surface currents on the outermost layer. The infinite summation is truncated to a finite number, after ascertaining the numerical convergence.

3.3 Numerical Results

The numerical procedure described in Section 3.1 for a layered dielectric body of revolution has been incorporated into a computer code. The resultant computer code is hereafter referred to as "LDBR". We compare the numerical results from the code LDBR with the solution for the layered sphere developed in Section 3.2. After establishing the code, additional geometries for which exact solutions are not available are considered.

The various scattering models considered are assumed to be illuminated by a uniform plane wave travelling in the positive z-direction. Since a plane wave incident along the axis of a body of revolution excites only the $n=1$ Fourier mode with $e^{+j\phi}$ variation, the currents on the surface have the form [11]

$$\bar{J}(t, \phi) = J_t(t) \cos \phi + j J_\phi(t) \sin \phi$$

$$\bar{M}(t, \phi) = j M_t(t) \sin \phi + M_\phi(t) \cos \phi$$

where

$$J_p(t) = 2 J_p^\theta(t)$$

$$, p = t \text{ or } \phi ,$$

$$M_p(t) = 2 M_p^\theta(t)$$

and where J_p^θ and M_p^θ are the electric and magnetic currents resulting from a θ -polarized incident field with a circumferential variation of the form $e^{j\phi}$. The figures in this section show J_t and M_ϕ in the $\phi = 0^\circ$ plane, while J_ϕ and M_t are in the $\phi = 90^\circ$ plane.

As a check on the accuracy of the iterative computations, we have considered some cases wherein the scatterer

is made up of dummy layers. That is, the entire scatterer, though homogeneous, is treated numerically as being made up of layers, each layer with the same material parameters. Fig. 3.5 indicates the currents on a sphere of "vacuum dielectric." In view of the equivalence theorem, the currents on the surface should obviously be

$$\vec{M} = -\hat{n} \times \vec{E}^{inc}$$

$$\vec{J} = \hat{n} \times \vec{H}^{inc} .$$

One notes that the results obtained from LDBR code agree well with the expected values. Fig. 3.6 indicates the currents on a dielectric sphere of dielectric constant $\epsilon_r = 2$, again made up of dummy layers. It is seen that the eigenfunction solution and the LDBR solution agree favorably. The results are also in good agreement with those of Wu [14] and Glisson [11], who have studied the homogeneous dielectric sphere. Fig. 3.7 indicates the equivalent surface currents obtained from LDBR for a homogeneous sphere with $\epsilon_r = 1$ and various values for the conductivity. The electric currents on a perfect electrically conducting sphere [15] are plotted for comparison. Fig. 3.8 indicates

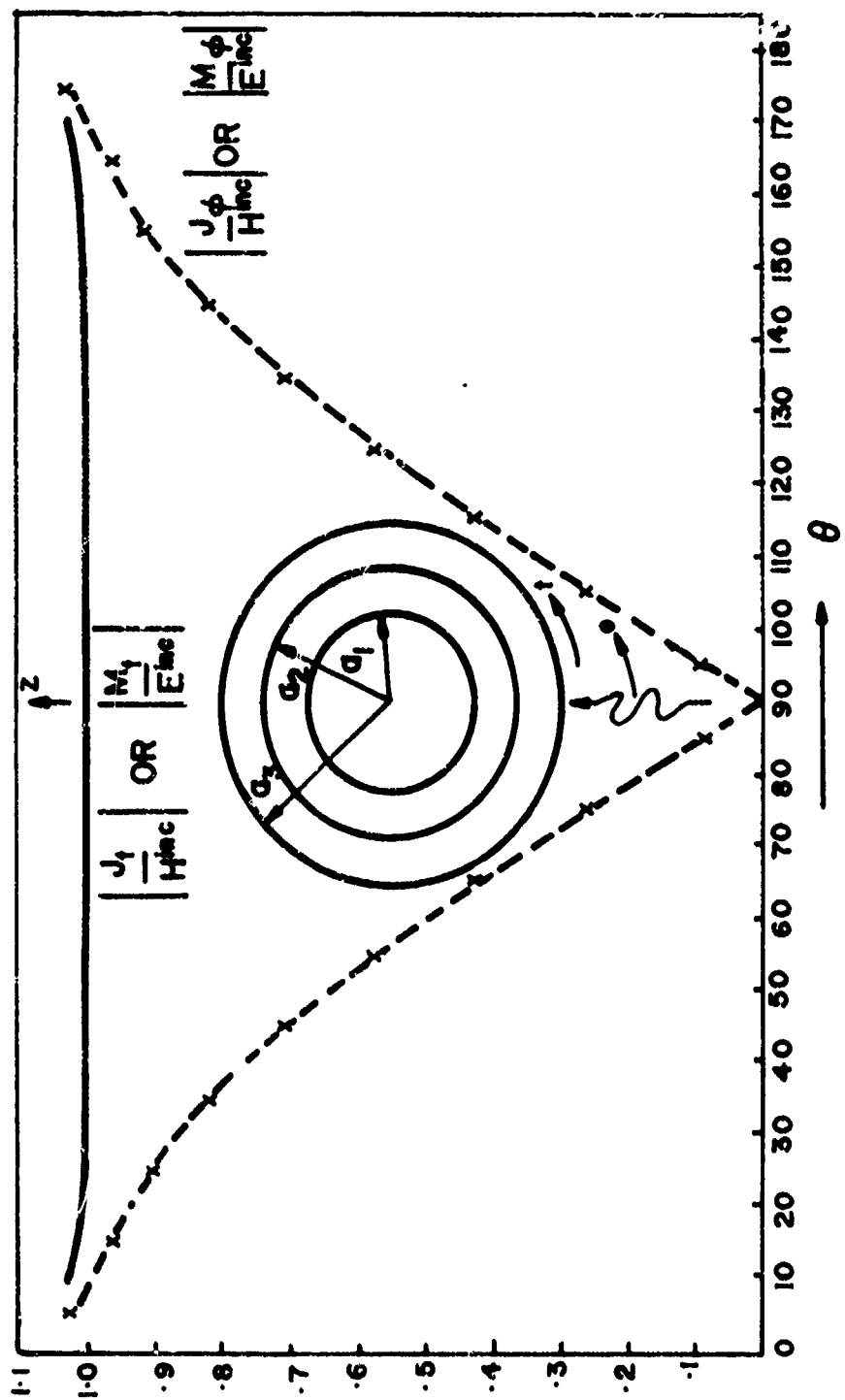


Figure 3.5. Electric and magnetic surface current distribution on a "vacuum dielectric" sphere. $a_1 = 0.4m$, $a_2 = 0.75m$, $a_3 = 1.0m$, $\lambda_0 = 1.0m$.

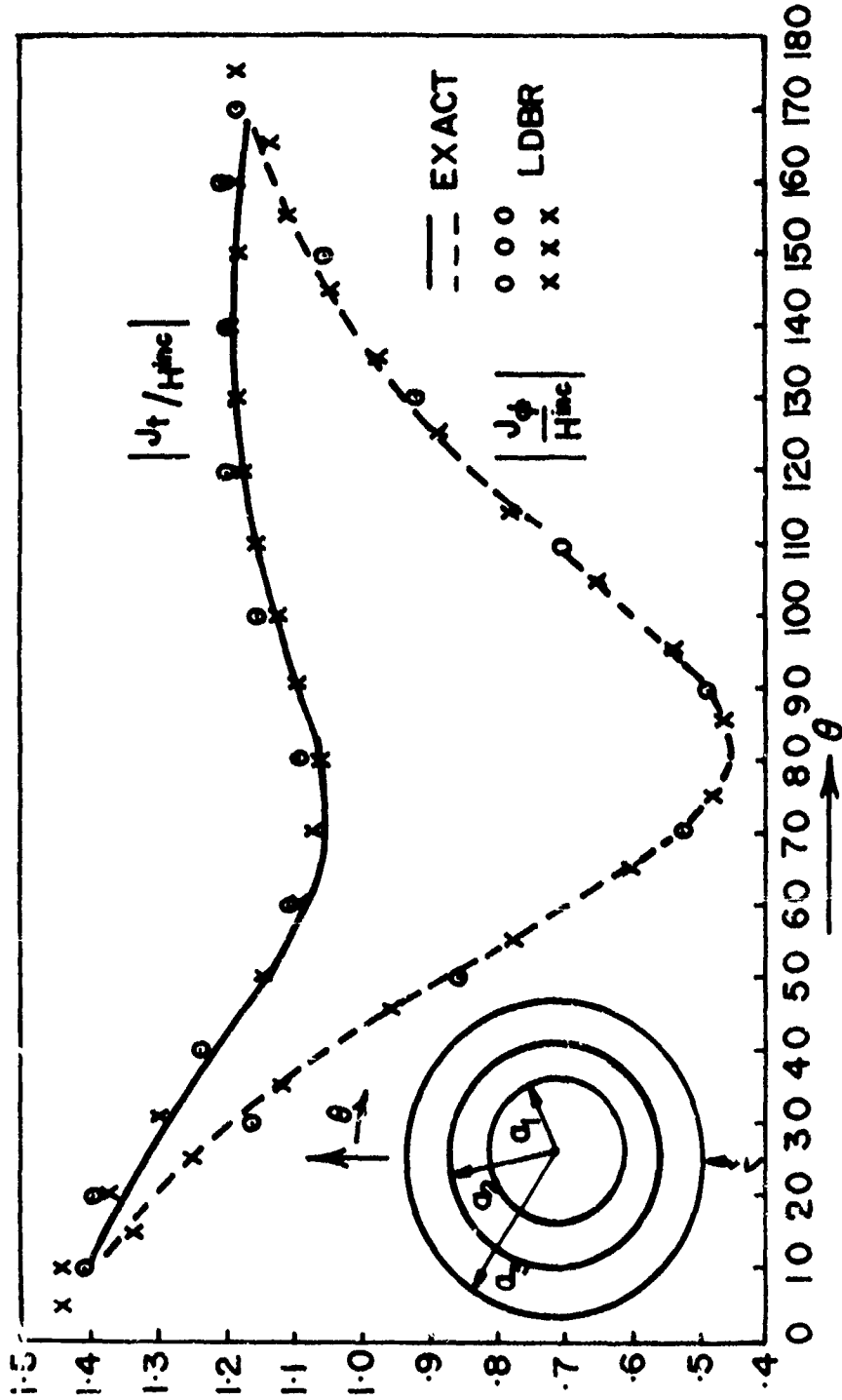


Figure 3.6a. Electric surface current distribution on a homogeneous dielectric sphere, $a_1=0.5m$, $a_2=0.75m$, $a_3=1.0m$, $\lambda_0=1.0m$, $\epsilon_r=2.0$

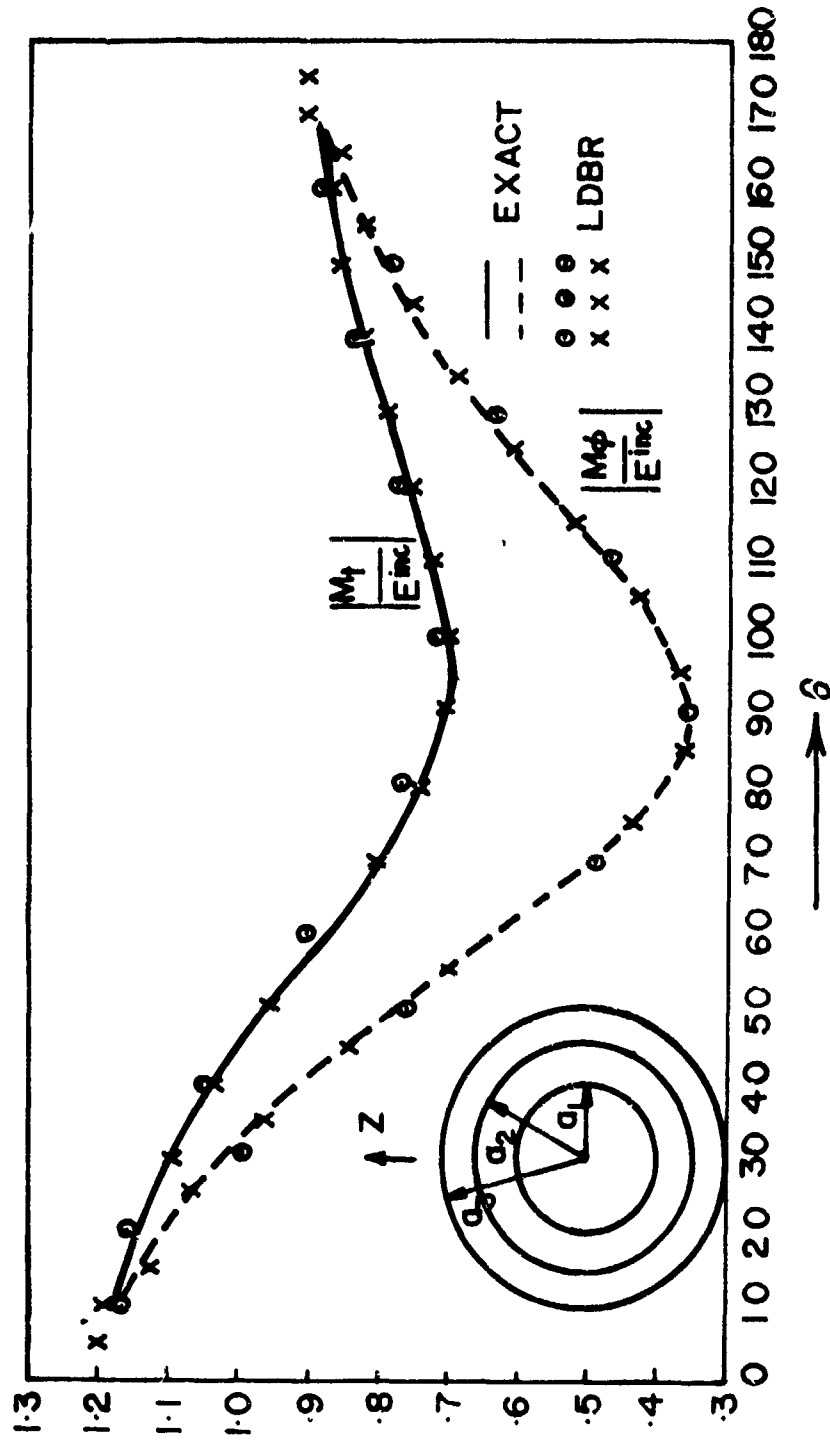


Figure 3.6b. Magnetic current distribution on the homogeneous dielectric sphere in Figure 3.6a.

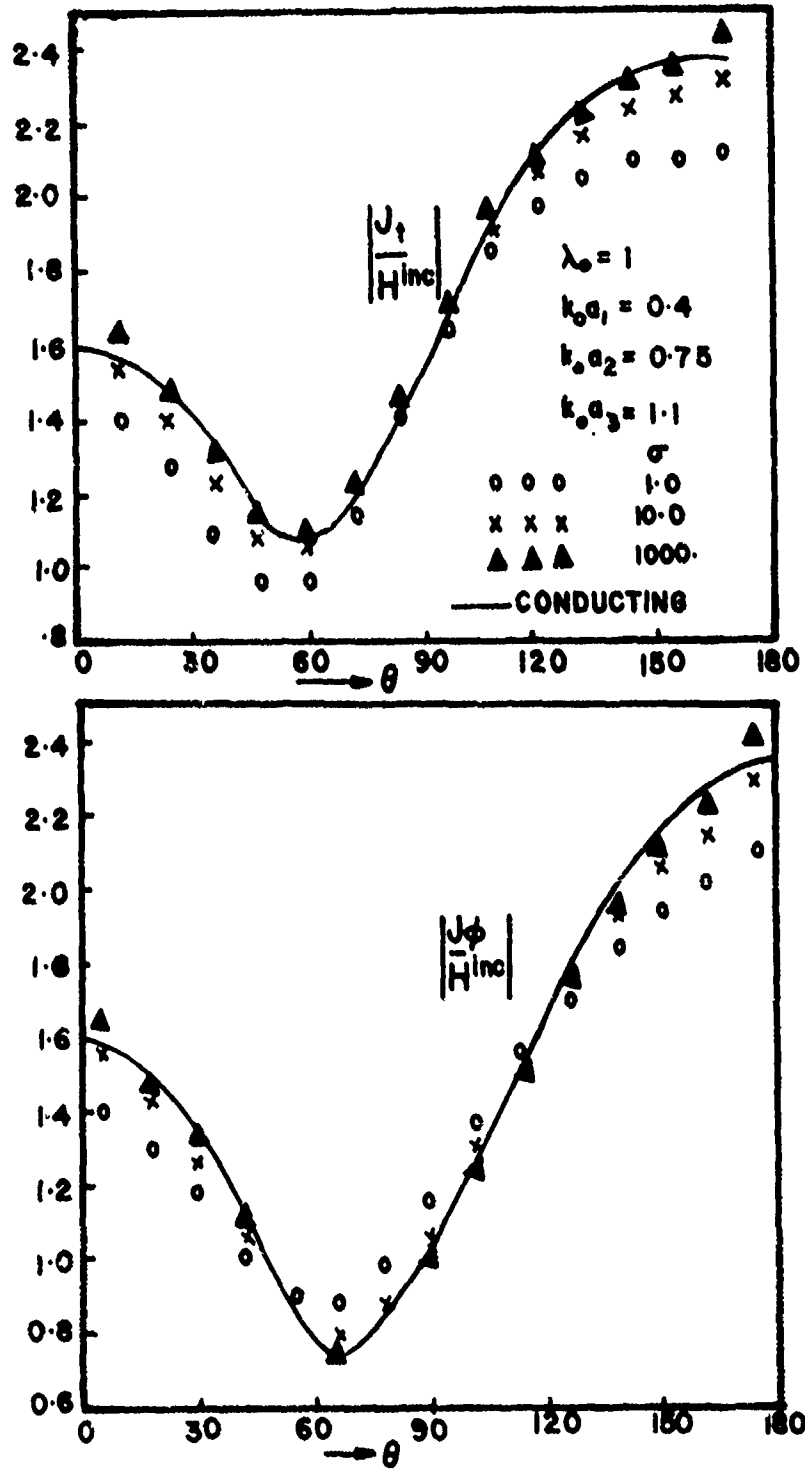


Figure 3.7a. Electric currents on a sphere for various conductivities.

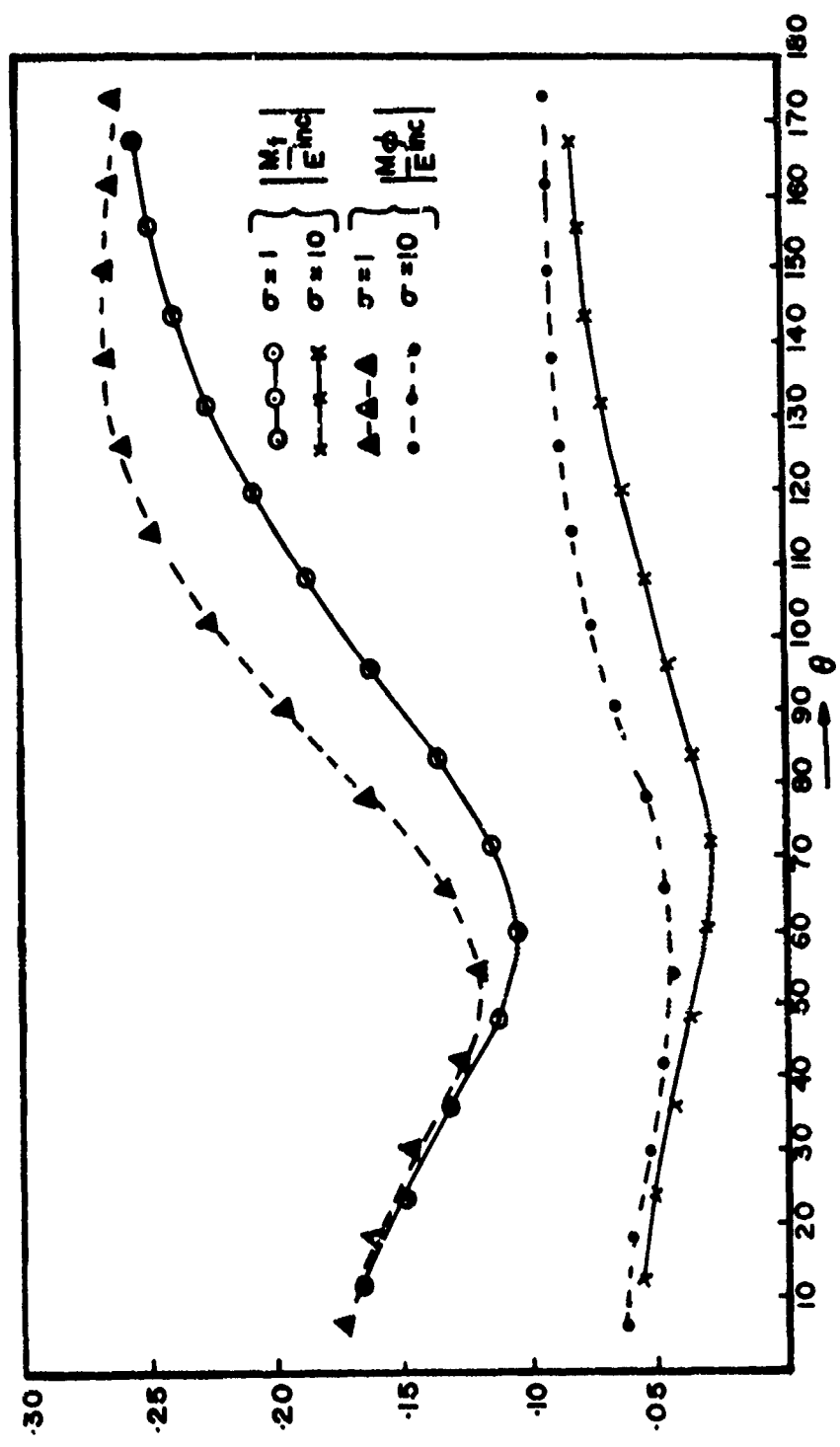


Figure 3.7b. Magnetic currents for $\sigma = 1$ and $\sigma = 10$ for $\phi = 1$ and $\phi = 10$ degrees.

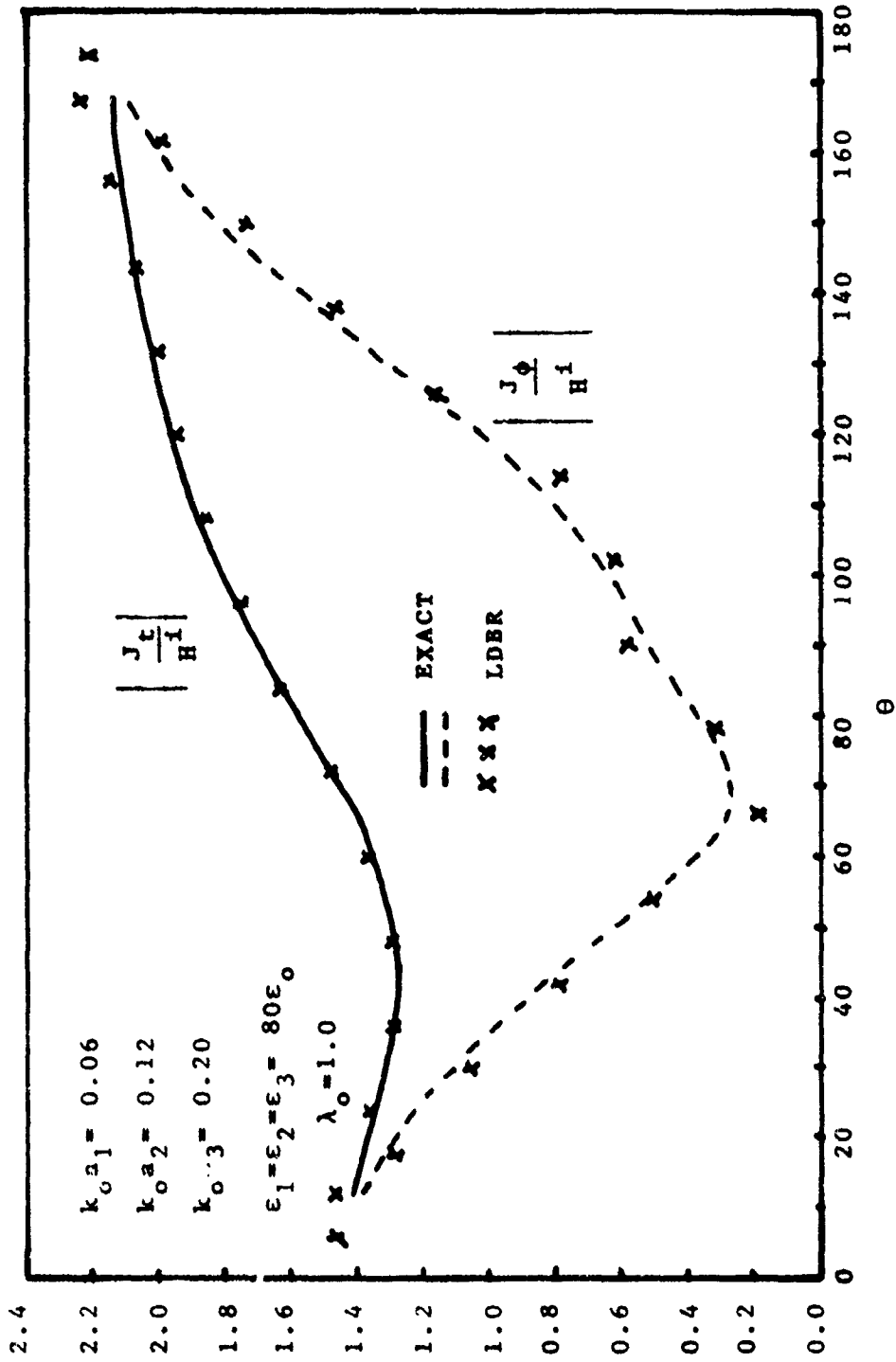


Figure 3.8a. Electric currents on a sphere of high dielectric constant. $k_{0a_1} = 0.06$, $k_{0a_2} = 0.12$, $k_{0a_3} = 0.20$, $\epsilon_r = 80$, $\sigma = 0$, $\lambda_0 = 1.0m$.

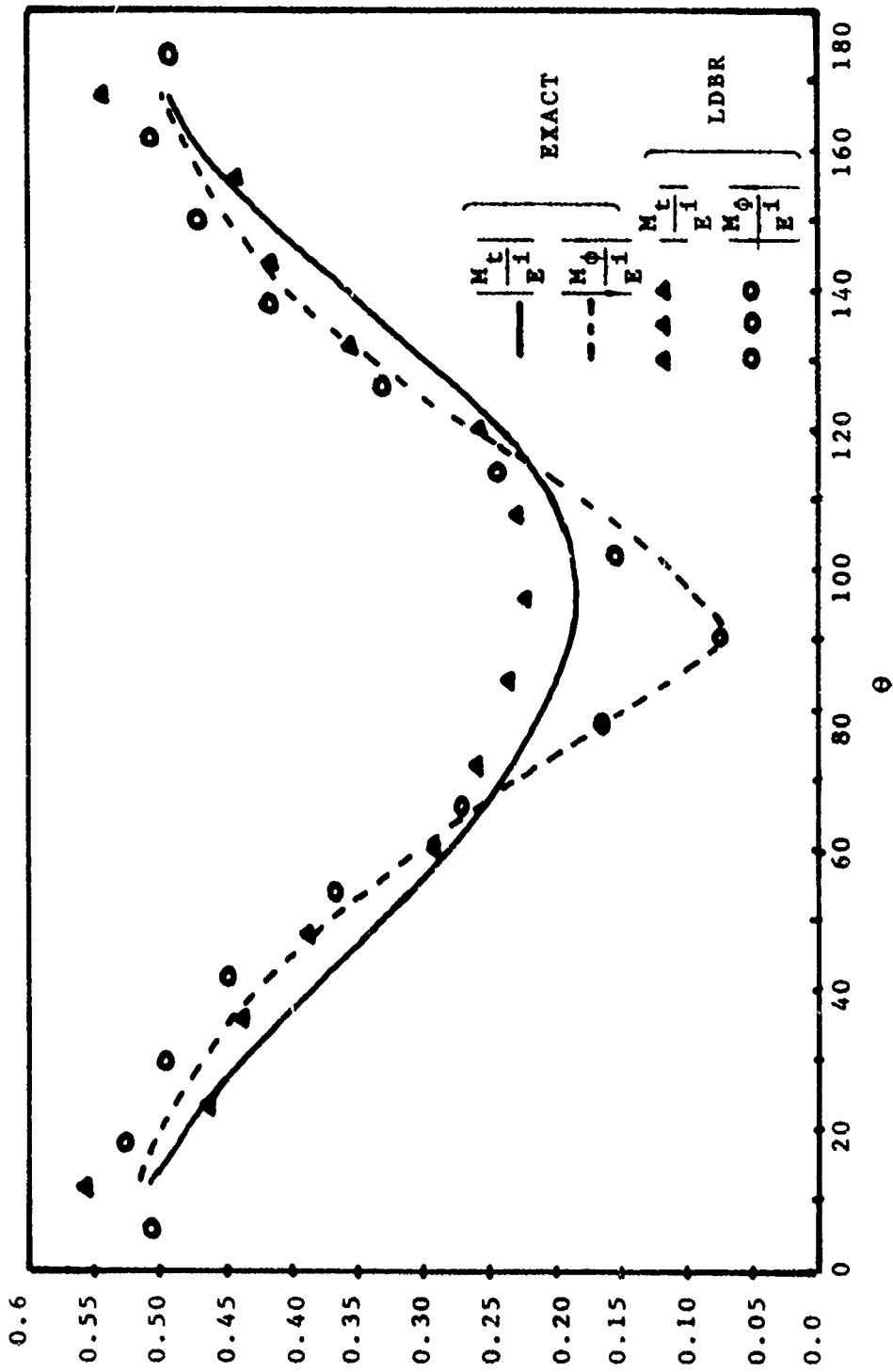


Figure 3.8b. Magnetic currents on the homogeneous sphere of Figure 3.8a.

the currents computed using LDBR and the eigenfunction solution procedure for a lossless sphere of $\epsilon_r = 80$, to illustrate the capability of the computer code to treat "dummy" layers with high dielectric constants. Fig. 3.9 and Fig. 3.10 show currents computed on an inhomogeneous sphere with different medium parameters on each layer. The results of LDBR code agree very well with those obtained from the eigenfunction solution procedure. It should be noted that the values of conductivity chosen for all the cases considered here are rather small. This is because the spherical Bessel functions of complex argument grow exponentially with increasing conductivity. In fact, with only moderate conductivities, the function values exceed the dynamic range of the computer used to perform the calculations. However, the code LDBR does not suffer from this limitation. Although the LDBR results for conductivities thus cannot be checked with those of the eigenfunction formulation, nevertheless, the LDBR results do converge as has been found by increasing the number of sample points on the layers. Calculations have also been carried out for the case of the inhomogeneous sphere in Fig. 3.9, in which additional dummy layers have been inserted within the homogeneous regions. It has been found that treating the three region problem in Fig. 3.9 as a five-layered sphere (i.e.

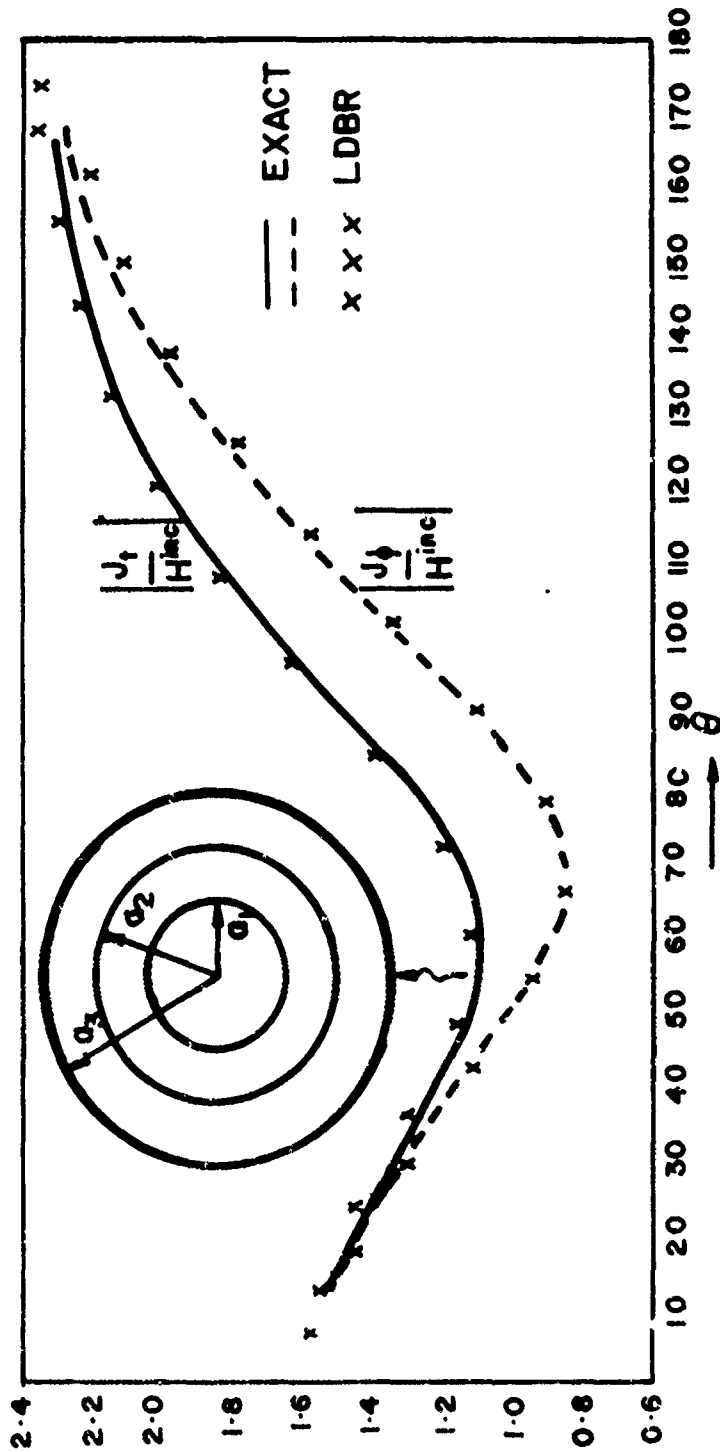


Figure 3.9a. Electric currents on an inhomogeneous sphere. $k_{o1} = 0.4$, $k_{o2} = 0.75$,
 $k_{o3} = 1.0$, $\epsilon_{r1} = \epsilon_{r2} = \epsilon_{r3} = 4.0$, $\sigma_1 = 1.0$ S/m, $\sigma_2 = 2.0$ S/m, $\sigma_3 = 4.0$ S/m.

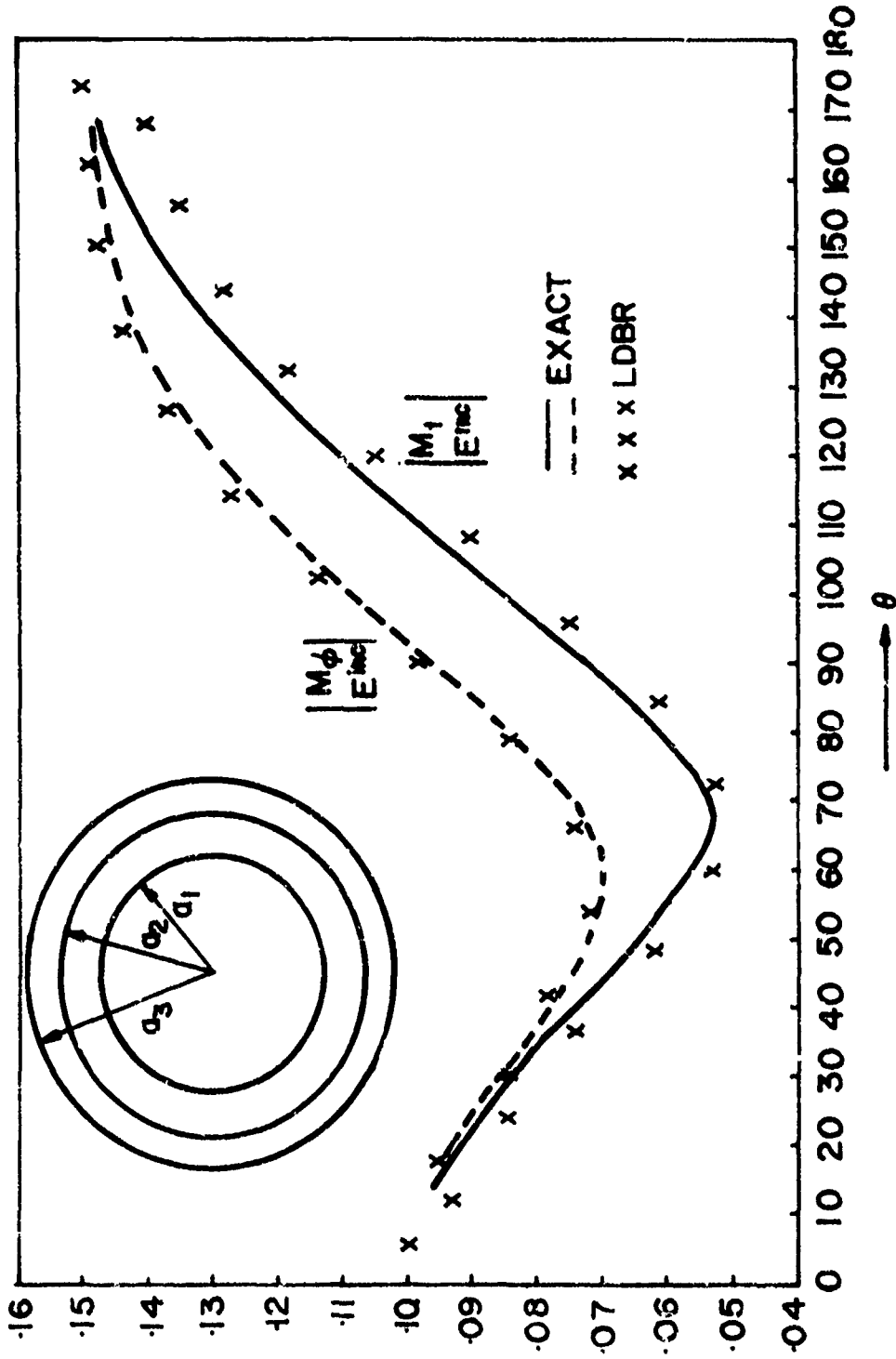


Figure 3.9b. Magnetic currents on the inhomogeneous sphere of Figure 3.9a.

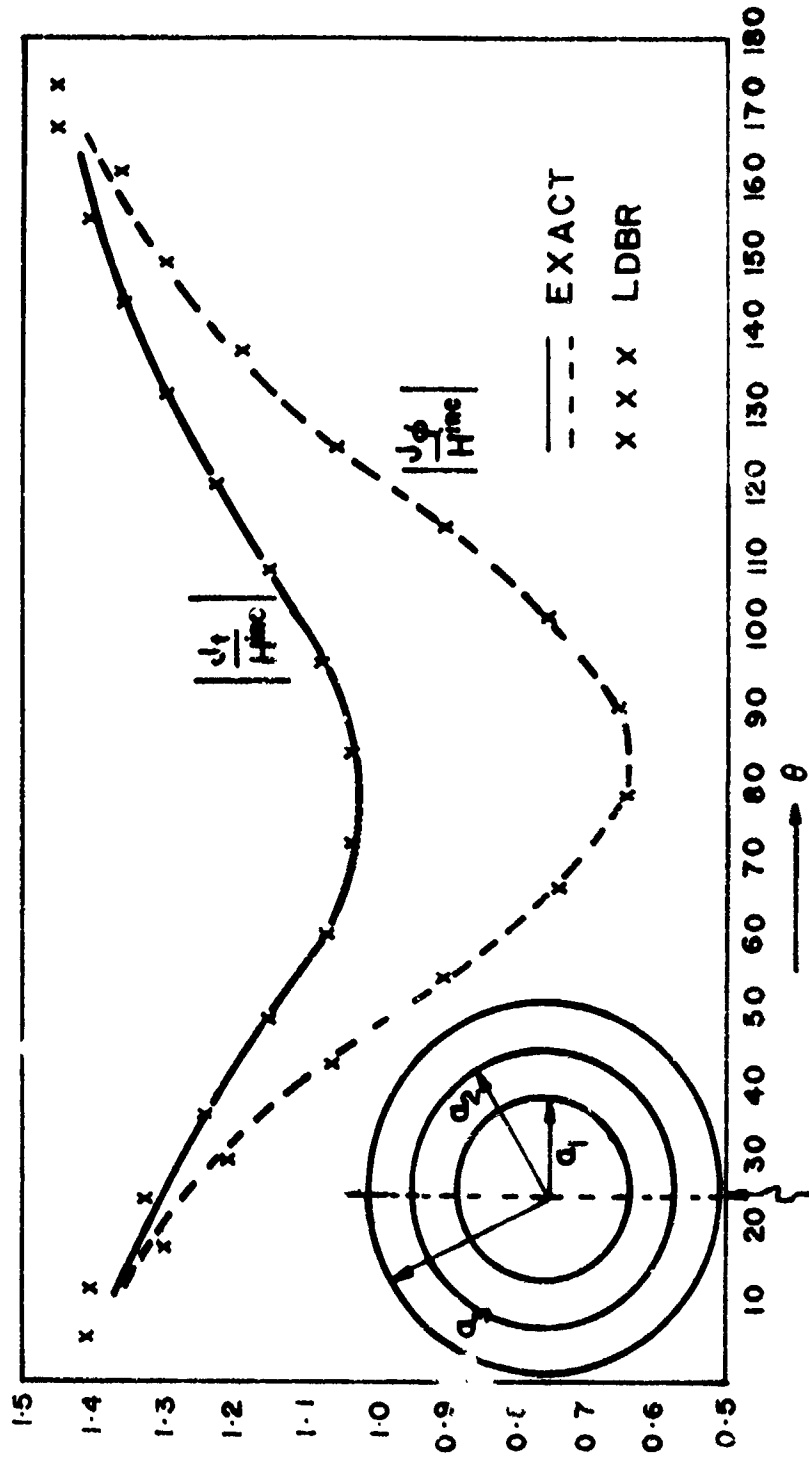


Figure 3.10a. Electric current distribution on an inhomogeneous sphere. $a_1 = 0.4m$, $a_2 = 0.75m$, $a_3 = 1.0m$, $\epsilon_{r1} = 2$, $\epsilon_{r2} = 3$, $\epsilon_{r3} = 4$, $\sigma_1 = \sigma_2 = \sigma_3 = 0.0$, $\lambda_0 = 1.0m$.

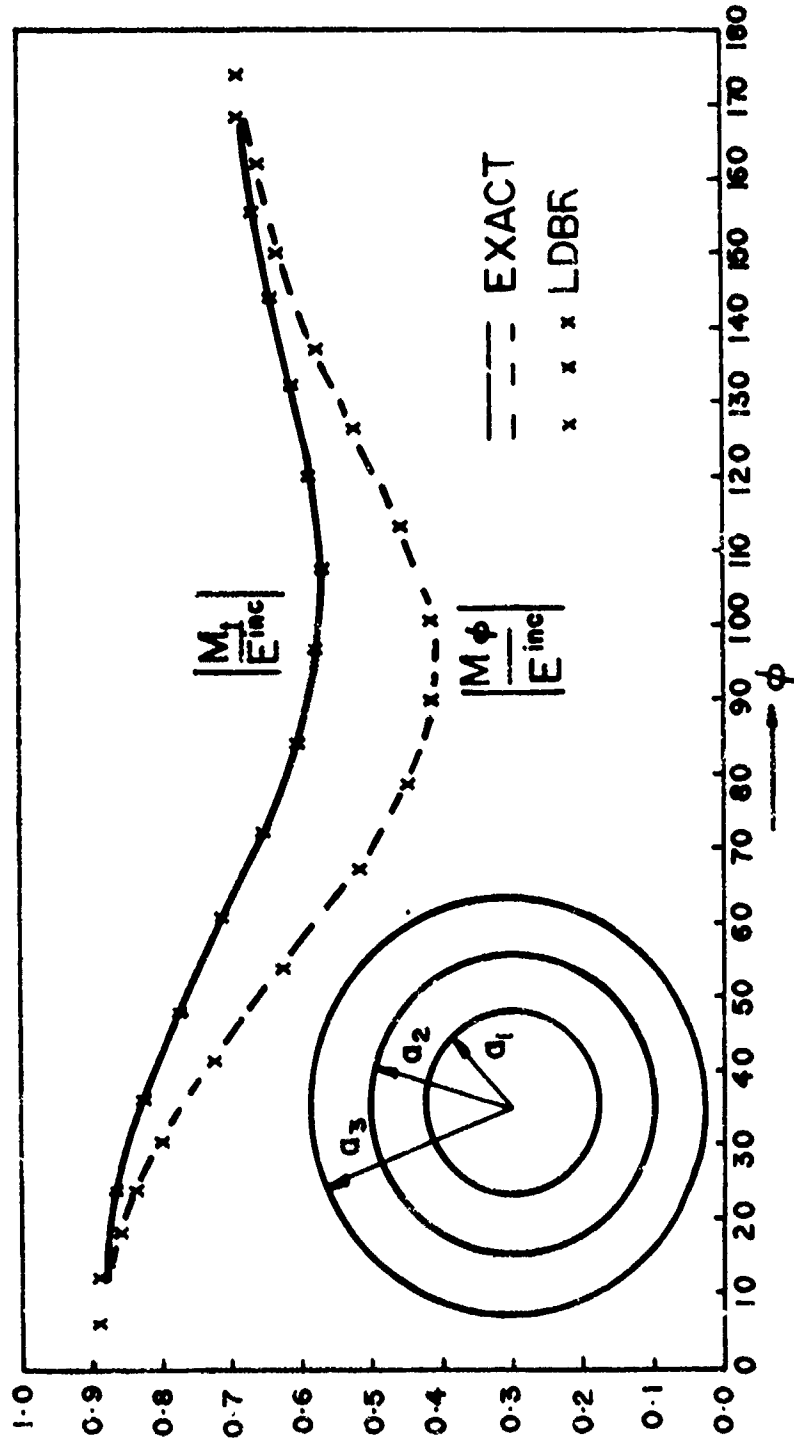


Figure 3.10b. Magnetic currents on the inhomogeneous sphere of Figure 3.10a.

two layers are dummy layers) has yielded results that are in excellent agreement with those obtained using but three layers. Fig. 3.11 shows the currents on a three layered inhomogeneous sphere wherein the outermost layer is chosen to be very thin. One notes that the results of the LDBR code are still in good agreement with those of the eigenfunction solution even for a body made up of thin layers.

We finally consider some additional cases. Fig. 3.12 indicates the currents on a finite homogeneous cylinder made up of dummy layers. Note that in this case, the dielectric region has surface edges and hence the equivalent surface currents may be discontinuous or possibly even singular at these edges. Fig. 3.13 indicates the currents on a homogeneous dielectric cone sphere. Also shown is the result obtained by Glisson [16]. One notes immediately the difference in the results near the tip of the cone. This difference is attributed to the layered treatment of the cone sphere body, which introduces a singularity at the cone tip even for source and field points not on the same surface. Although the current expansion scheme we adopt does not match the fields at the tip, nevertheless, the kernels involved will be highly peaked. By performing the integration around the cone tip more accurately, this error is easily eliminated.

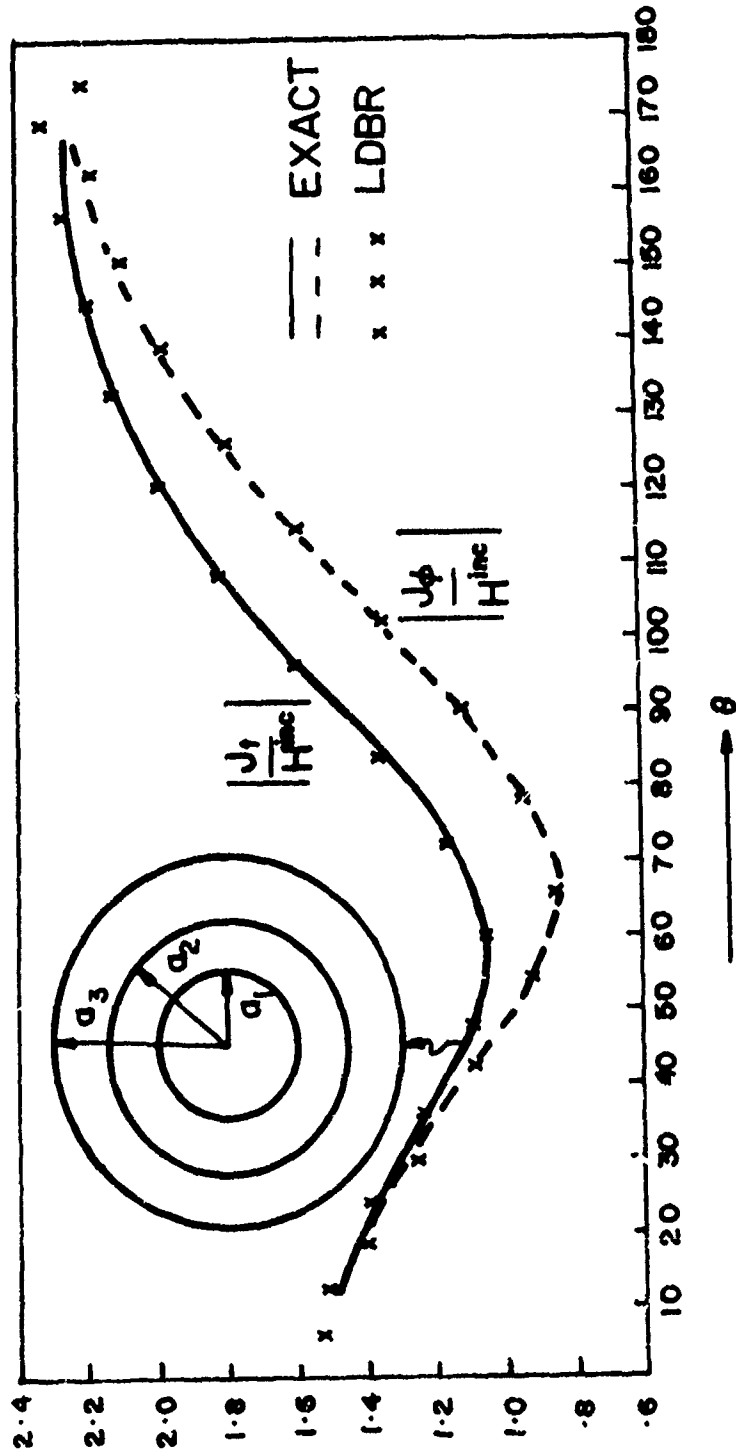


Figure 3.11a. Electric surface current distribution on an inhomogeneous dielectric sphere, $a_1 = 0.5m$, $a_2 = 0.95m$, $a_3 = 1.0m$, $\epsilon_1 = \epsilon_2 = \epsilon_3 = \epsilon_0$, $\sigma_1 = 0.2S/m$, $\sigma_2 = 0.3 S/m$, $\sigma_3 = 0.4 S/m$, $\lambda_0 = 2\pi m$.

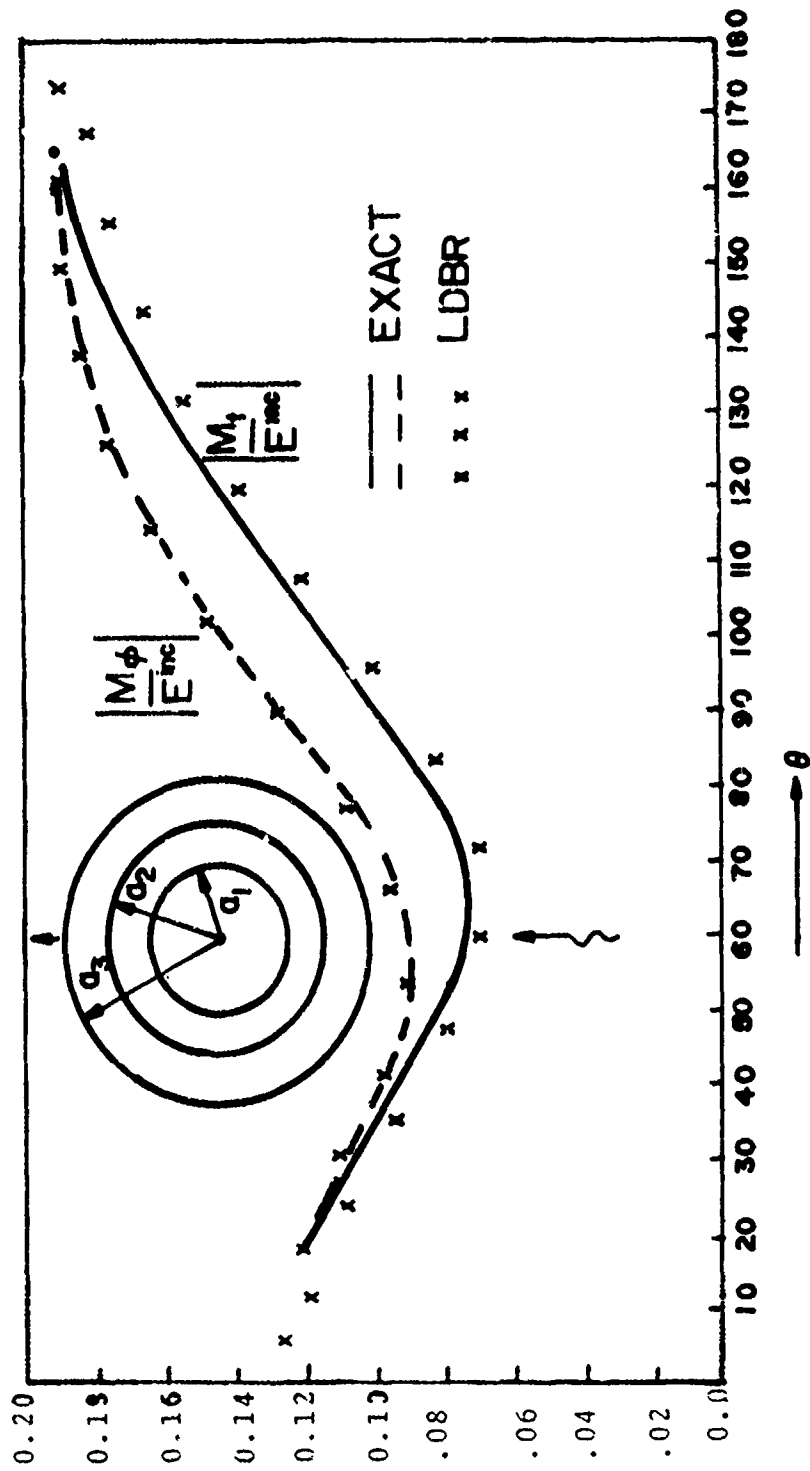


Figure 3.11b. Magnetic currents on the inhomogeneous sphere in Figure 3.11a.

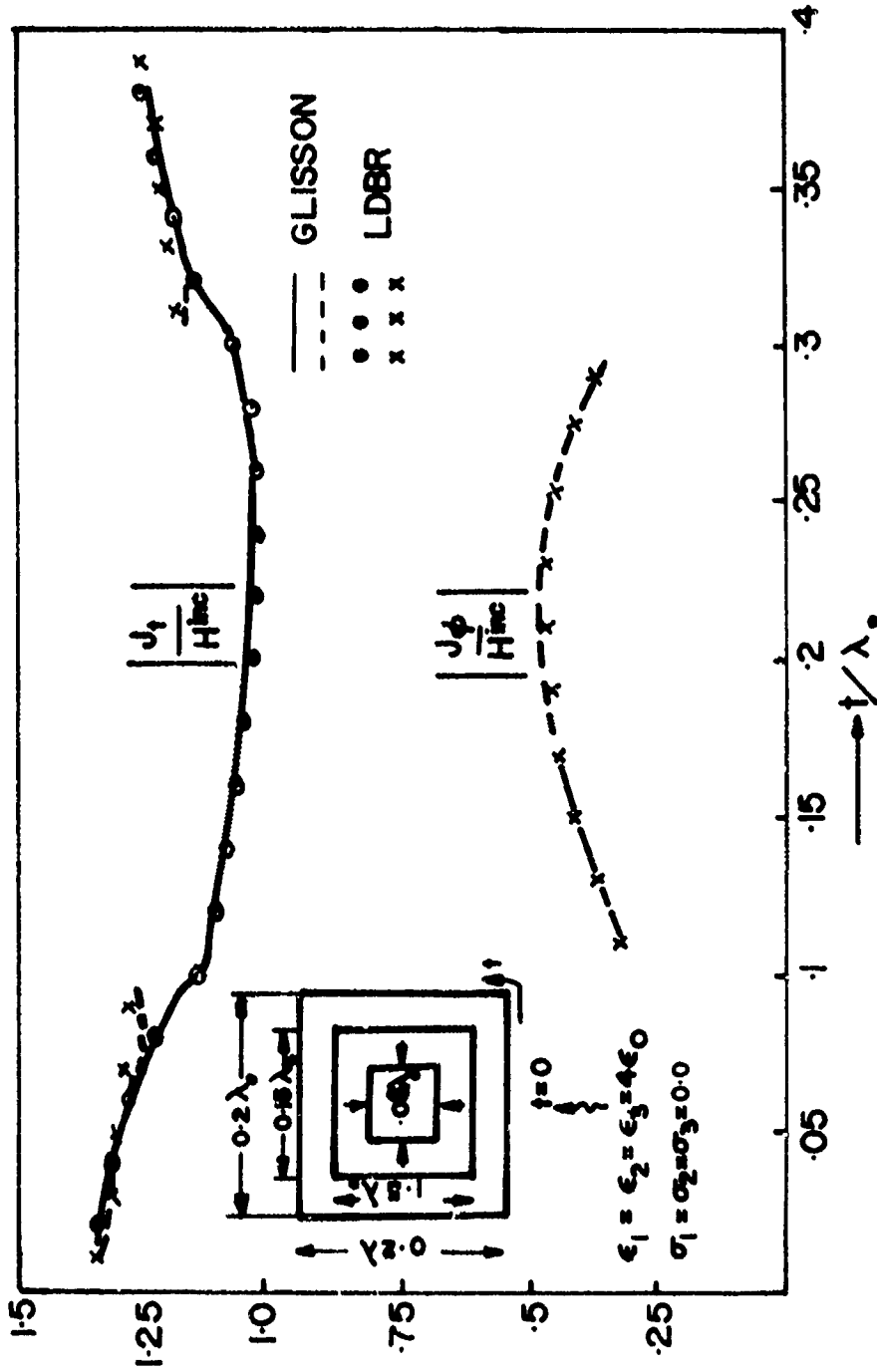


Figure 3.12a. Electric surface current distribution on a finite homogeneous dielectric cylinder.

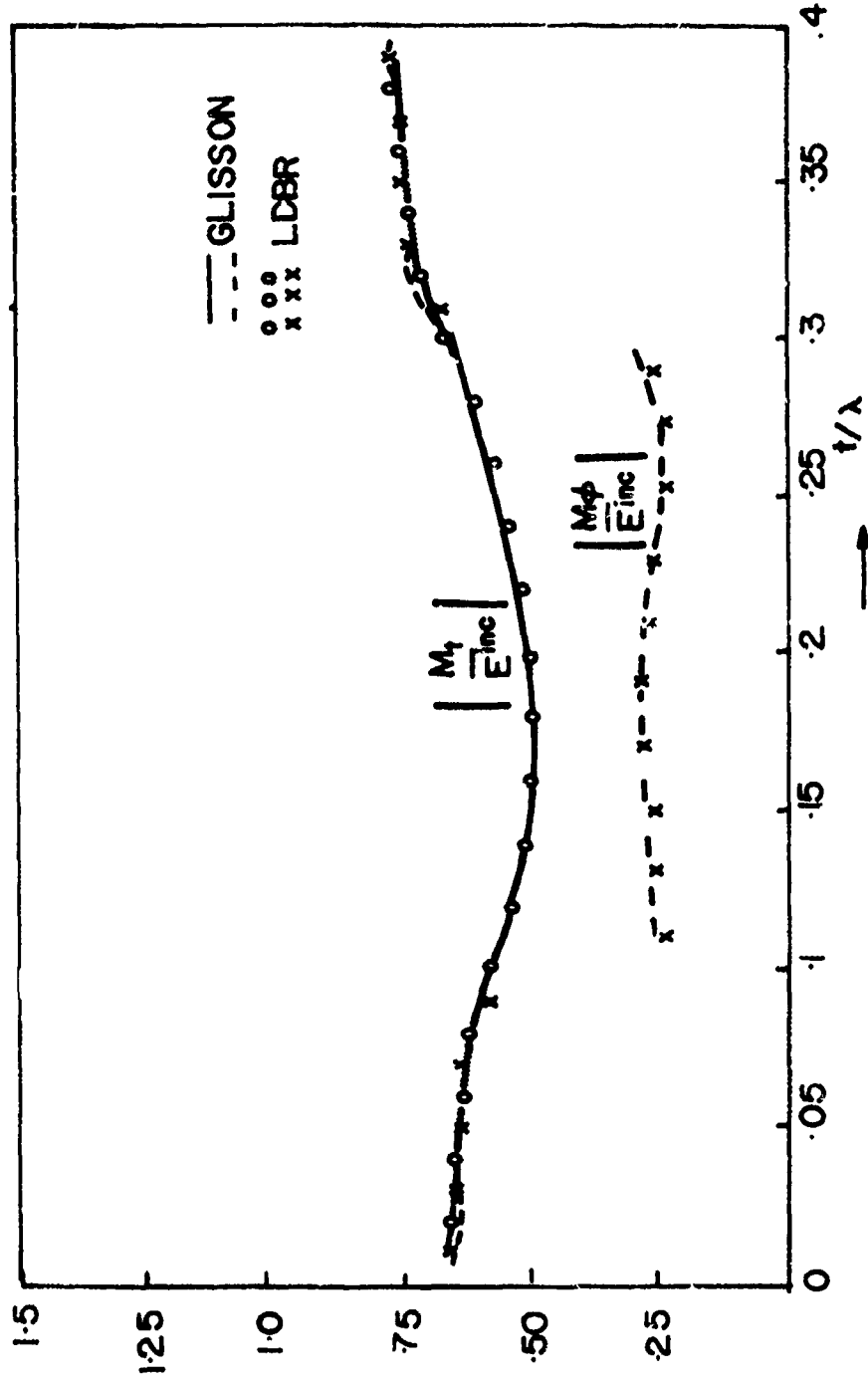


Figure 3.12b. Magnetic current distribution on the finite dielectric cylinder of Figure 3.12a.

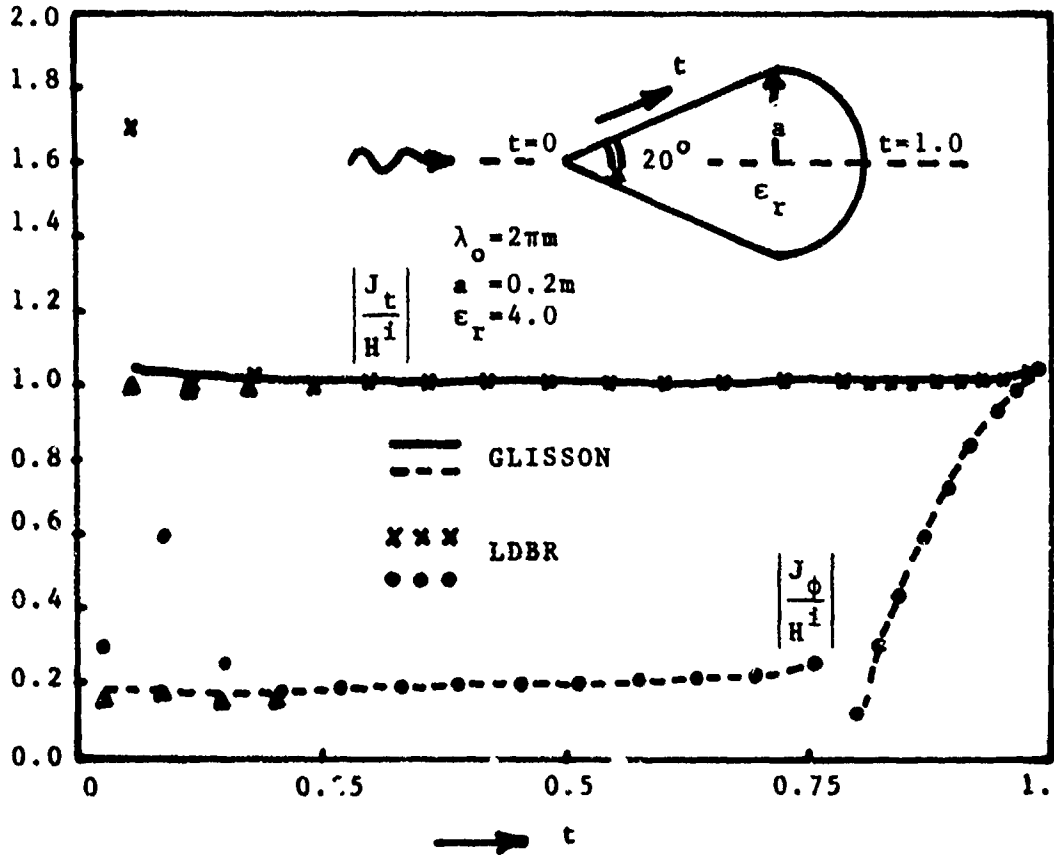


Figure 3.13a. Electric current distribution on a dielectric cone-sphere. $\blacktriangle \blacktriangle \blacktriangle$ indicates results obtained with improved integration around the cone tip.

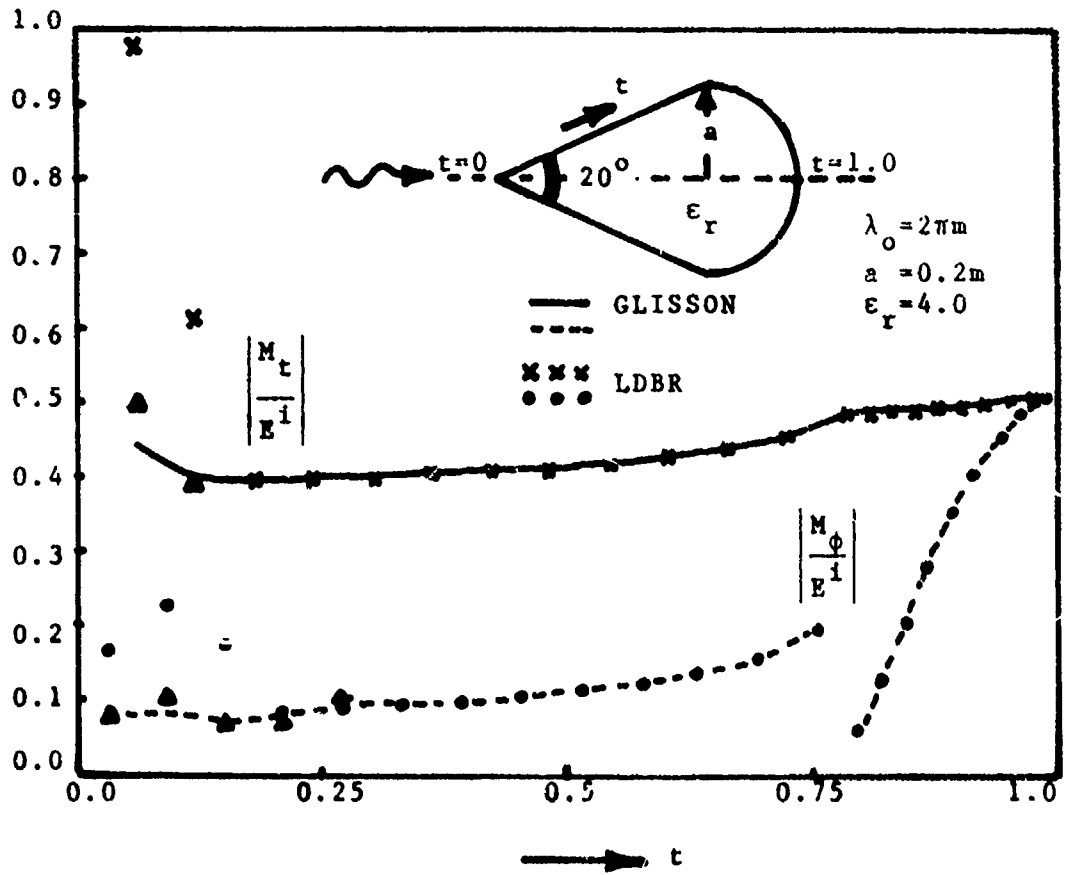


Figure 3.13b. Magnetic currents on the homogeneous cone-sphere in Figure 3.13a.

CHAPTER IV

MISSILE PLUME SCATTERING

In this chapter, the procedure described in Chapter III for obtaining the scattered fields for layered dielectric bodies of revolution is extended to treat a missile with an attached inhomogeneous exhaust plume. Calculated missile currents are presented for selected plume inhomogeneities, frequencies, and angles of incidence.

4.1 Block Tridiagonal Formulation for Missile Plume Scattering

The inhomogeneous plume is modeled as a series of layers of homogeneous regions. Fig. 4.1 shows an approximate model of the missile plume problem. The boundary conditions require that the tangential electric and magnetic fields be continuous across the plume layers and that the tangential electric field vanish along the missile surface and along the missile/plume interface. This leads to a set of coupled integral equations for the equivalent currents on the surfaces between layers of the plume and on the missile and missile/plume interface. The numerical procedure

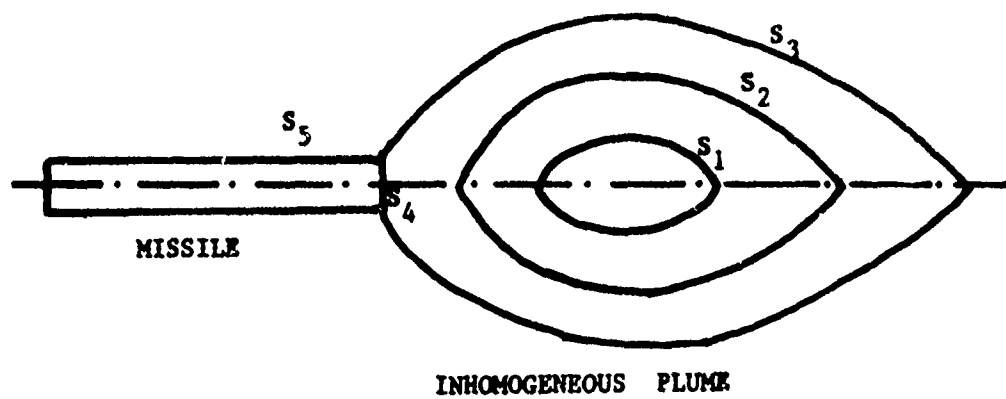


Figure 4.1. Geometry of a missile with a trailing inhomogeneous plume.

indicated in Chapter III leads to a matrix equation for the representative model in Fig. 4.1 as follows:

$$\begin{bmatrix} L_{11} & L_{12} & 0 & 0 & 0 \\ L_{21} & L_{22} & L_{23} & L_{24} & 0 \\ 0 & L_{32} & L_{33} & L_{34} & L_{35} \\ 0 & L_{42} & L_{43} & L_{44} & 0 \\ 0 & 0 & L_{53} & 0 & L_{55} \end{bmatrix} \begin{bmatrix} I_1 \\ I_2 \\ I_3 \\ I_4 \\ I_5 \end{bmatrix} = \begin{bmatrix} 0 \\ 0 \\ v_3^{inc} \\ 0 \\ v_4^{inc} \end{bmatrix}, \quad (4.1)$$

where

$$I_i = \begin{bmatrix} \bar{J}_i \\ \bar{M}_i \end{bmatrix}, \quad i = 1, 2, 3$$

$$I_i = [\bar{J}_i], \quad i = 4, 5$$

$$v_3^{inc} = \begin{bmatrix} \bar{E}_{3 \tan}^{inc} \\ \bar{H}_{3 \tan}^{inc} \end{bmatrix}, \quad v_5^{inc} = [\bar{E}_{5 \tan}^{inc}],$$

and L_{ij} are the coupling matrices whose elements correspond

to the field contribution on surface i due to currents on surface j . An immediate observation of (4.1) is that the block tridiagonal nature of the overall system matrix now appears to have been lost with the presence of the missile. However, we merely regroup some of the operators, currents and driving vectors as follows:

$$L'_{23} = [L_{23} \quad L_{24} \quad 0]$$

$$L'_{32} = \begin{bmatrix} L_{32} \\ L_{42} \\ 0 \end{bmatrix}$$

$$L'_{33} = \begin{bmatrix} L_{33} & L_{34} & L_{35} \\ L_{43} & L_{44} & 0 \\ L_{53} & 0 & L_{55} \end{bmatrix}$$

$$v^{inc} = \begin{bmatrix} v_3^{inc} \\ 0 \\ v_5^{inc} \end{bmatrix}, \quad I'_3 = \begin{bmatrix} I_3 \\ I_4 \\ I_5 \end{bmatrix}$$

With these new definitions, (4.1) may be written as

$$\begin{bmatrix} L_{11} & L_{12} & 0 \\ L_{21} & L_{22} & L'_{23} \\ 0 & L'_{32} & L'_{33} \end{bmatrix} \begin{bmatrix} I_1 \\ I_2 \\ I'_3 \end{bmatrix} = \begin{bmatrix} 0 \\ 0 \\ v^{inc} \end{bmatrix}, \quad (4.2)$$

which retains the block tridiagonal nature. The extension to an arbitrary number of layers should be obvious. Thus with suitable partitioning of the matrix equation, the iteration procedure indicated in Section 2.4 can still be utilized.

4.2 Boundary Conditions at the Plume-Missile Junction

The boundary condition on the conducting missile is that the tangential electric field vanish over the missile surface. On the plume interfaces, however, we require that the tangential electric and magnetic fields be continuous. Thus, at the junction of the plume and the missile, we must have $E_t = 0$ and H_ϕ to be continuous. Since $\bar{J} = \hat{n} \times \bar{H}$ and $\bar{M} = \bar{E} \times \hat{n}$, these conditions translate into conditions on the surface currents which imply that J_t , the t-directed component of the electric current, be continuous as one approaches the junction along any one of the three surfaces meeting there and that M_t , the t-directed component of the magnetic current, vanish at the junction (Here the t-direction is the direction along the generator arc of the

body of revolution). Note, however, that J_ϕ and M_ϕ may be singular near the junction since these currents flow parallel to an edge. With the displaced current expansion scheme (see Fig. 4.2), however, these current components are not defined directly at the junction, but rather a half-subdomain away from the junction. The junction point of the missile and plume is chosen to be at the center of the t -directed current pulse and continuity of the current at the junction is enforced. Note that no special boundary conditions on J_ϕ or M_ϕ at the missile-plume junction are needed because of the shifted subdomain scheme.

In order to apply the boundary conditions on the t -directed component of the electric and magnetic currents, let us consider the equivalent problems, shown in Fig. 4.2, obtained by the application of the equivalence principle. Fig. 4.2a is the exterior equivalence, wherein the fields in the exterior region are only due to equivalent electric currents residing on the missile surface and equivalent electric and magnetic currents residing on the outside of the plume surface. The fields in the interior are assumed to be zero for this part of the problem. Fig. 4.2b shows the internal equivalence, wherein the fields in the exterior region are assumed to be zero. We note herein that the fields on the interior are due to equivalent electric currents residing on

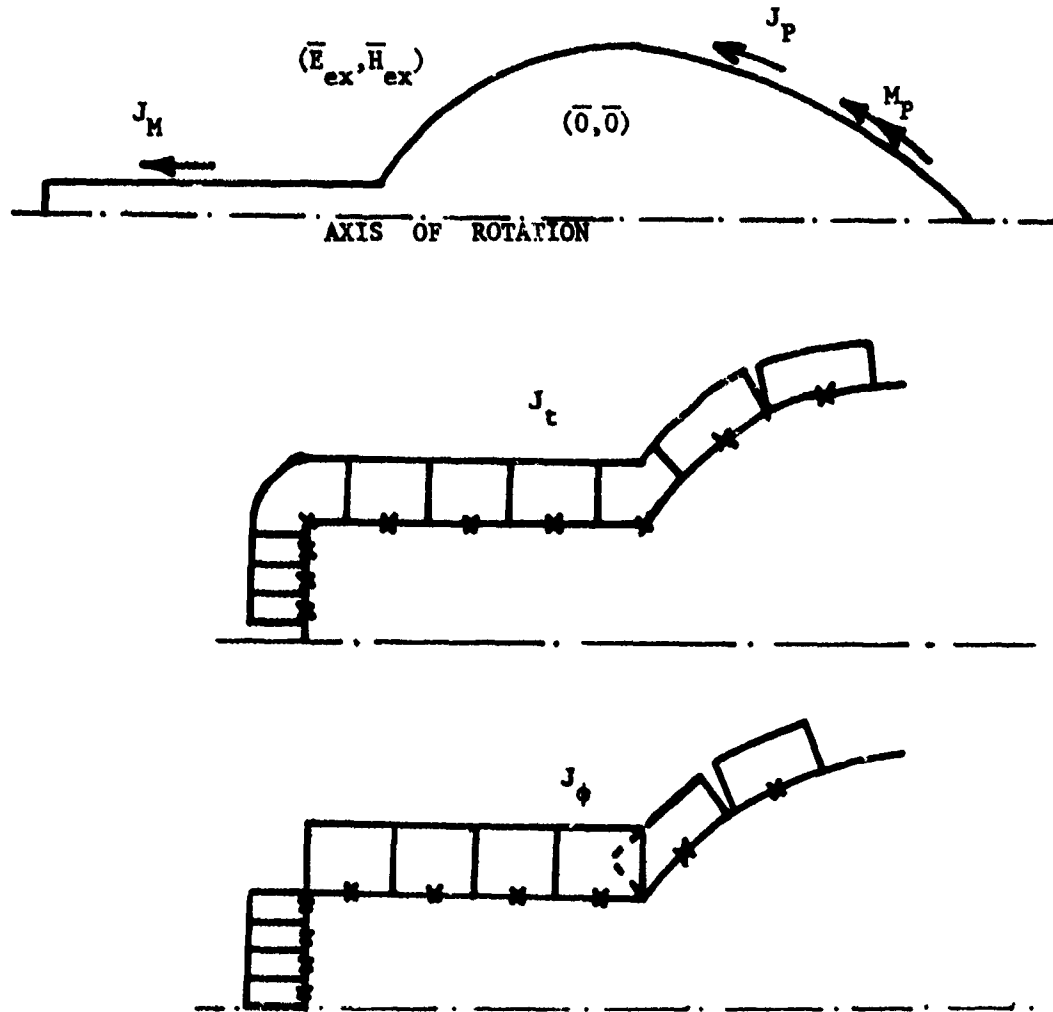


Figure 4.2a. External equivalence and current expansion scheme for the missile plume configuration.

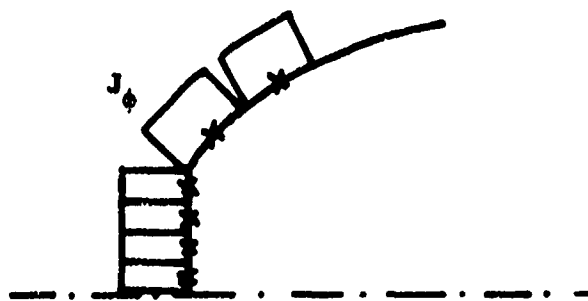
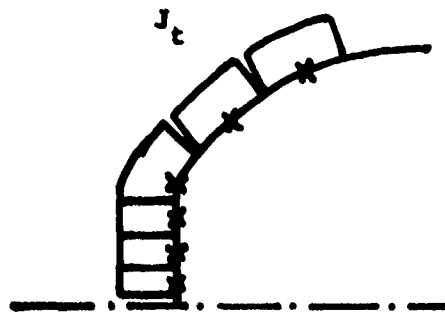
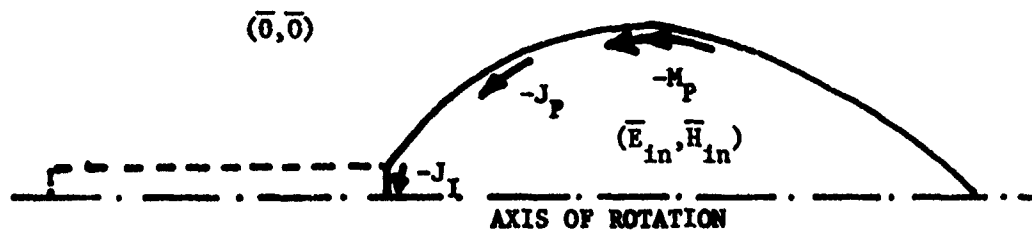


Figure 4.2b. Internal equivalence and current expansion scheme for the missile/plume configuration.

the interface of the missile/plume and due to electric and magnetic currents on the interior of the plume. We also note that the missile current does not appear in this part of the problem. Using the above two equivalent problems, we note that the following are true:

$$\hat{n} \times \bar{E}_{ex}^- (\bar{J}_M, J_{tj}, \bar{J}_P, \bar{M}_P) + \hat{n} \times \bar{E}^{inc} = 0 \quad , \quad (4.3)$$

$$\hat{n} \times \bar{H}_{ex}^- (\bar{J}_M, J_{tj}, \bar{J}_P, \bar{M}_P) + \hat{n} \times \bar{H}^{inc} = 0 \quad , \quad (4.4)$$

$$\bar{r} \in S_P + S_M$$

$$\hat{n} \times \bar{E}_{in}^+ (-\bar{J}_I, J_{tj}, -\bar{J}_P, -\bar{M}_P) = 0 \quad , \quad (4.5)$$

$$\hat{n} \times \bar{H}_{in}^+ (-\bar{J}_I, J_{tj}, -\bar{J}_P, -\bar{M}_P) = 0 \quad , \quad (4.6)$$

$$\bar{r} \in S_P + S_I$$

where S_P , S_M and S_I are the plume, missile and interface surfaces, respectively and

\bar{E}_{ex}^- is the electric field produced by the currents for the exterior equivalence, evaluated just inside the missile/plume surface,

\bar{H}_{ex}^- is the magnetic field produced by the currents for the exterior equivalence, evaluated just inside the missile/plume surface,

\bar{E}_{in}^+ is the electric field produced by the currents for the interior equivalence, evaluated just outside the plume/interface surface,

- \bar{H}_{in}^+ is the magnetic field produced by the currents for the interior equivalence, evaluated just outside the plume/interface surface,
- \bar{J}_M is the electric current on the missile surface,
- \bar{J}_P, \bar{M}_P are the electric and magnetic currents on the plume,
- J_{tj} is the t-component of the electric current at the junction,
- \bar{J}_I is the electric current on the missile/plume interface.

Over the plume surface S_P , (4.3) and (4.5) result in

$$\hat{n} \times \bar{E}_{ex}^- - \hat{n} \times \bar{E}_{in}^+ = -\hat{n} \times \bar{E}^{inc}, \quad \bar{r} \in S_P, \quad (4.7a)$$

Similarly, from (4.4) and (4.6) one obtains

$$\hat{n} \times \bar{H}_{ex}^- - \hat{n} \times \bar{H}_{in}^+ = -\hat{n} \times \bar{H}^{inc}, \quad \bar{r} \in S_P, \quad (4.7b)$$

From (4.3) we have,

$$\hat{n} \times \bar{E}_{ex}^- = -\hat{n} \times \bar{E}^{inc}, \quad \bar{r} \in S_M, \quad (4.8)$$

From (4.5) we have,

$$\hat{n} \times \bar{E}_{in}^+ = 0, \quad \bar{r} \in S_I, \quad (4.9)$$

where \bar{r} refers to the point at which the fields are evaluated. Herein the dependence of the various fields on the appropriate currents are suppressed. Equations (4.7) through (4.9) are the required equations. For computational purpose, the layers are chosen in accordance with the contours of the equivalent problems (see Fig. 4.2). If one uses a testing procedure similar to that used in Chapter III for the layered dielectric body of revolution, the above equations may be

reduced to a matrix equation. At this stage we exercise some caution with regard to the equations associated with the evaluation of the fields at a point due to various current sub-domains. For test points on the plume surface, Equation (4.7) essentially corresponds to the enforcement of the continuity of tangential electric and magnetic fields. Equations (4.8) and (4.9) correspond to the vanishing of the tangential electric fields over the missile surface and interface, respectively. At the junction, the net effect is to add together three equations that correspond to (i) enforcement of continuity of the tangential electric field at the plume/exterior region interface, (ii) the requirement that the tangential electric field vanish on the missile surface, and (iii) the requirement that the tangential electric field vanish at the missile/plume interface. The use of the current expansion scheme shown in Fig. 4.2 along with the above testing procedure results in separate terms in the moment matrix pertaining to the t-directed component of the electric current at the junction. Since these terms correspond to the same unknown, viz. the unknown current coefficient at the junction, they are grouped together. Such a procedure yields an average value of the contribution from the junction current, the averaging being carried out over all the

three surfaces that meet at the junction and thus achieves the continuity of the t-directed component of the electric current at the junction. Since the t-directed magnetic current pulses overlap the t-directed electric current pulses and since the magnetic current on the missile/exterior region interface and the missile/plume interface is zero, the t-directed magnetic current pulse coefficient at the junction is forced to be zero, thus yielding a vanishing t-directed component of magnetic current at the junction.

4.3 Numerical Results

The computer code LDBR, described in Chapter III for solving currents on a layered dielectric body of revolution, was modified to incorporate the procedures described in Section 4.2 which would enable one to solve for the currents on a composite missile-plume structure. This modified code will be hereafter referred to as the MPLM code. Since the composite missile-plume body is thin compared to the length, only the circumferentially uniform Fourier mode ($m = 0$) current is considered. This is because for reasonably thin bodies of revolution the non-symmetric modes are only weakly coupled to the plume and thus these modes of missile current, though perhaps significant by themselves, probably do not

vary much with the plume presence.

Due to the lack of either an exact solution or comparable measured results for the missile/plume geometry, a few special geometries were considered and the results compared with those obtained from other valid computer codes. Figs. 4.3a and 4.3b show the currents on the missile, when the plume conductivity is set to zero. As one would expect upon setting the plume conductivity to zero, the currents induced on the missile should be identical to those induced on a conducting cylinder excited by a plane wave. Also shown for comparison in these figures are the results obtained by a computer code developed by Glisson [16] for the currents induced on a cylinder due to a plane wave illumination. The results of the MPLM code are in excellent agreement with those of Glisson. As a further check, the geometry of a missile with a trailing cylindrical plume (of the same radius as that of the missile) of uniform conductivity $\sigma = 1000 \text{ S/m}$ is considered. In this case, the missile plume combination resembles a perfectly conducting cylinder whose length is the sum of the lengths of the missile and plume. Figs. 4.4a and 4.4b show the circumferentially uniform Fourier mode current on the composite structure. Also shown on these figures are the results obtained by the previously mentioned code of Glisson. We note the excellent

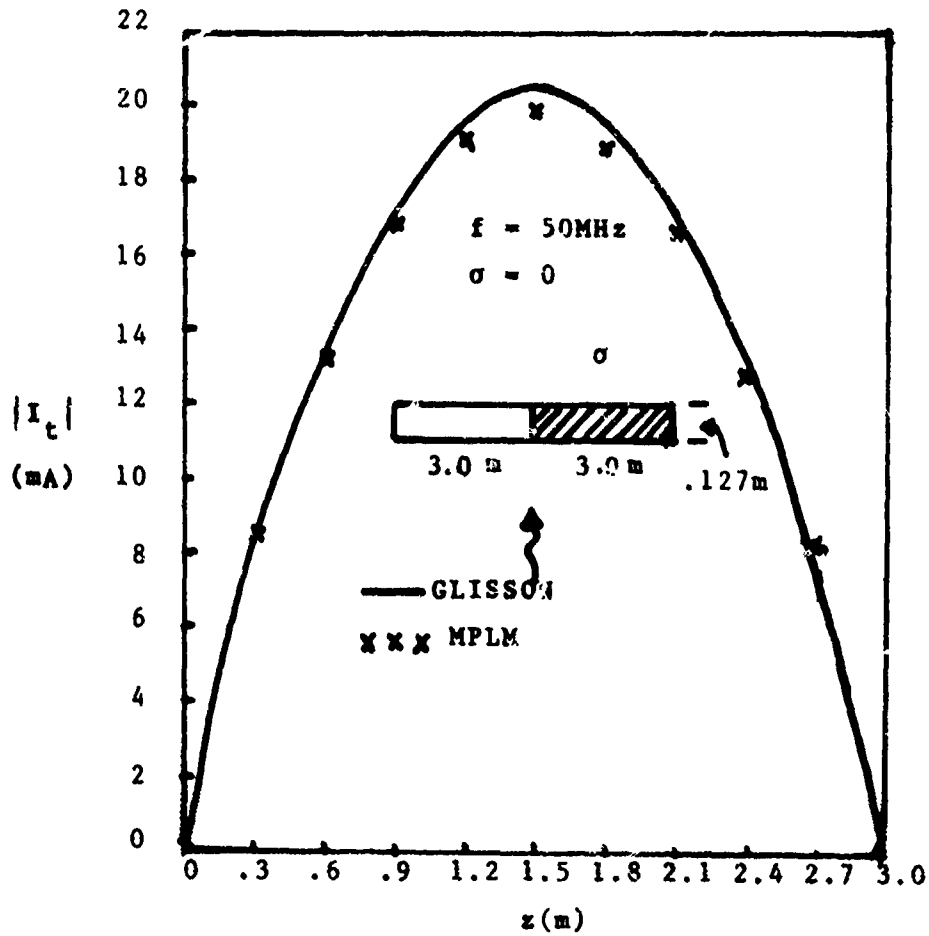


Figure 4.3a. Electric current distribution along a missile with a trailing plume of uniform conductivity $\sigma = 0$ S/m.

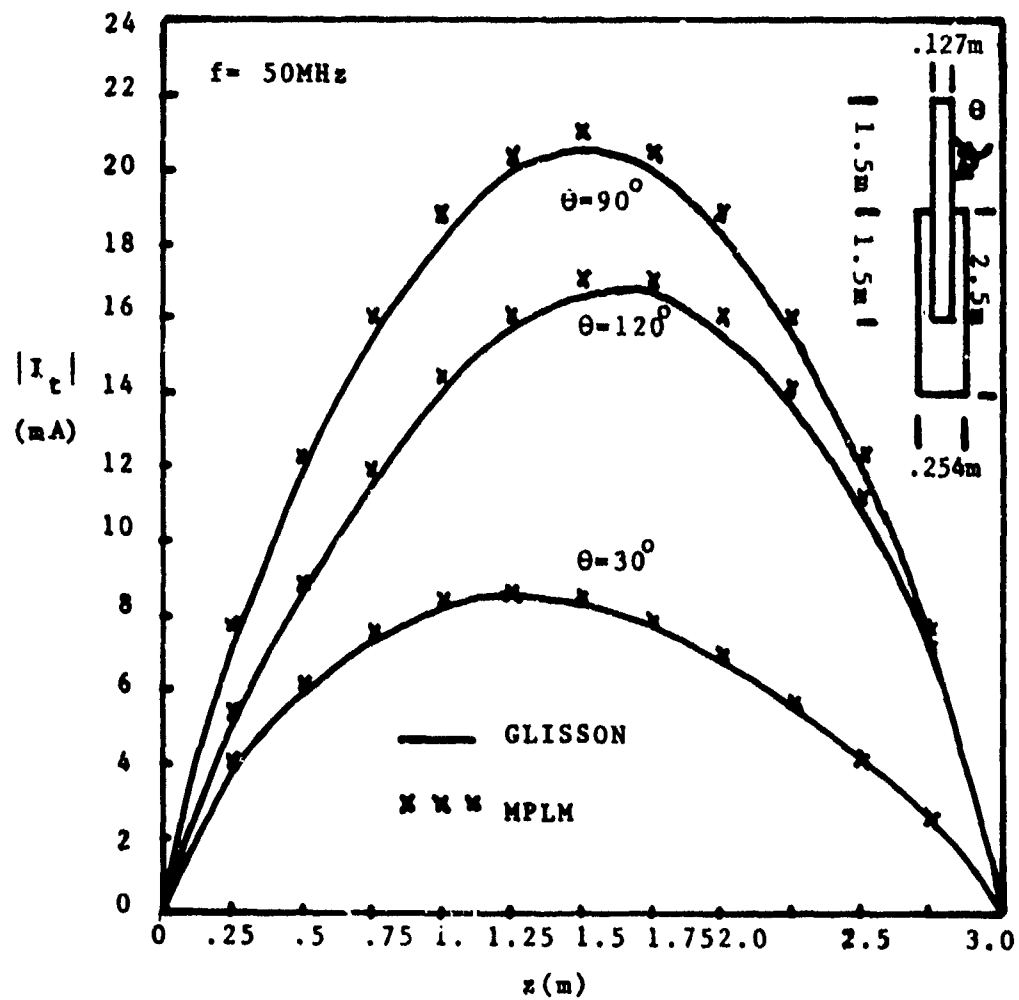


Figure 4.3b. Electric current distribution along a missile with a surrounded plume of uniform conductivity $\sigma = 0 \text{ S/m}$.

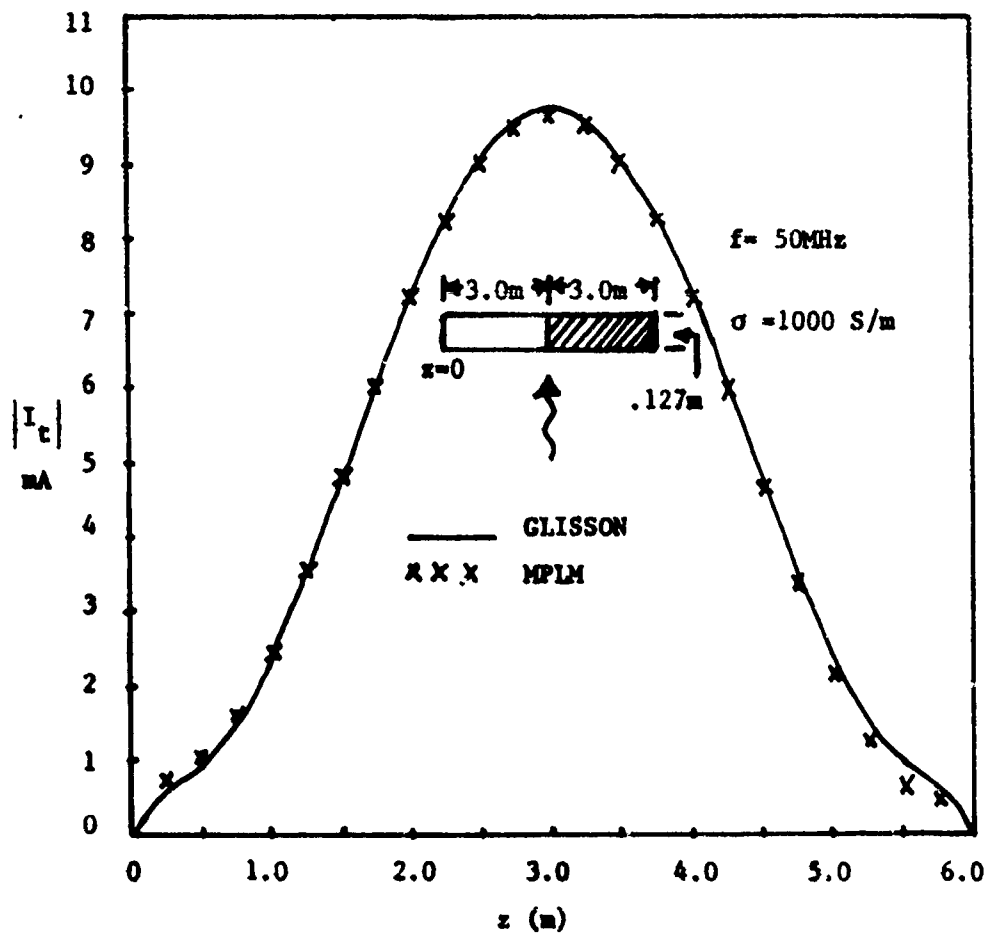


Figure 4.4a. Electric current distribution along a missile and trailing plume of uniform conductivity $\sigma = 1000$ S/m under broadside illumination.

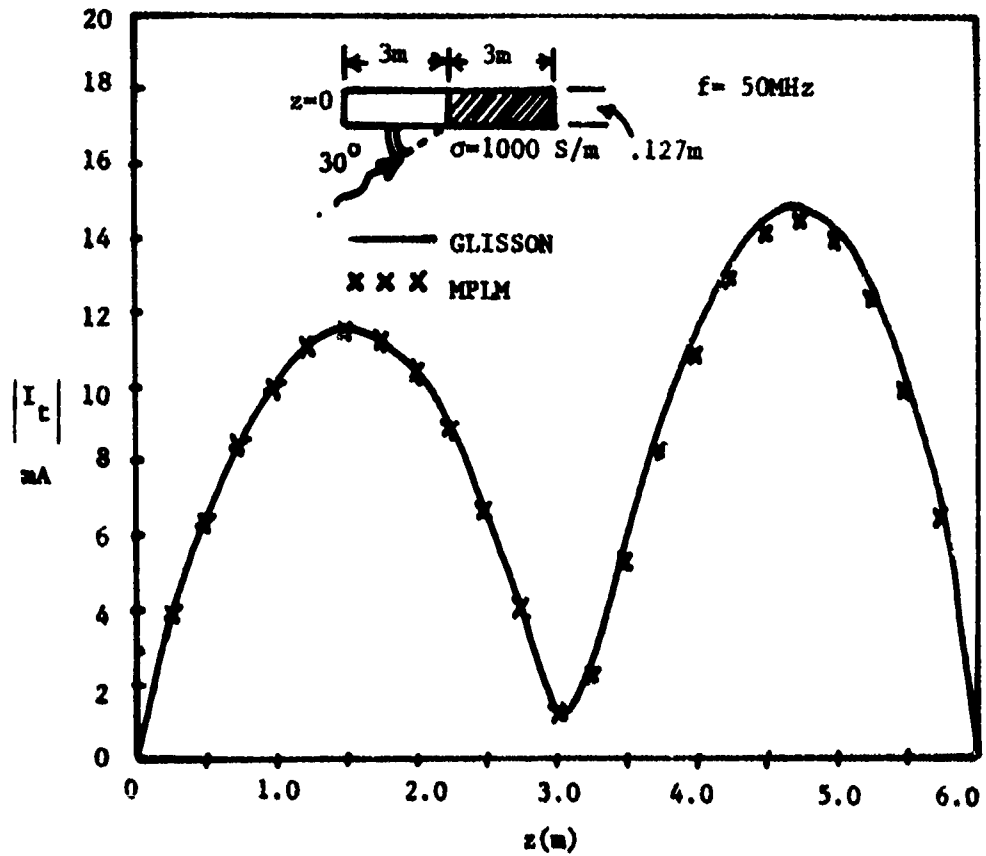


Figure 4.4b. Electric current distribution along a missile and trailing plume of uniform conductivity $\sigma = 1000$ S/m under oblique incidence.

agreement in the two approaches. The excellent agreement in the above two checks, under limiting cases, provide some confidence in the validity of the computer code MPLM. Calculations were also made for a homogeneous cylindrical plume with conductivity $\sigma = 0.2$ S/m. Fig. 4.5 depicts the resulting currents on the missile-plume combination. Also shown are the results obtained by Wu et.al. [17] for the same case. One notes a fairly good agreement in the two results. A possible explanation for the difference is the different type of treatment of the junction between the missile and the plume used here as compared to that used by Wu et.al. [17]. Further it is known that the junction modeling strongly influences the currents on the missile [17]. Whereas the procedure used here essentially averages the boundary condition on portions of the missile, plume and the missile/plume interface that are common to the junction, the approach followed by Wu et.al. [17] is to enforce only the boundary condition on the missile and let the enforced continuity of current flowing onto the remaining surfaces at the junction take care of the satisfaction of the boundary conditions on these surfaces. This latter approach is, in principle, correct; however, in a numerical procedure, a certain degree of "averaging" of the

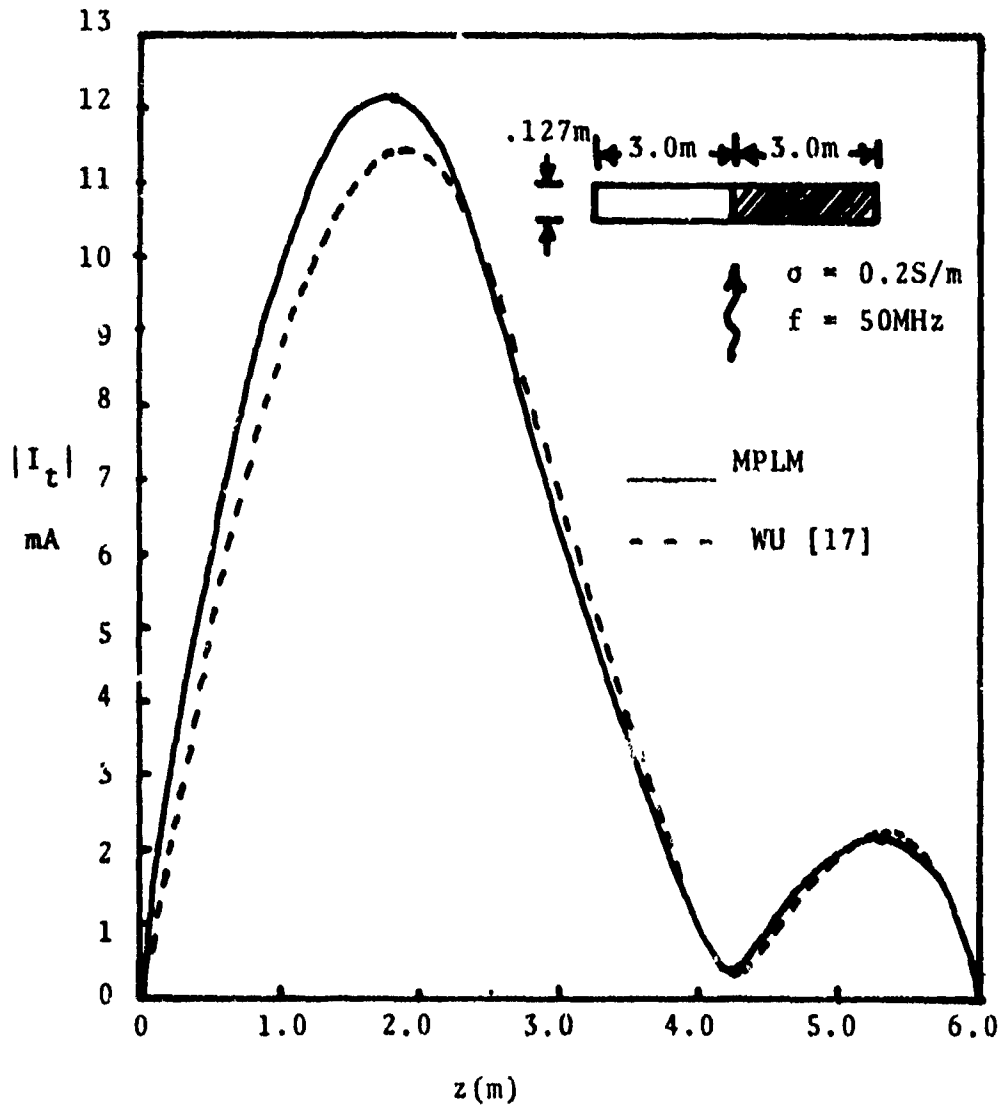


Figure 4.5. Electric current distribution along missile and trailing plume of uniform conductivity $\sigma = 0.2$ S/m under broadside illumination.

boundary conditions is desirable because a pulse representation of the current is, in a sense, a local averaging process and hence one can expect the boundary conditions to be satisfied only in an average sense as well. Based on these observations and the excellent agreement in the limiting cases shown in Figs. 4.3 and 4.4, it is concluded that the missile/plume junction treatment used here probably yields more accurate results than those obtained by the treatment adopted by Wu et.al. [17], and that the differences in the results seen in Fig. 4.5 are due to the different ways in which the junction is treated.

For the actual inhomogeneous missile plume, the plume inhomogeneity is predicted using the LAPP computer code. This code simultaneously models thermo-chemical reactions and rocket aerodynamics to establish the electrical properties, viz., permittivity and conductivity, inside the plume region. The plume conductivity calculations we have used here model the plume of a static (zero velocity) Chapparral missile at a 5000 ft. (1524m) altitude. The calculations show that the electrical permittivity does not change much from the free-space value, but that the conductivity is strongly inhomogeneous both radially and axially. A detailed discussion of the LAPP code is given in [18]. Conductivity values

predicted by the LAPP code result in constant conductivity profiles shown in Fig. 4.6. Based on this accurate profile, a judicious choice of layer boundaries was made and the assumed constant value of the conductivity between the layer boundaries was obtained by averaging the conductivity between two contours. Fig. 4.7 shows the resulting layered approximation to the inhomogeneous plume. We shall be adopting two models of the plume, the long and **short** plume models. Such a choice is made for two reasons. It has been found [17] that the effect of the plume on the currents on the missile is negligible when the conductivity in the region around the nozzle of the missile is small. Further, the values of the conductivity in the plume, as predicted by the LAPP code, is known to be less accurate around the nozzle region as compared to the values predicted in the regions away from the nozzle. The extent of the regions of the short and long plume models are shown in Fig. 4.7. One notes that the region around the nozzle has a low conductivity value in the long plume model and a higher conductivity value in the short plume model. Figs. 4.8 through 4.12 show the computed currents on the missile and plume for various angles on incidence and frequencies. Cost of computations has limited a more detailed study of the short plume model. We note from these figures that the currents on the missile are not much affected under the long

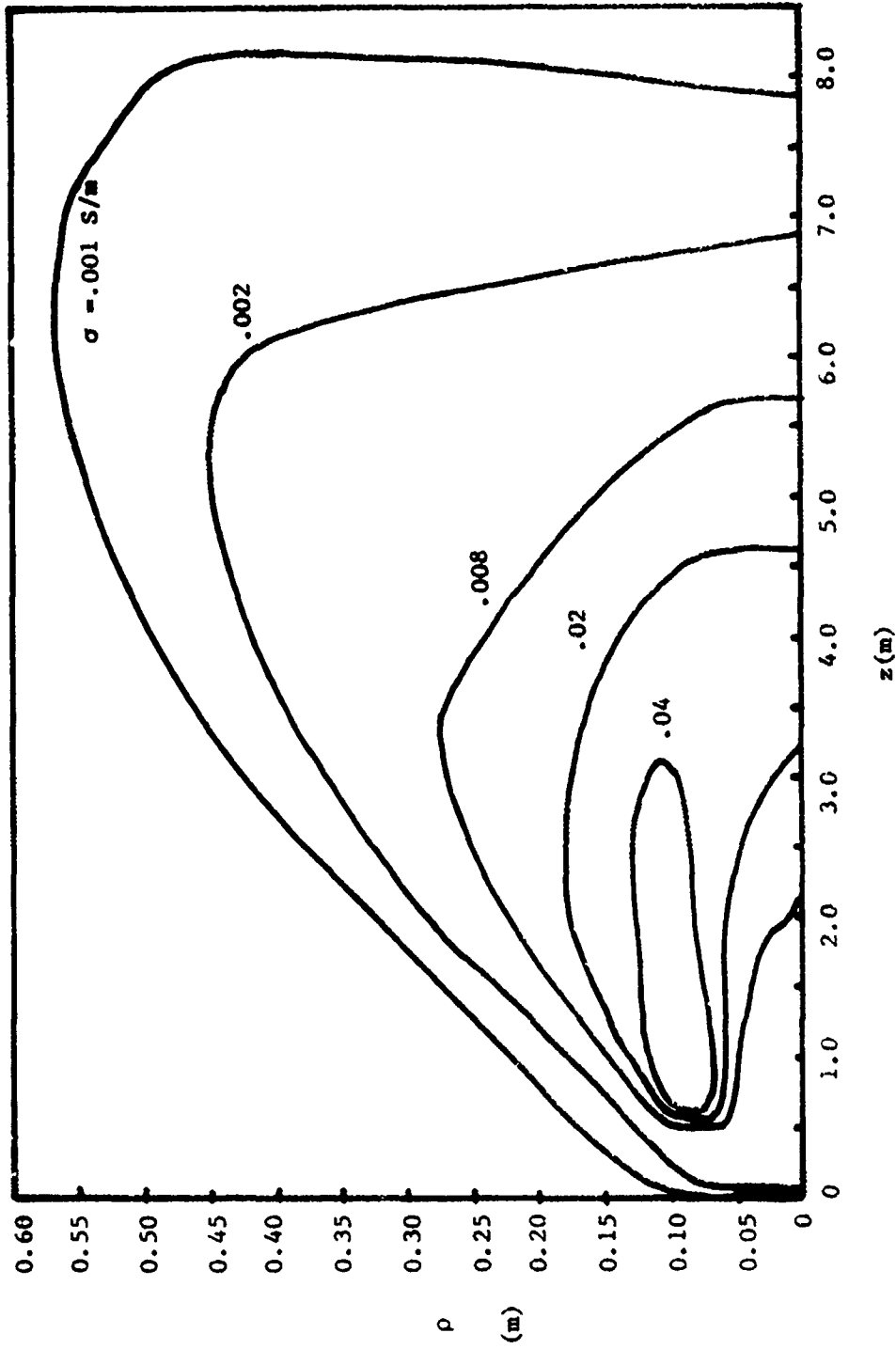


Figure 4.6. Constant conductivity contours of a Chaparral missile plume.

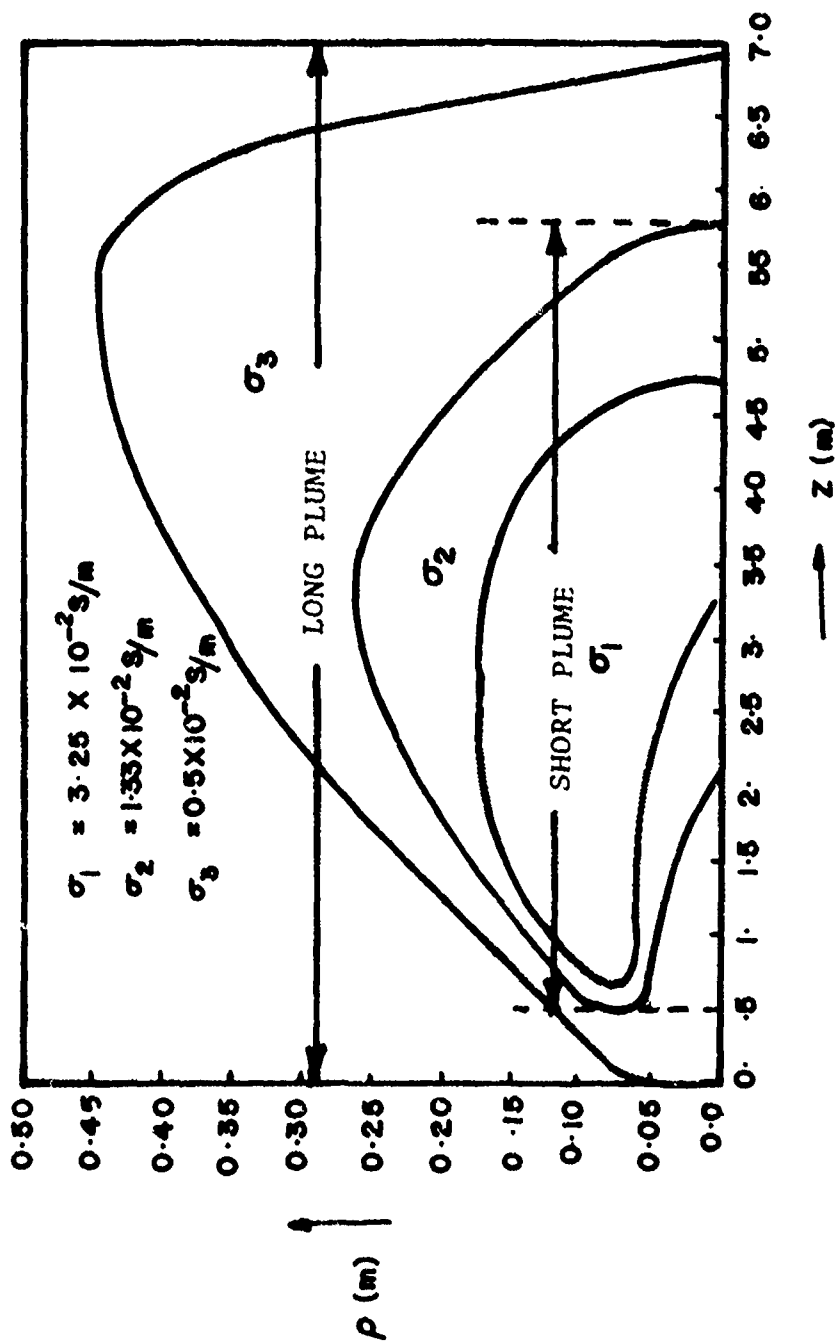


Figure 4.7. Layered approximation to the plume of the Chaparral missile.

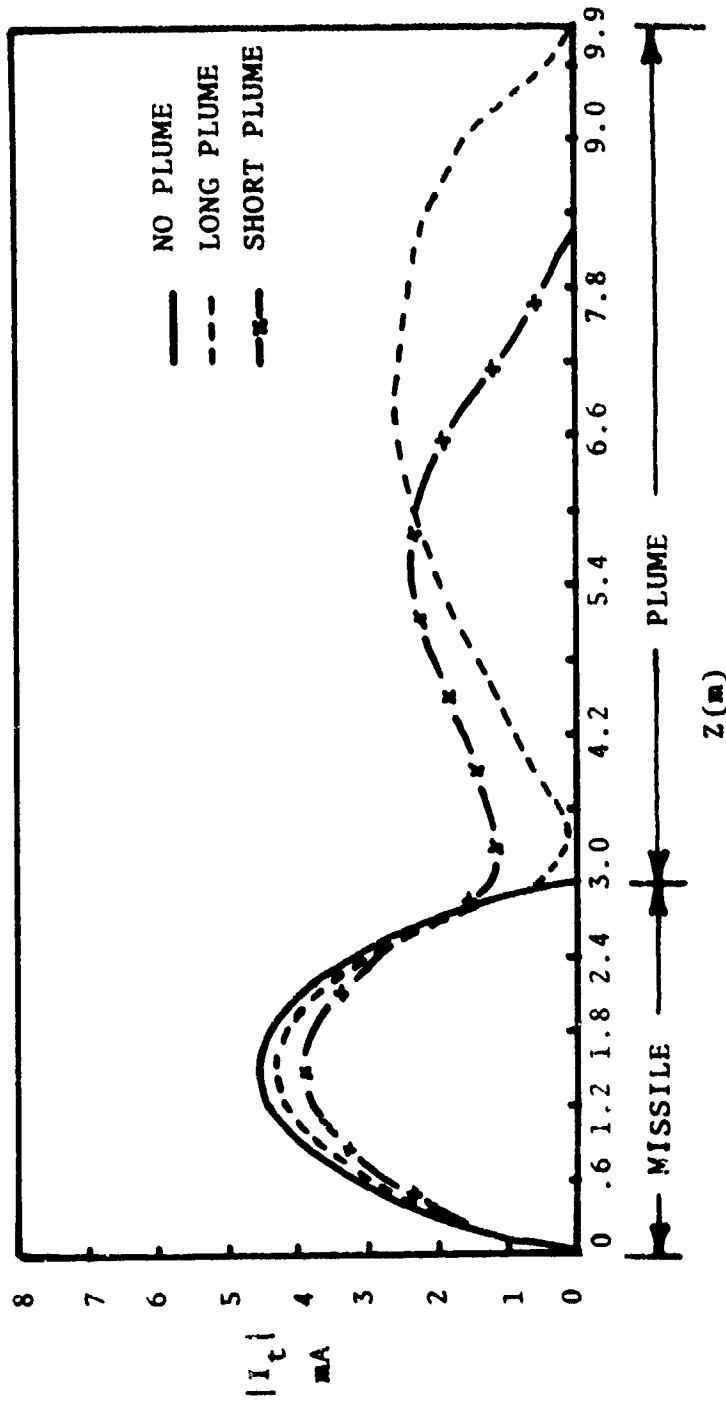


Figure 4.8a. Electric current distribution along a Chaparral missile and trailing plume, $f = 30$ MHz, $\theta^{inc} = 30^\circ$.

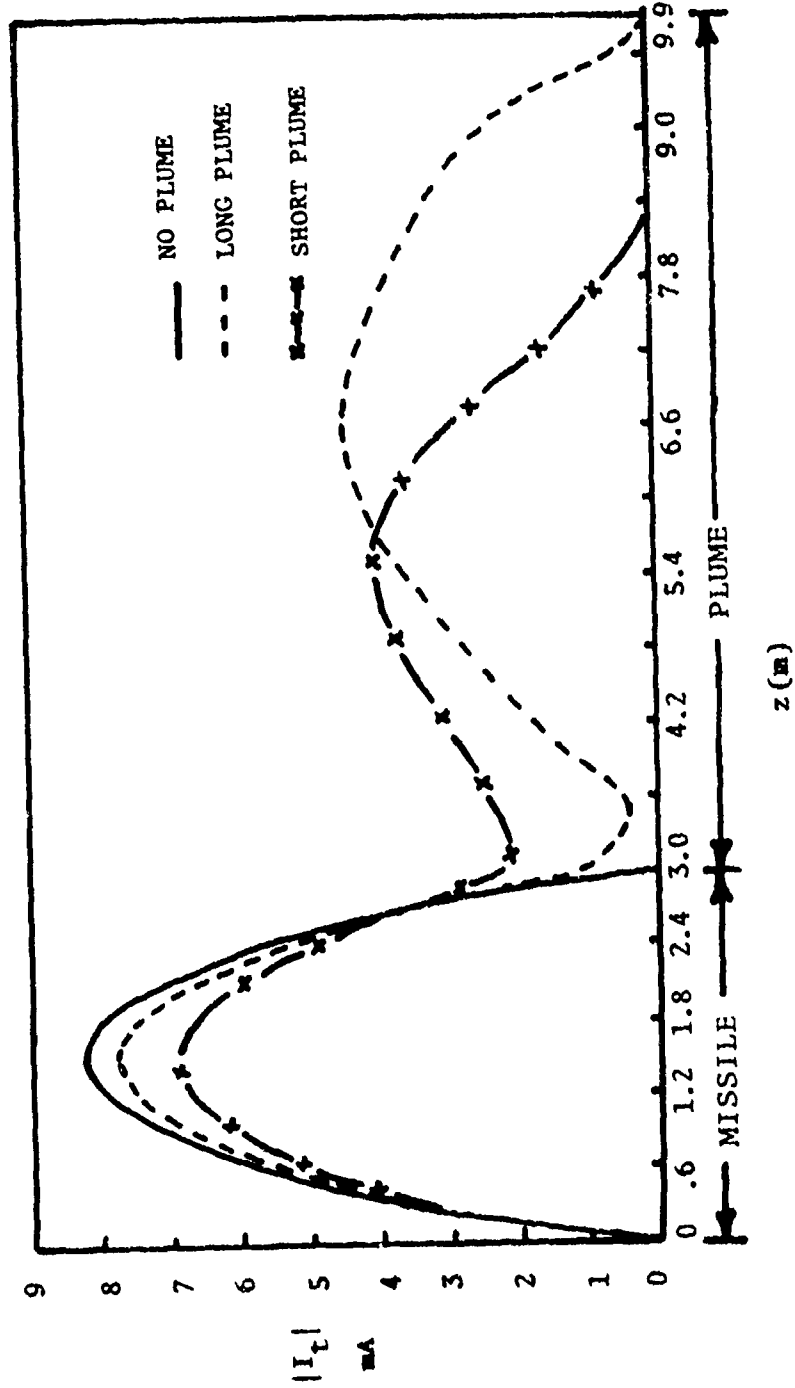


Figure 4.8b. Electric current distribution along a Chaparral missile and trailing plume. $f = 30$ MHz, $\theta^{inc} = 60^\circ$.

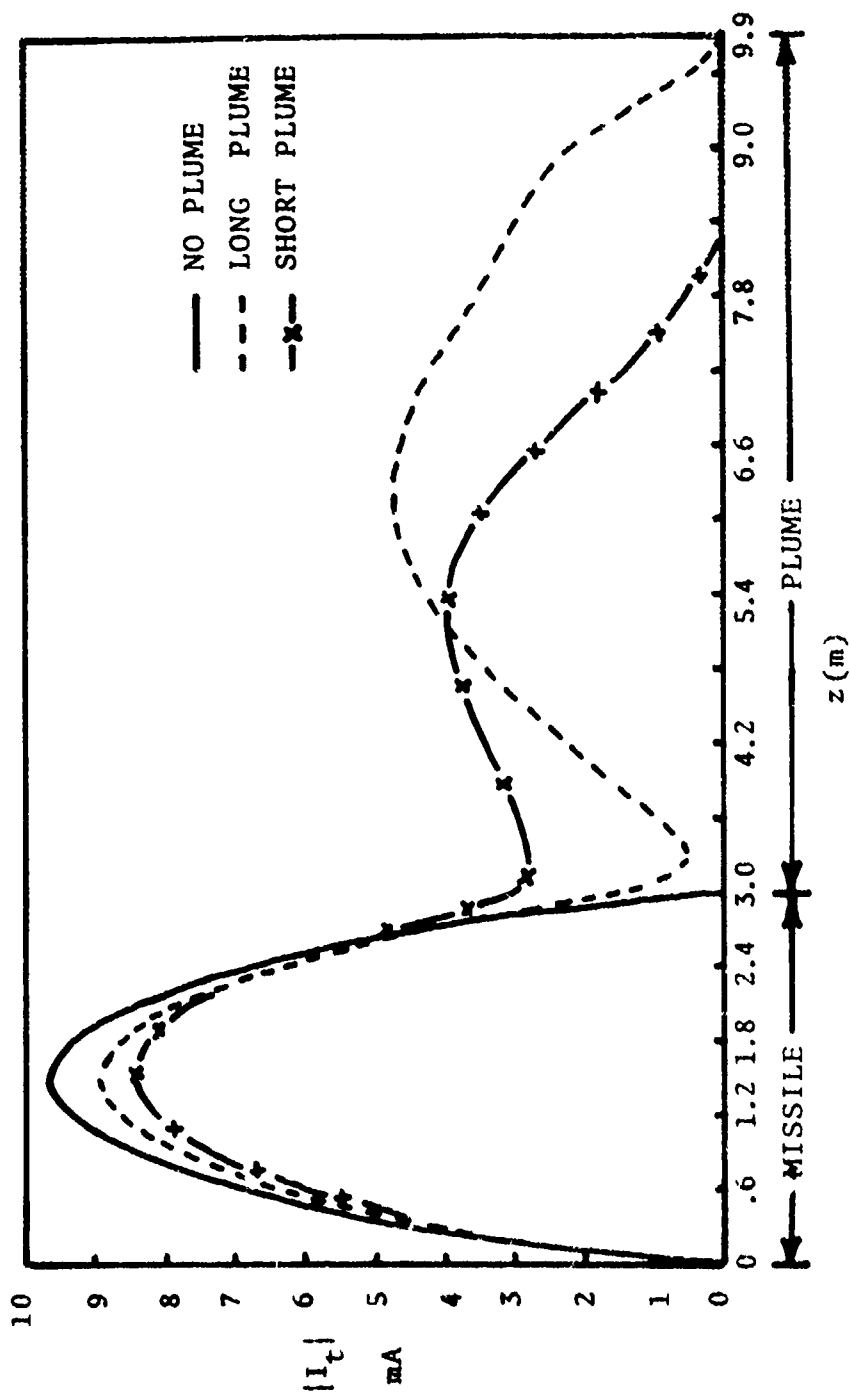


Figure 4.8c. Electric current distribution along a Chaparral missile and trailing plume, $f = 30$ MHz, $\theta_{inc} = 90^\circ$.

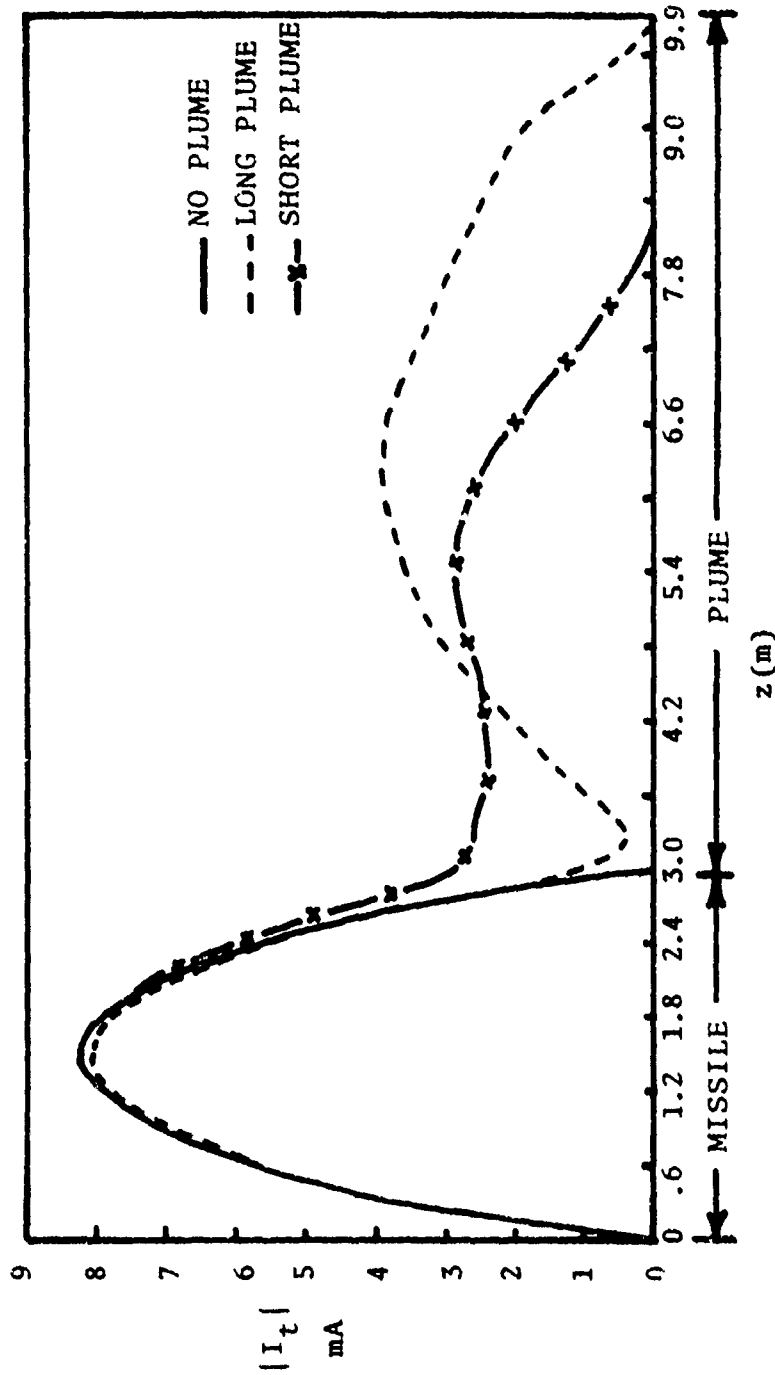


Figure 4.8d. Electric current distribution along a Chaparral missile and trailing plume, $f = 30$ MHz, $\theta^{inc} = 120^\circ$.

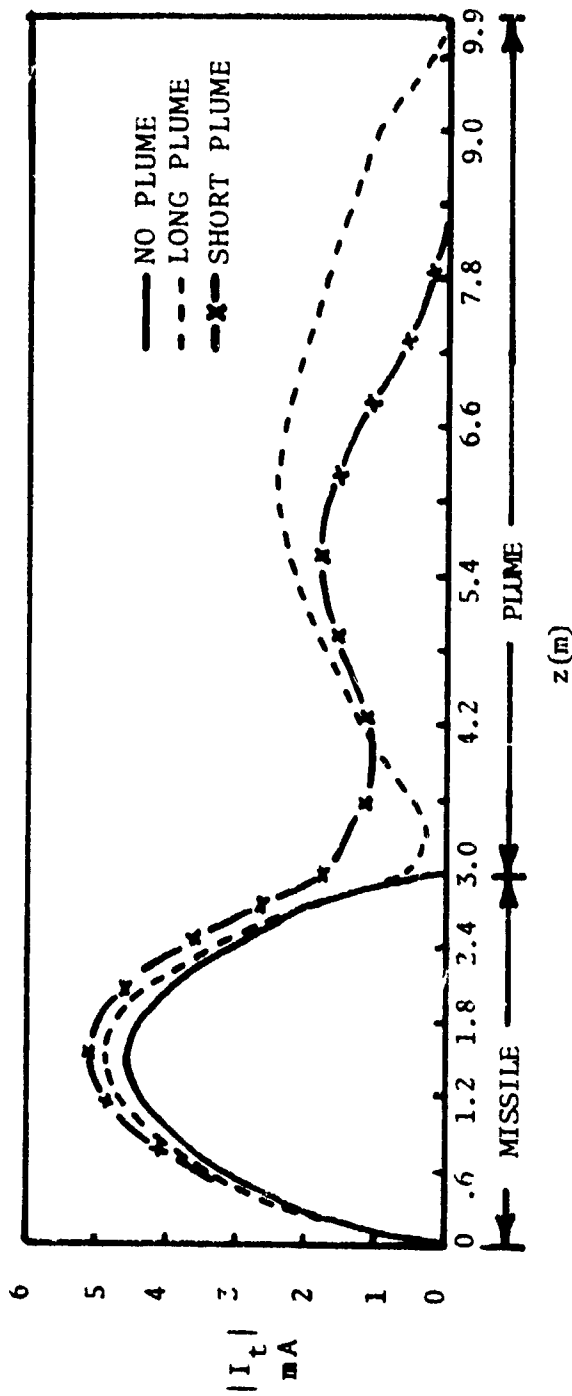


Figure 4.8a. Electric current distribution along a Chaparral missile and trailing plume, $f = 30$ MHz, $\theta_{inc} = 150^\circ$.

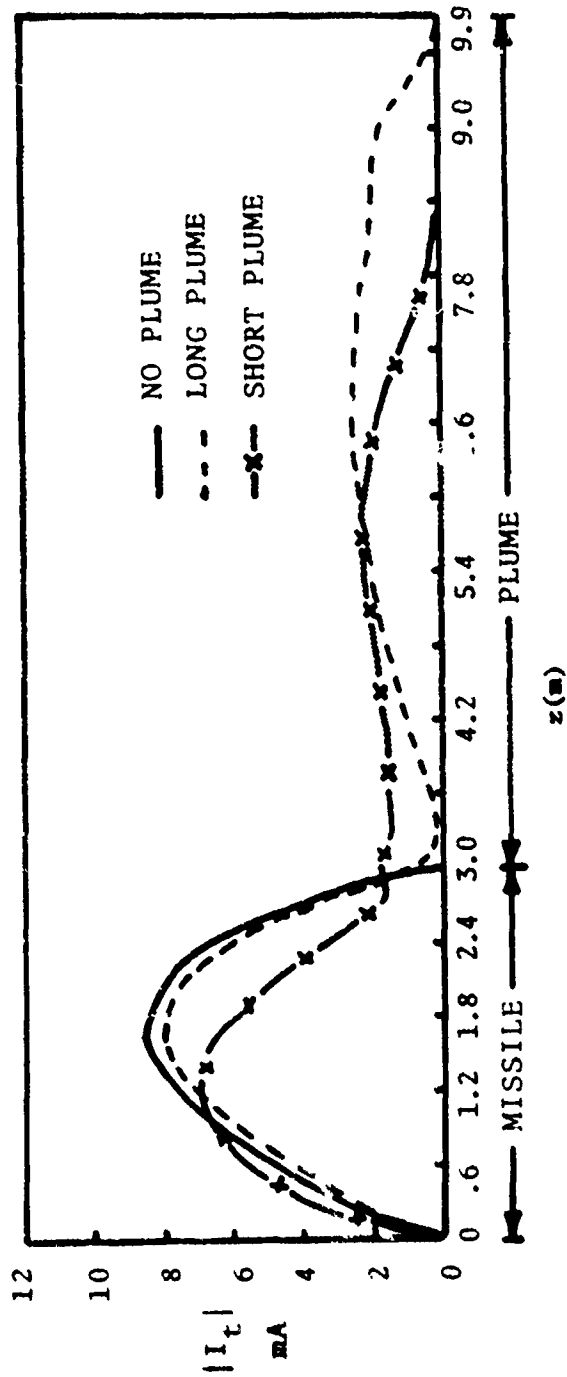


Figure 4.9a. Electric current distribution along a Chaparral missile and trailing plume, $f = 50$ MHz, $\theta_{inc} = 30^\circ$.

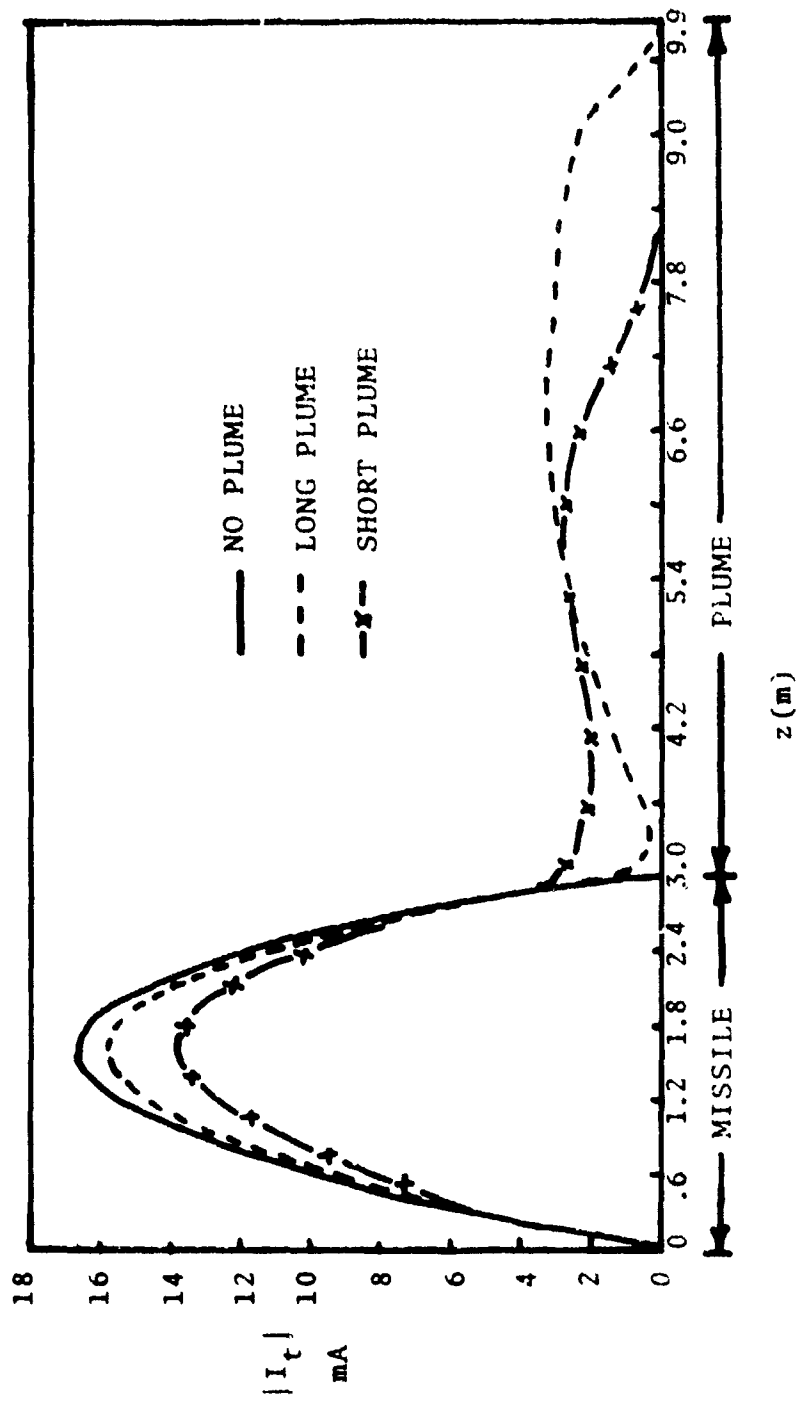


Figure 4.9b. Electric current distribution along a Chaparral missile and trailing plume, $f = 50$ MHz, $\theta^{inc} = 60^\circ$.

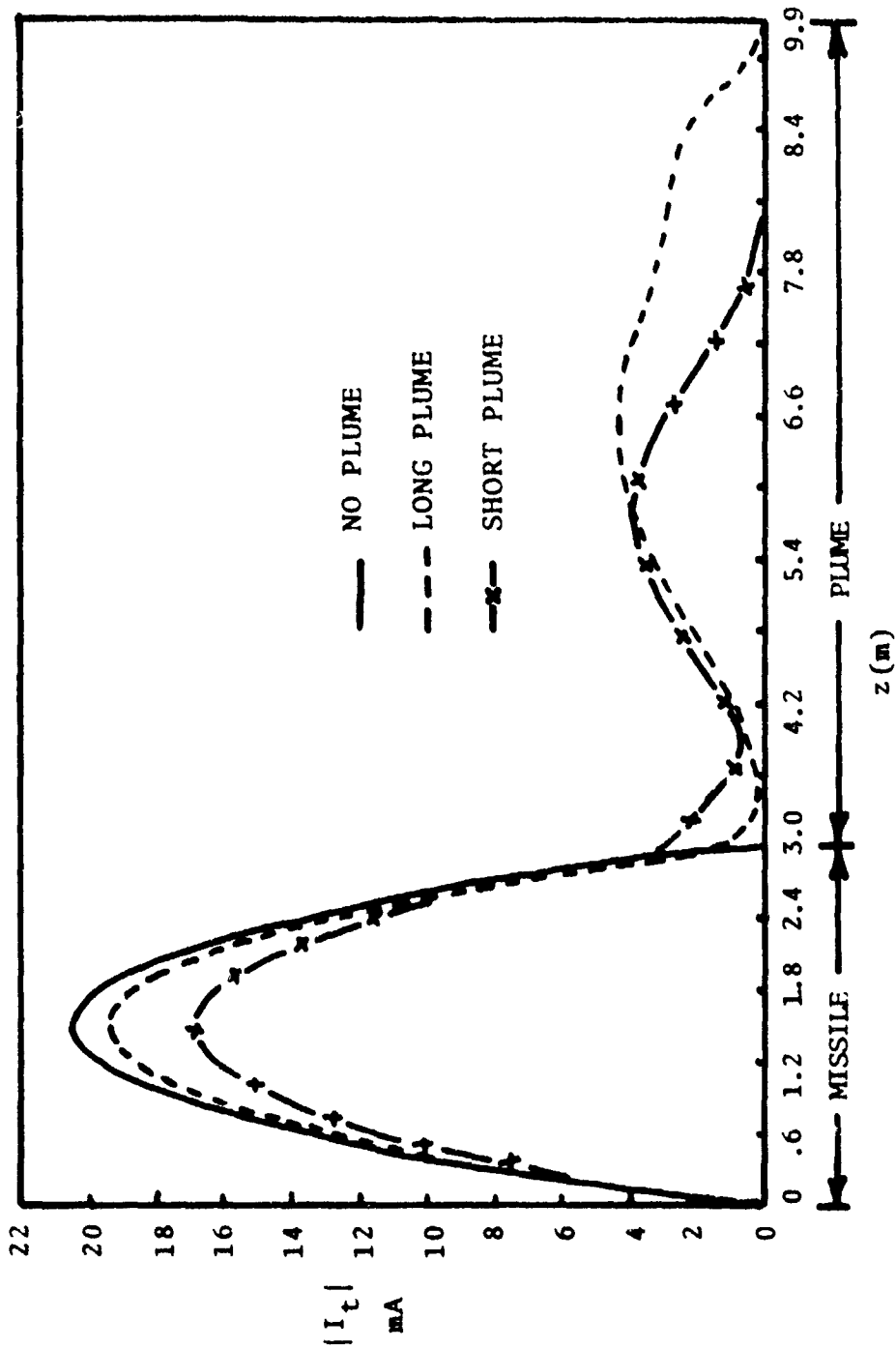


Figure 4.9c. Electric current distribution along a Chaparral missile and trailing plume, $f = 50$ MHz, $\theta_{inc} = 90^\circ$.

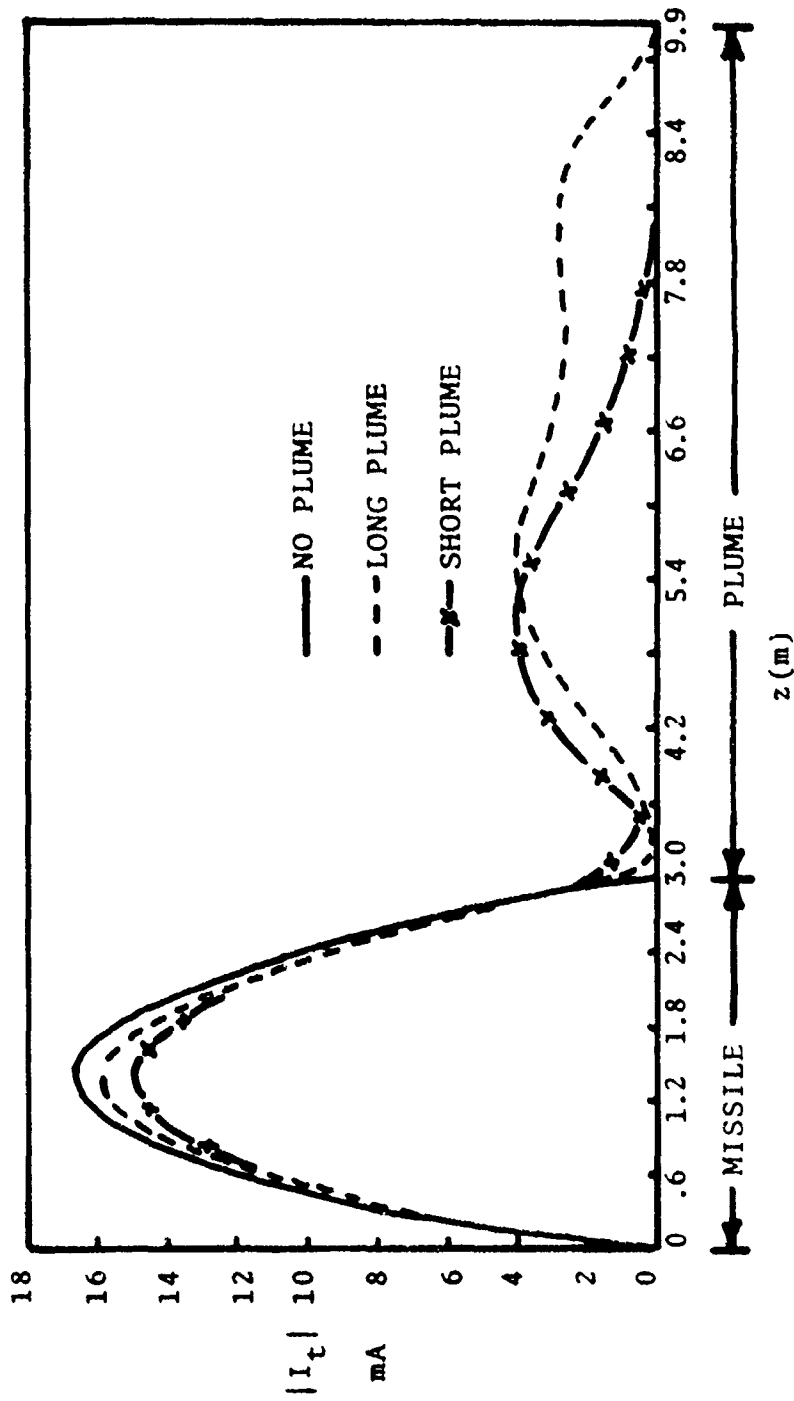


Figure 4.9d. Electric current distribution along a Chaparral missile and trailing plume, $f = 50 \text{ MHz}$, $\theta_{inc} = 120^\circ$.

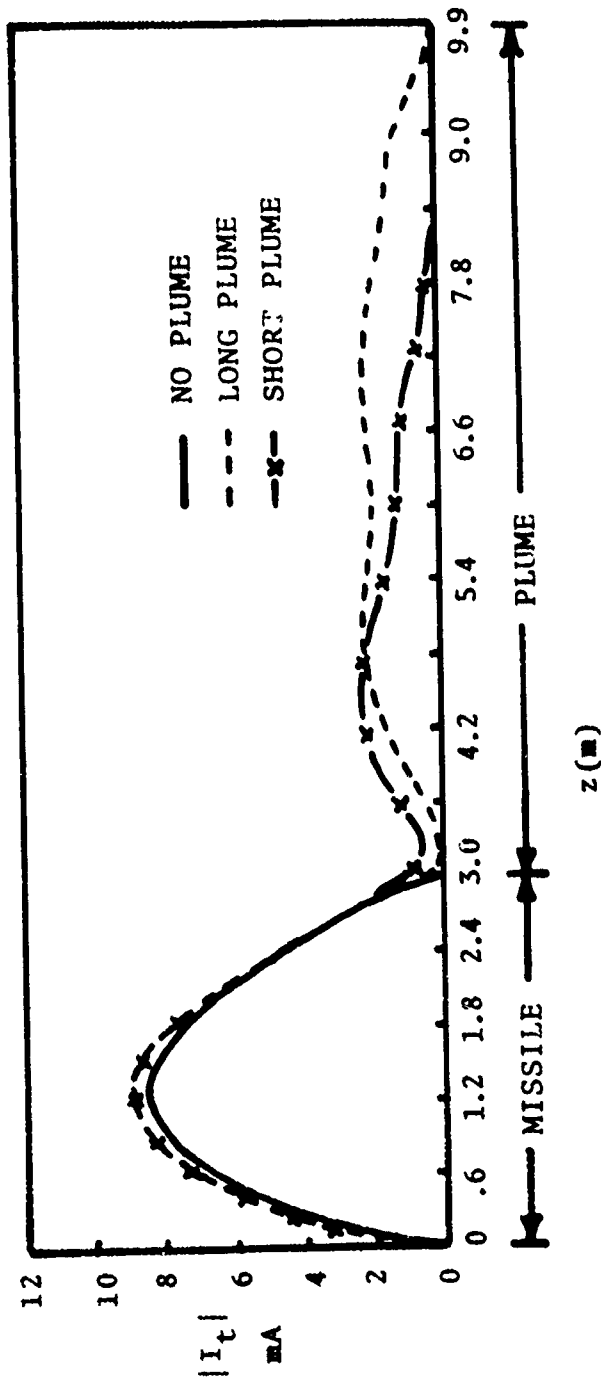


Figure 4.9e. Electric current distribution along a Chaparral missile and trailing plume, $f = 50$ MHz, $\theta^{inc} = 150^\circ$.

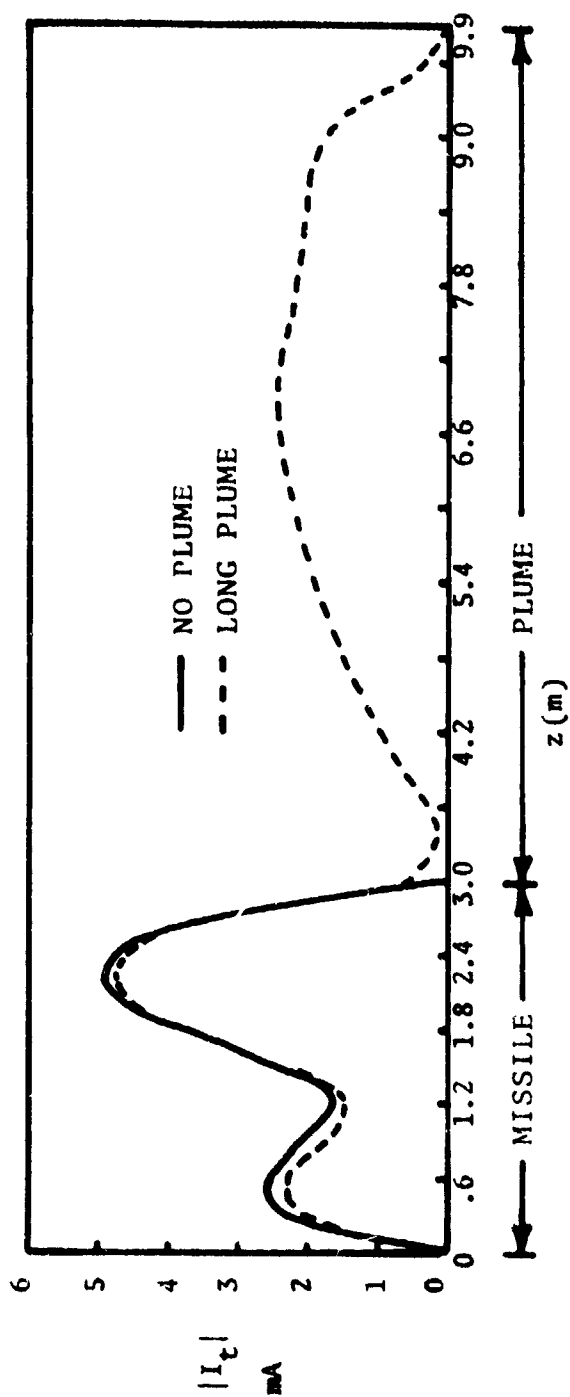


Figure 4.10a. Electric current distribution along a Chaparral missile and trailing plume, $f = 70 \text{ MHz}$, $\theta_{inc} = 30^\circ$.

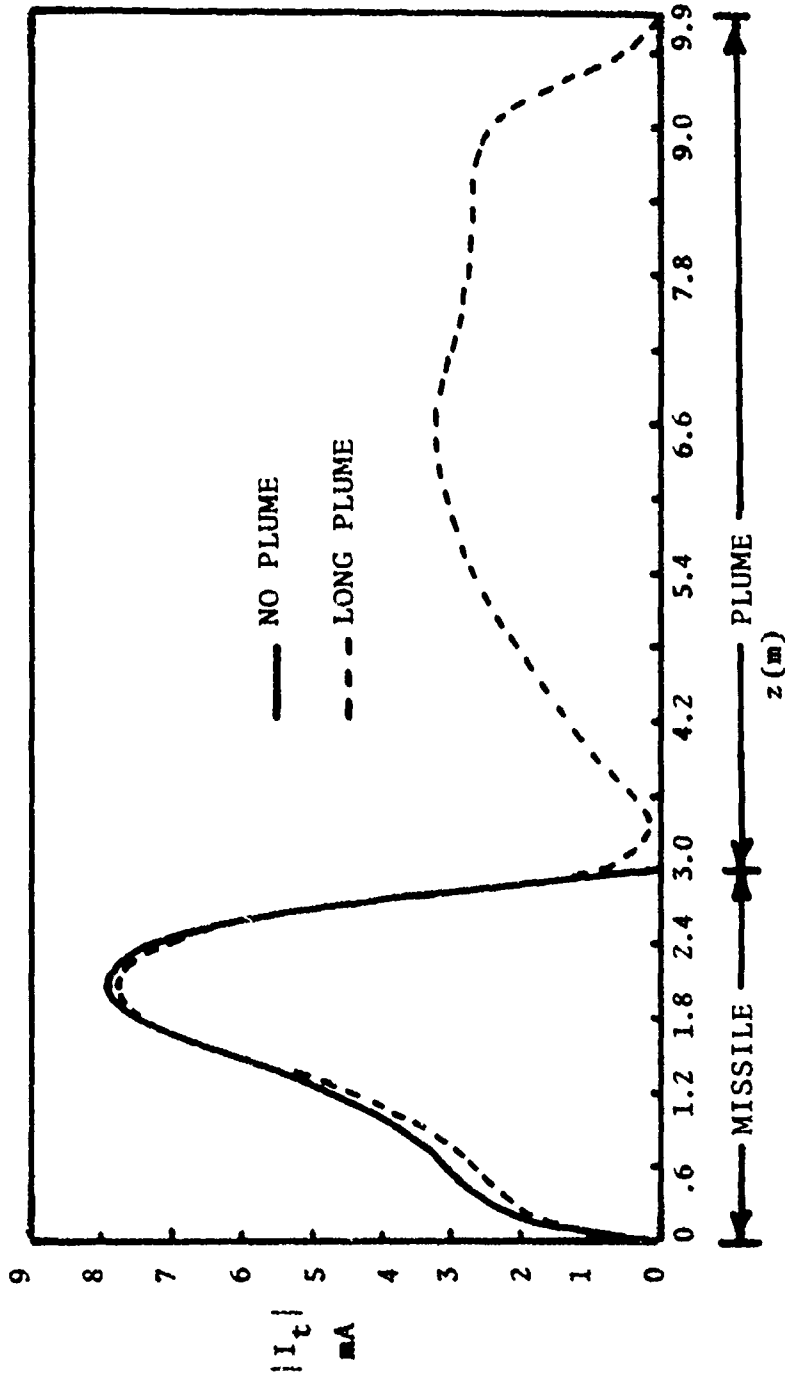


Figure 4.10b. Electric current distribution along a Chaparral missile and trailing plume, $f = 70$ MHz, $\theta^{inc} = 60^\circ$.

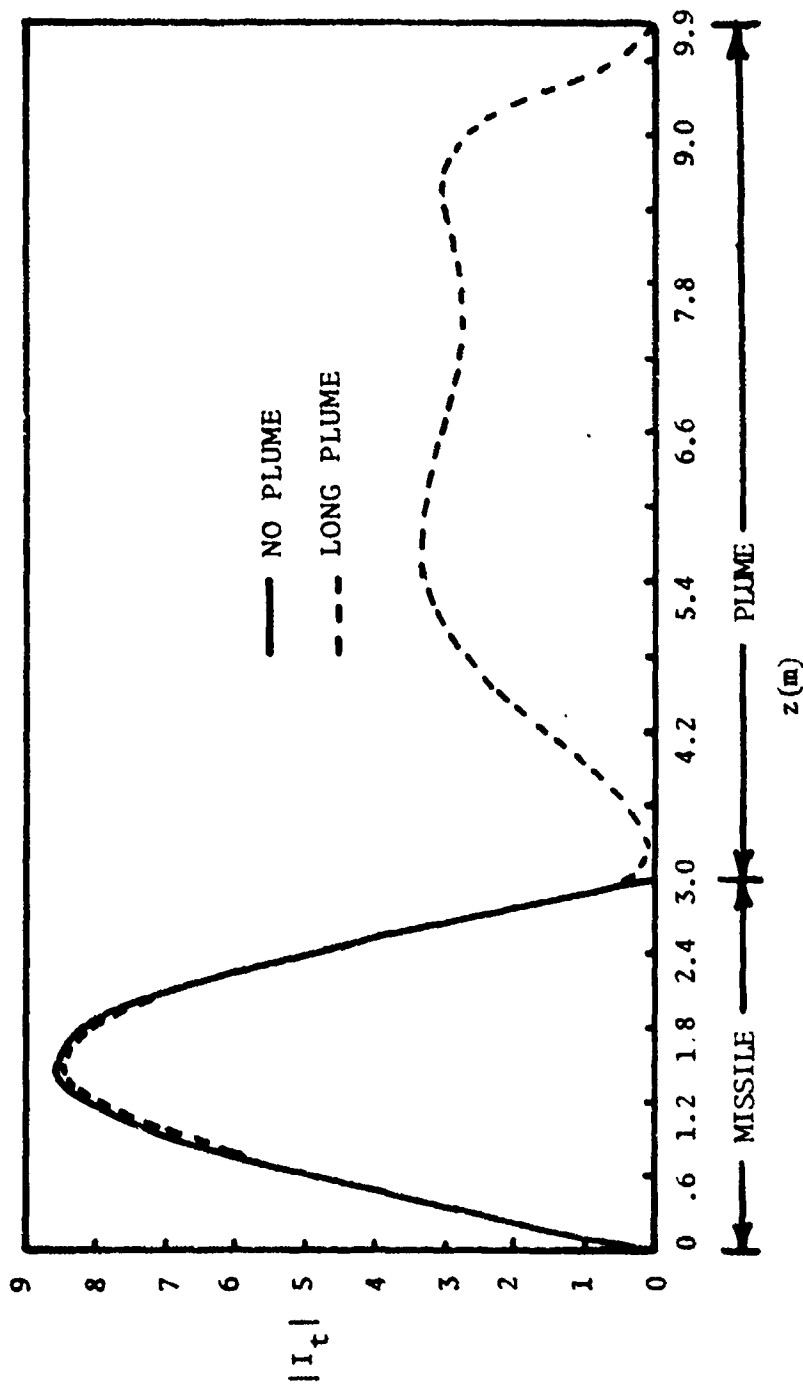


Figure 4.10c. Electric current distribution along a Chaparral missile and trailing plume, $f = 70$ MHz, $\theta_{inc} = 90^\circ$.

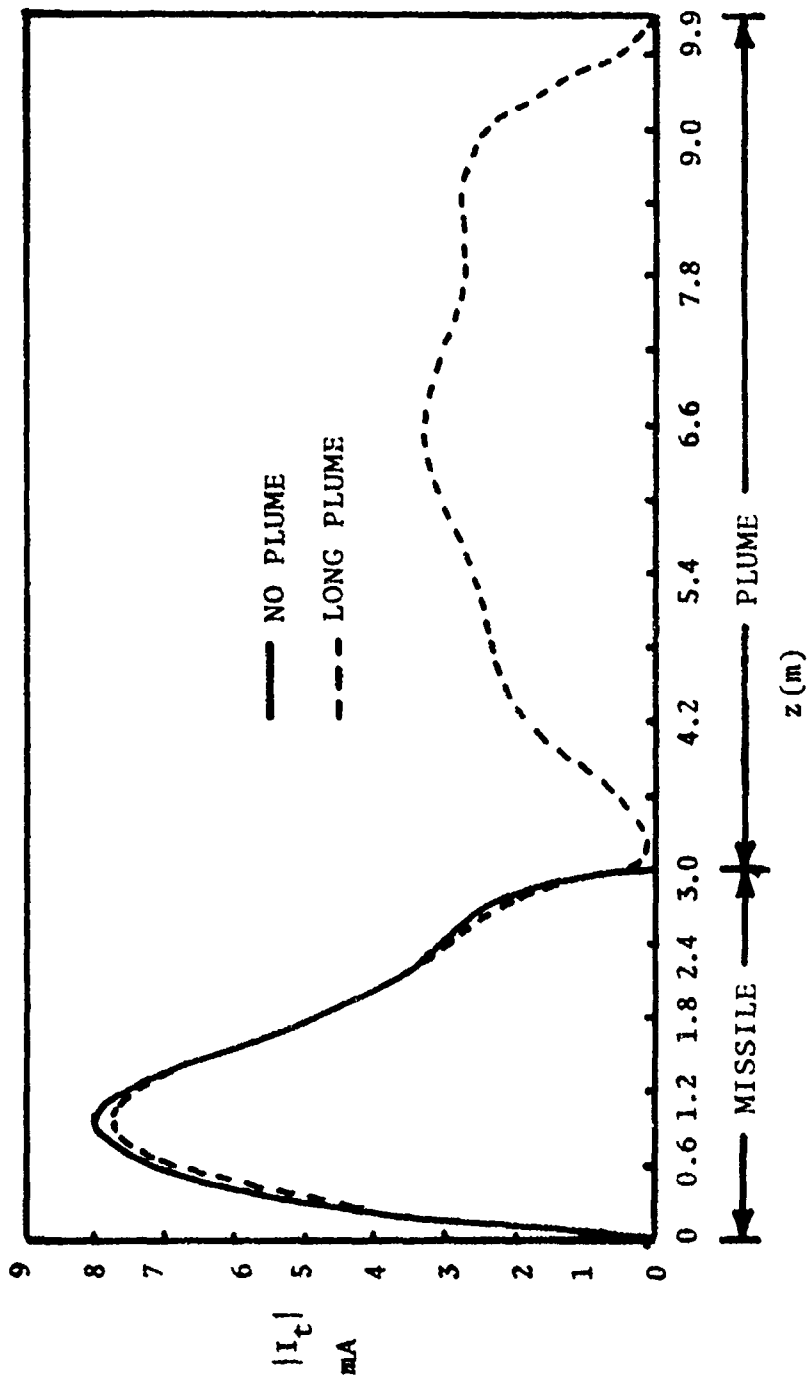


Figure 4.10d. Electric current distribution along a Chaparral missile and trailing plume, $f = 70$ MHz, $\theta^{inc} = 120^\circ$.

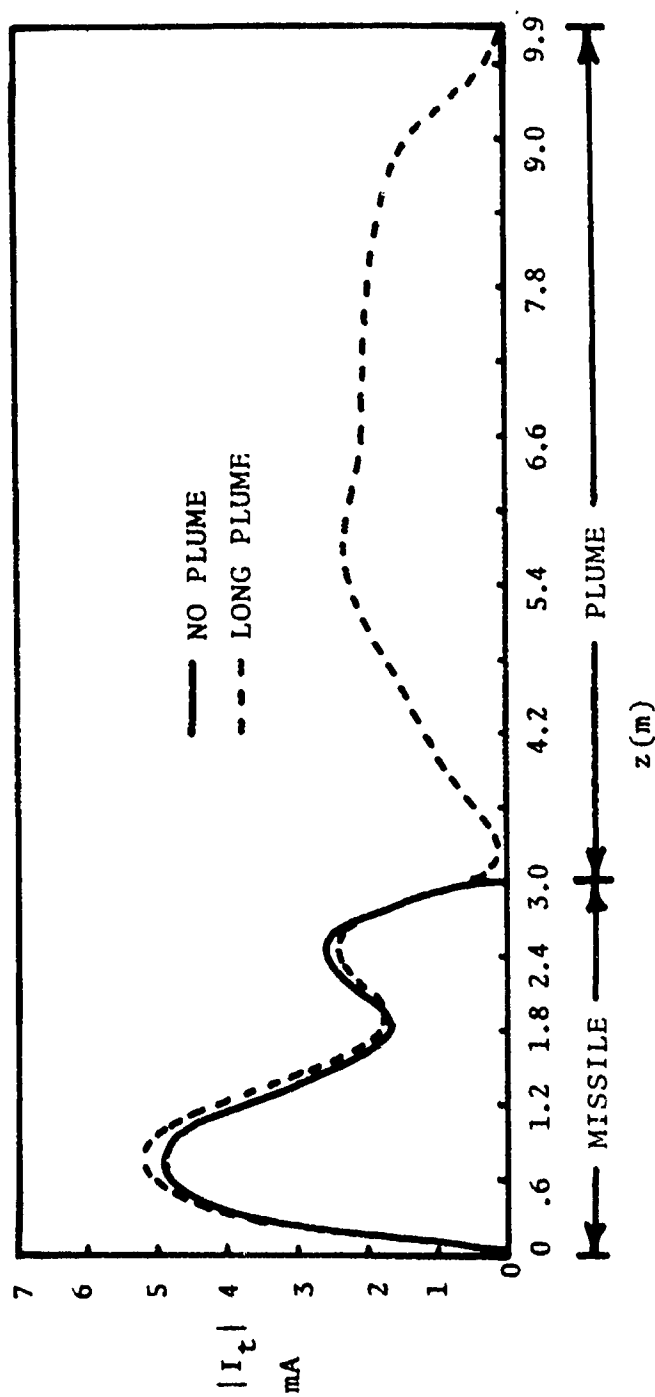


Figure 4.10e. Electric current distribution along a Chaparral missile and trailing plume, $f = 70$ MHz, $\theta_{inc} = 150^\circ$.

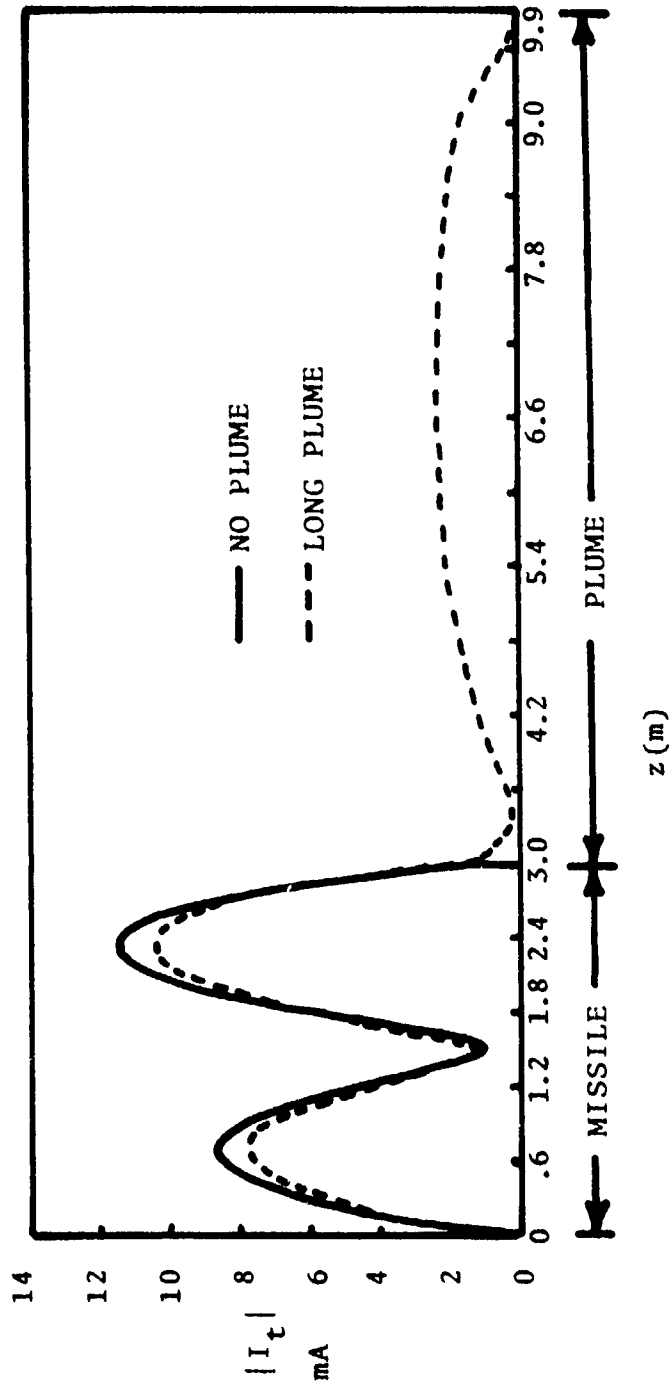


Figure 4.11a. Electric current distribution along a Chaparral missile and trailing plume, $f = 90$ MHz, $\theta^{inc} = 30^\circ$.

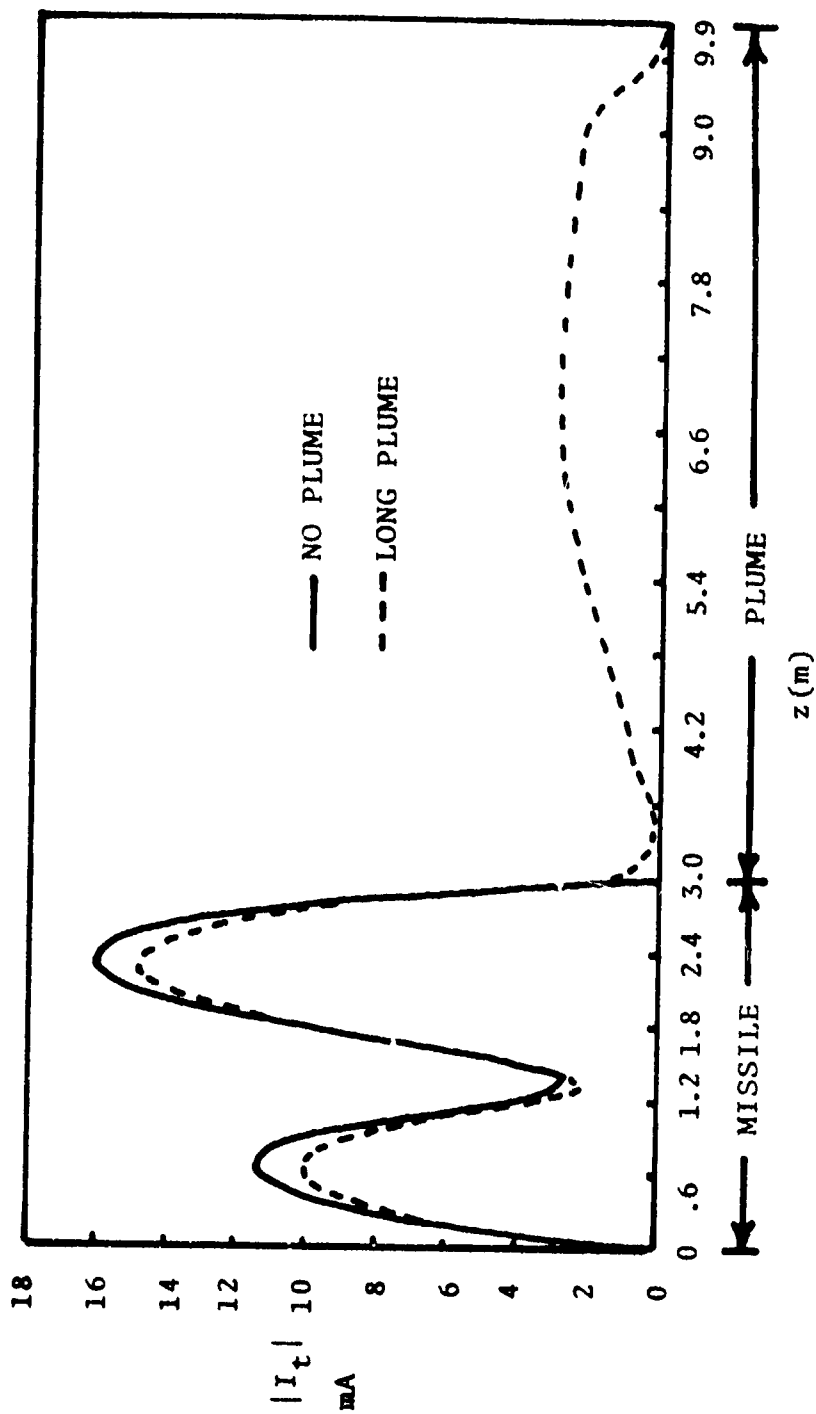


Figure 4.11b. Electric current distribution along a Chaparral missile and trailing plume, $f = 90$ MHz, $\theta_{inc} = 60^\circ$.

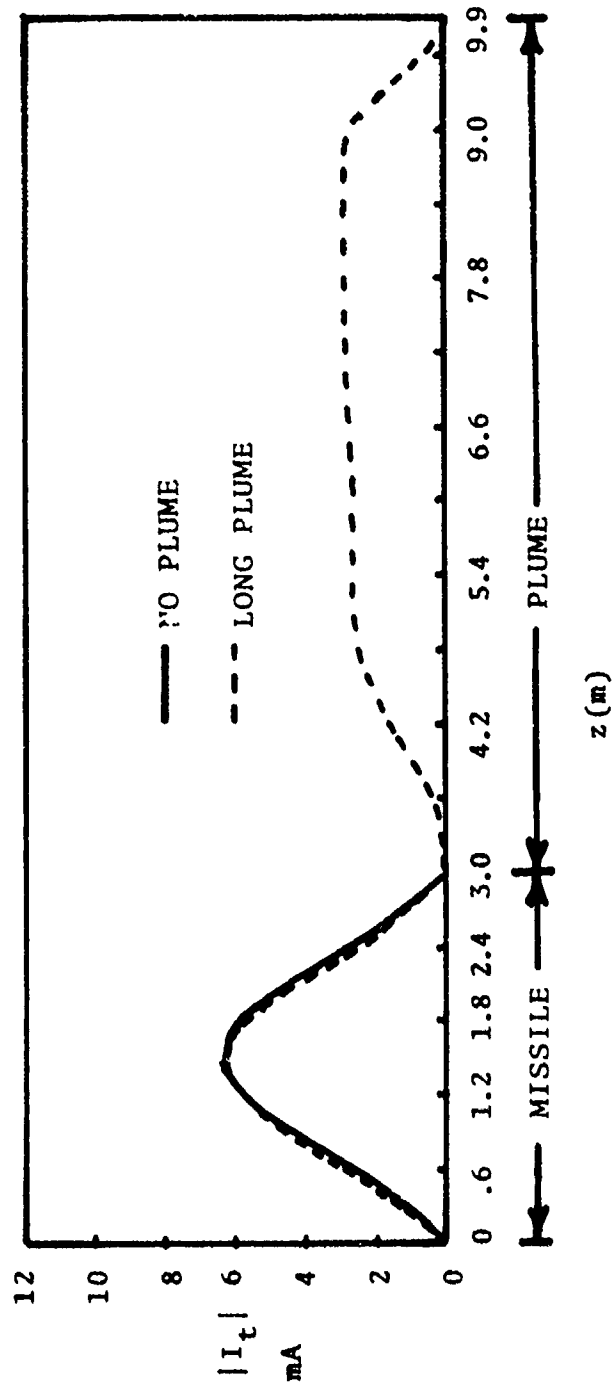


Figure 4.11c. Electric current distribution along a Chaparral missile and trailing plume, $f = 90$ MHz, $\theta_{inc} = 90^\circ$.

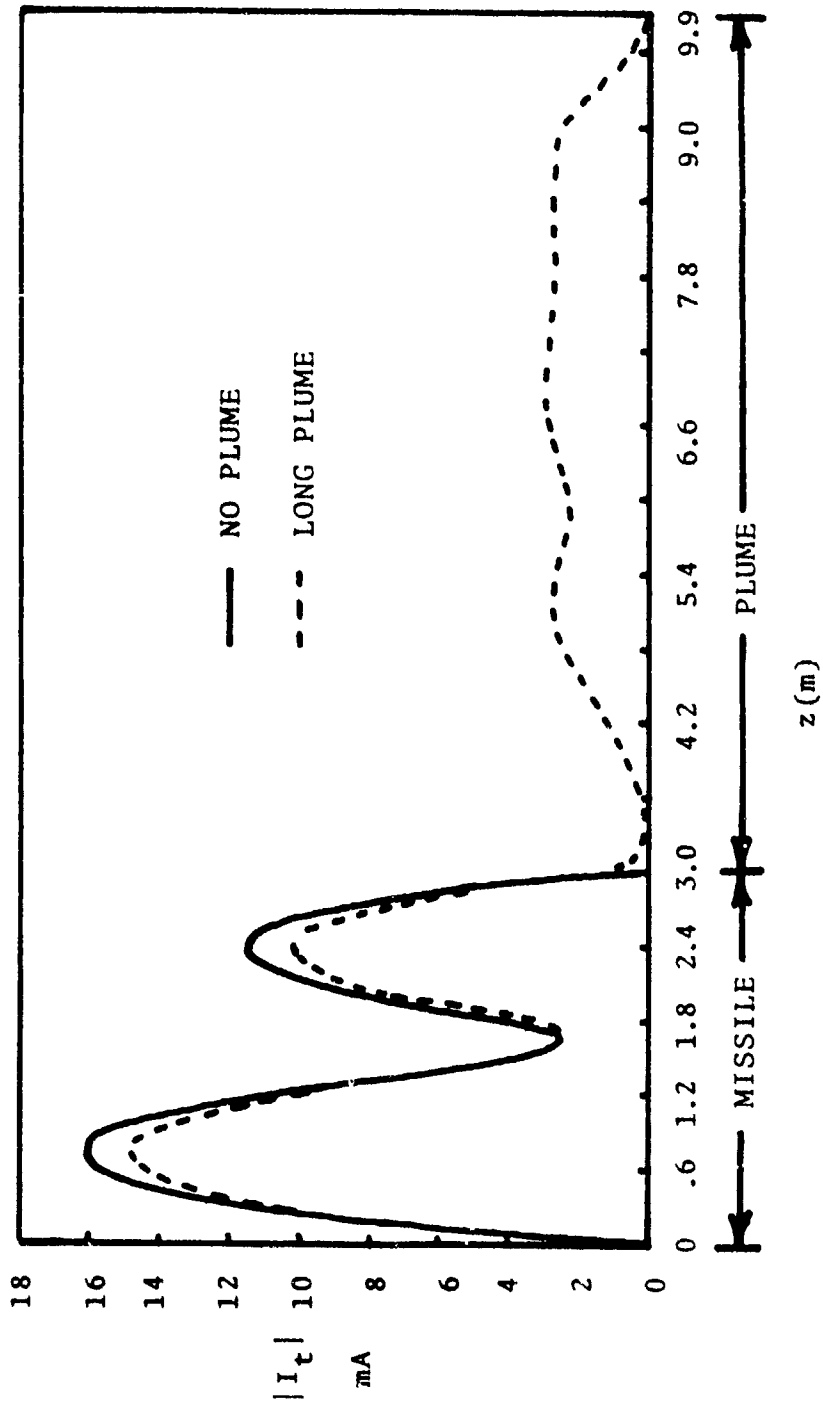


Figure 4.11d. Electric current distribution along a Chaparral missile and trailing plume, $f = 90$ MHz, $\theta^{inc} = 120^\circ$.

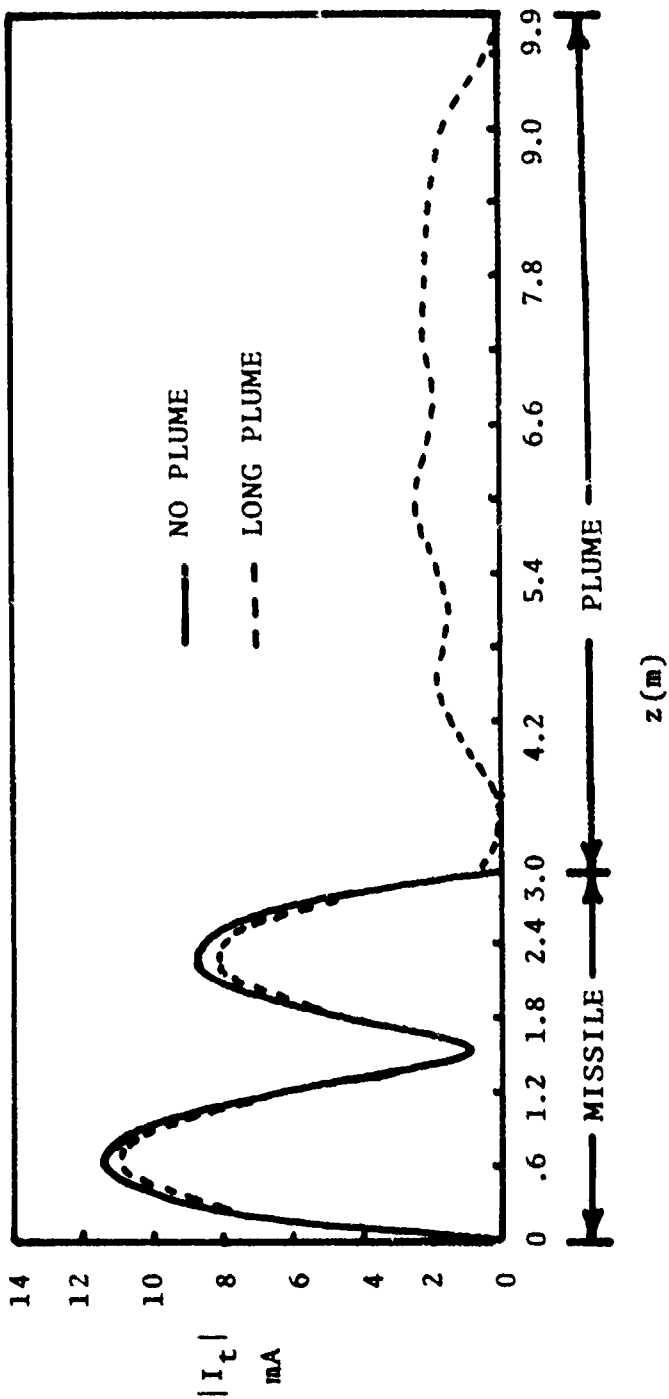


Figure 4.11e. Electric current distribution along a Chaparral missile and trailing plume, $f = 90 \text{ MHz}$, $\theta_{inc} = 150^\circ$.

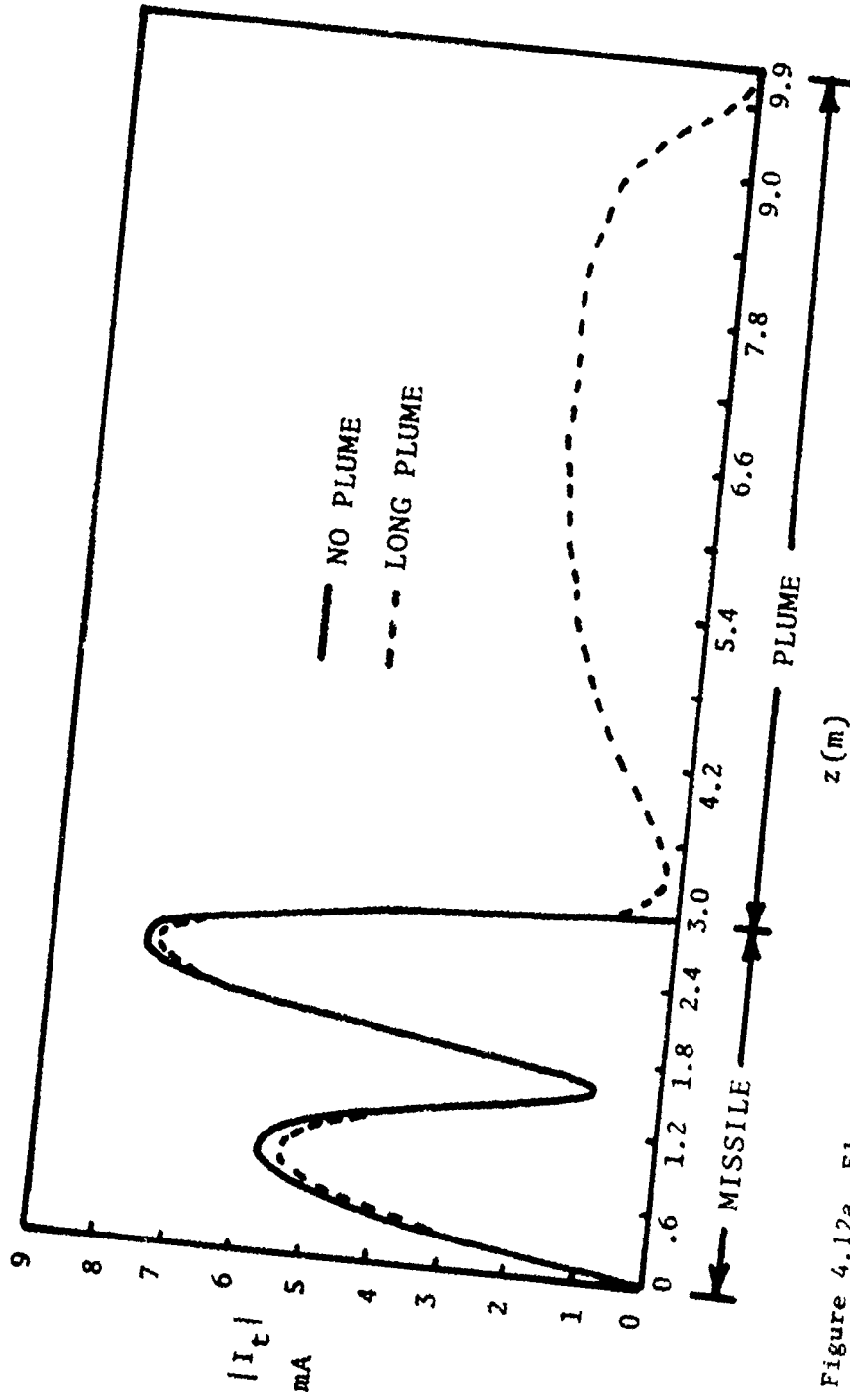


Figure 4.12a. Electric current distribution along a Chaparral missile and trailing plume, $f = 100$ MHz, $\theta_{inc} = 30^\circ$.

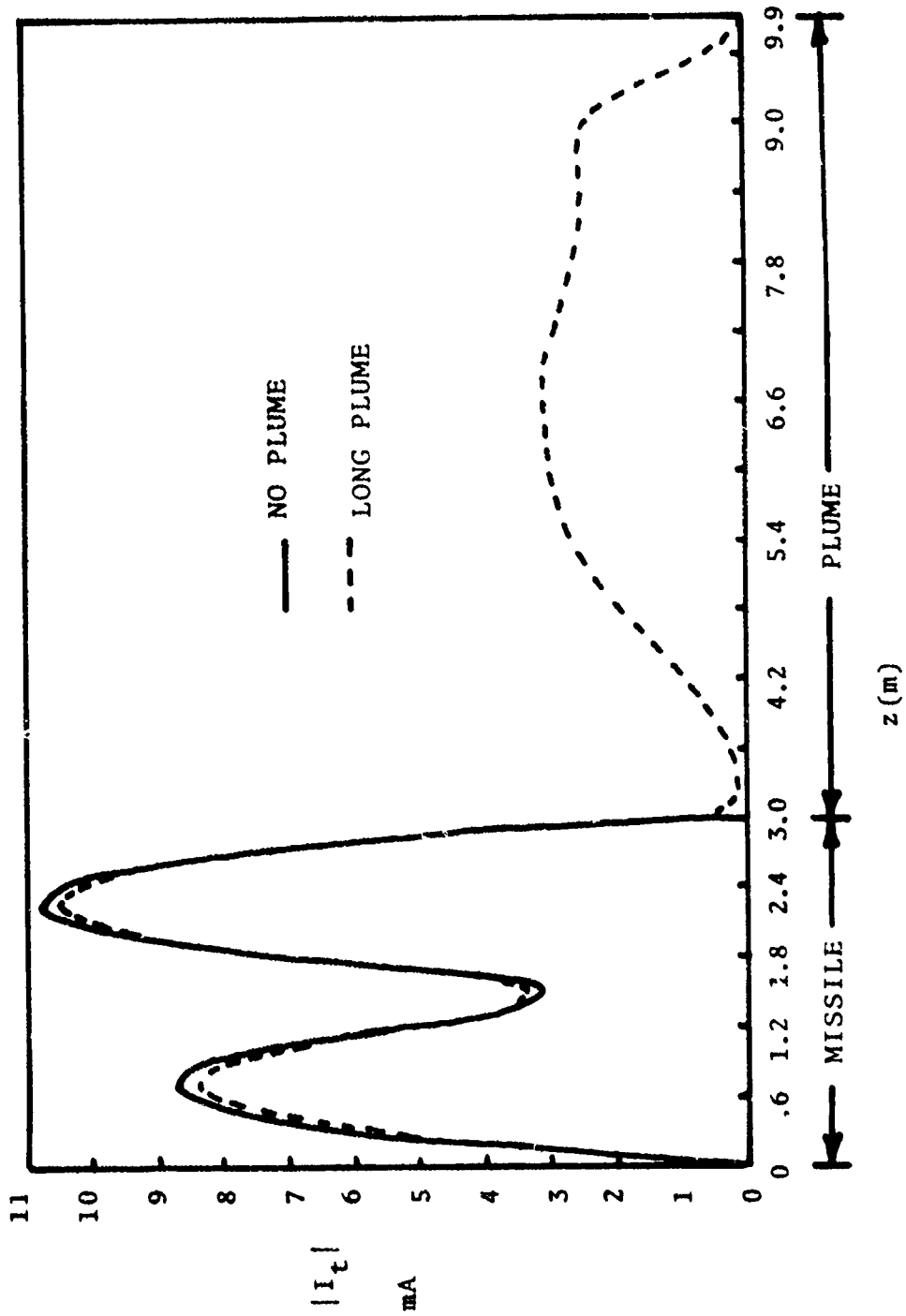


Figure 4.12b. Electric current distribution along a Chaparral missile and trailing plume, $f = 100$ MHz, $\theta_{inc} = 60^\circ$.

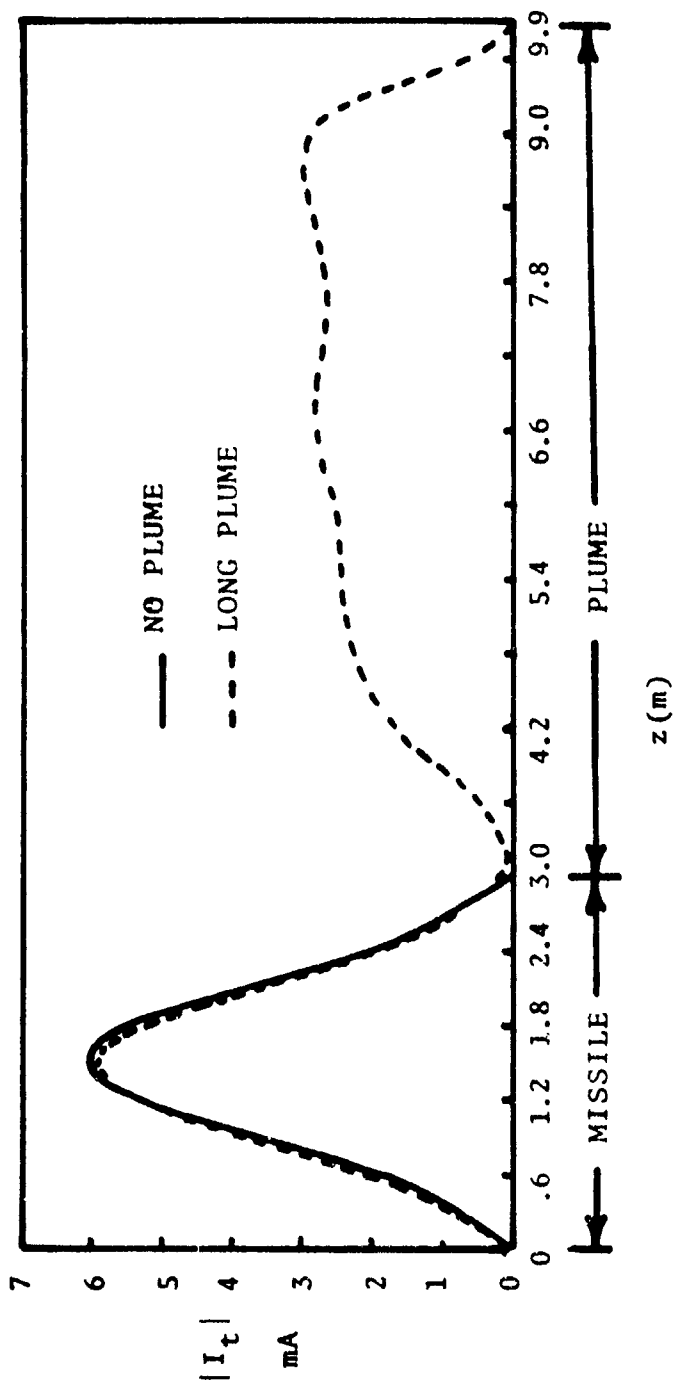


Figure 4.12c. Electric current distribution along a Chaparral missile and trailing plume, $f = 100$ MHz, $\theta_{inc} = 90^\circ$.

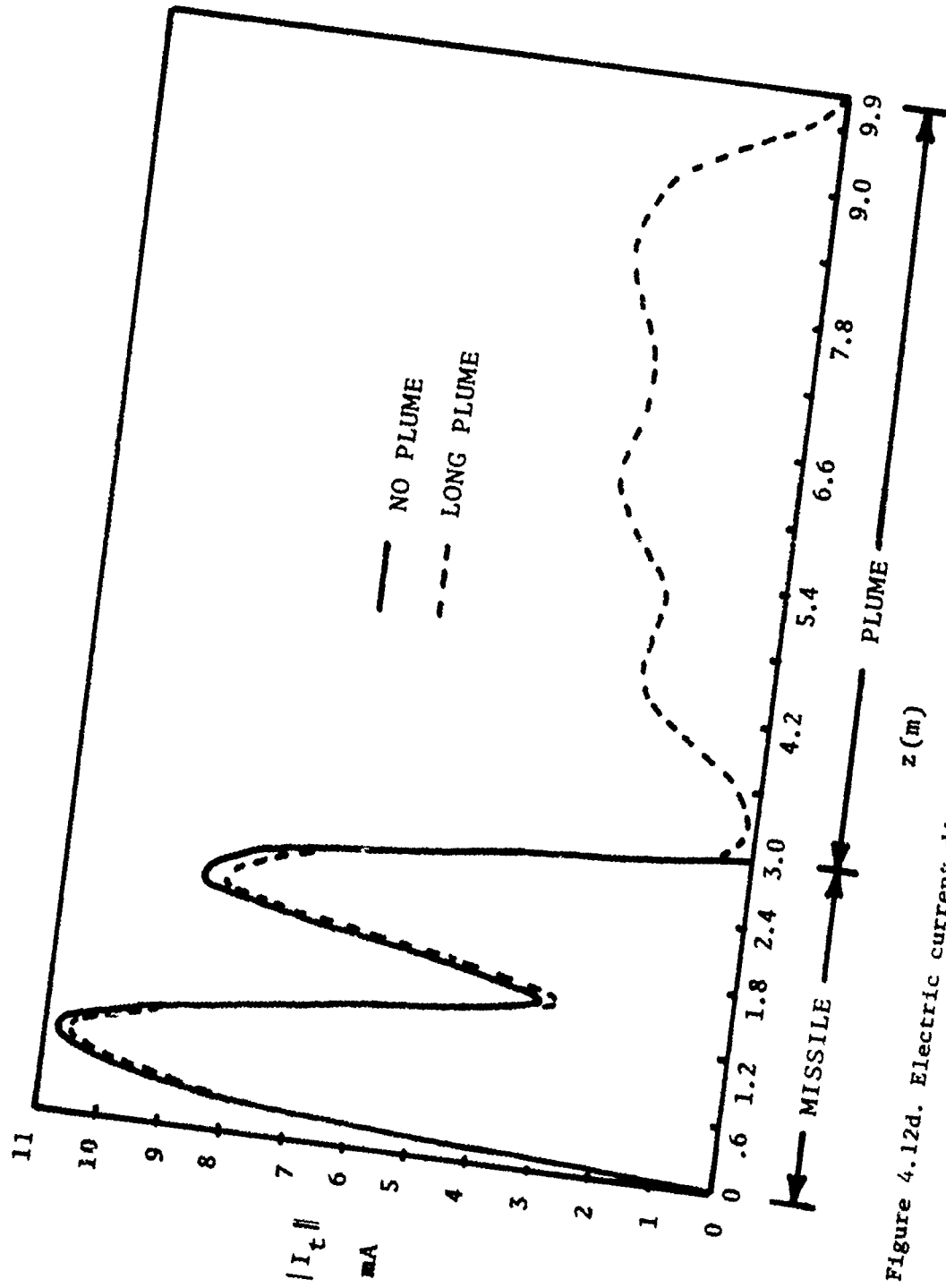


Figure 4.12d. Electric current distribution along a Chaparral missile and trailing plume, $f = 100$ MHz, $\theta_{inc} = 120^\circ$.

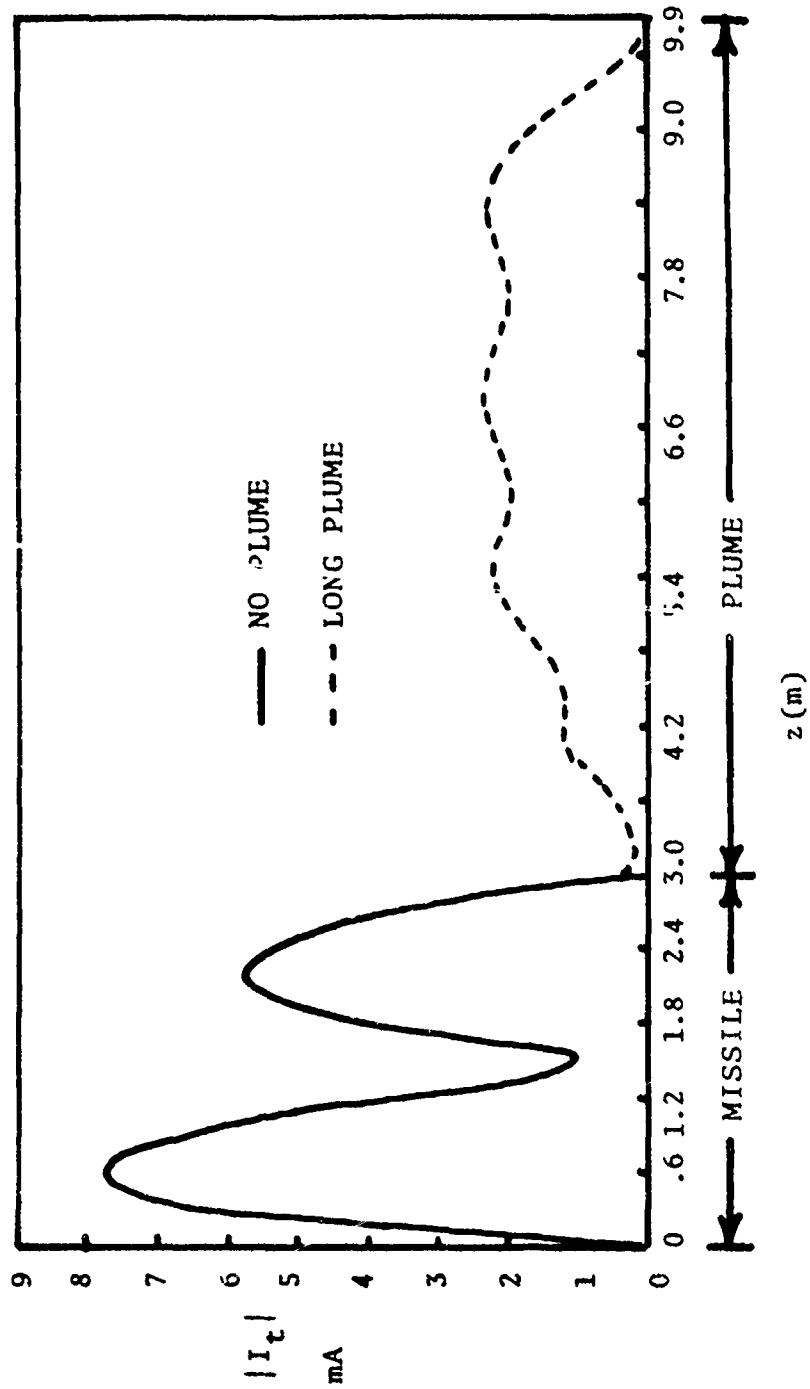


Figure 4.12e. Electric current distribution along a Chaparral missile and trailing plume, $f = 100$ MHz, $\theta_{inc} = 150^\circ$.

plume model situation. Due to the low conductivity in the plume around the nozzle region, the coupling between the missile and the plume will be low. Such an observation has been made by Wu et.al. [17]. For the short plume model case, we note that that the nozzle of the missile is now in a region of a higher conductivity than in the long plume model. The currents on the missile are now more affected by the presence of the plume. One notes that for angles of incidence grazing from the plume side, the currents on the missile can be more than the no plume case. One notes also that the current on the missile around the nozzle region is much higher than in the no plume or long plume cases. Thus coupling into the interior of the missile through apertures placed in the region around the nozzle of the missile will be greater in the short plume case than in the long plume case.

The currents on the plume appears to be comparable to the missile current at low frequencies. However, at frequencies above the first resonance, the current on the plume is generally much smaller than the missile current. For the 30MHz case, (see Figs. 4.8a through 4.8e), an interesting observation in the plume current is the peak occurring at about 3m from the junction and a shoulder which occurs at about 4.8m from the junction. One notes that the skin depths at this frequency and for the various conductivities involved are much

greater than the radial spread of the plume. Hence assuming a uniform current distribution across the cross-section of the plume, an "equivalent admittance", Y_{eq} , per unit length may be computed as follows:

$$Y_{eq} = \int_S \sigma \, dA ,$$

where σ is the value of the conductivity in the elementary area dA at the cross-sectional surface S at any point along the axis of the plume. Fig. 4.13 shows the variation of the equivalent admittance along the plume. One notes that the location of the peak and shoulder in the equivalent admittance variation roughly correspond to the peak and shoulder in the current on the plume.

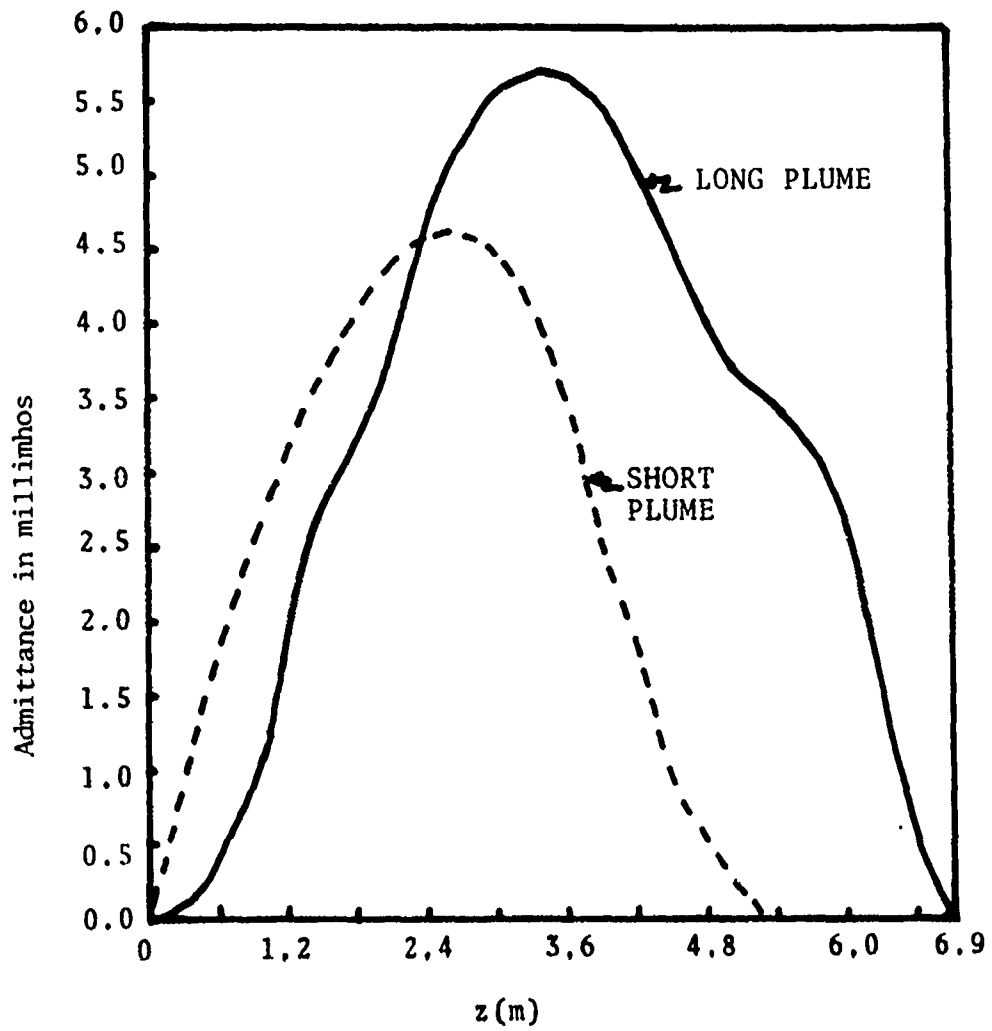


Figure 4.13. Equivalent admittance variation along the axis of the plume.

CHAPTER V

CONCLUSION

In this work, we are concerned with developing an approach for treating missiles with attached inhomogeneous conducting exhaust plumes. In Chapter II, a discussion of various approaches is presented and a detailed comparison of the unimoment method and the surface integral equation approach with a moment method solution has been given. It has been found that for thin and layered inhomogeneities, the surface integral equation approach is more efficient, while the unimoment method is more efficient for highly varying inhomogeneities and nearly circular objects. Since the objective here was to model and study a composite missile plume configuration wherein the axial length of the plume is large compared to its radial dimension, the surface integral equation approach was adopted. A computer code was then developed to compute currents induced on layered dielectric bodies of revolution. The validity of the computer code was then verified by comparing the computations with an eigenfunction formulation for concentric layered lossy dielectric spheres. The surface integral equation procedure was next

extended to the missile-plume problem and a simple approach for the numerical treatment of the missile/plume junction was developed and validated.

The computations on the layered model of the inhomogeneous plume have yielded results which are in good agreement with the surface impedance boundary condition approach used in [17]. However, the surface impedance boundary condition approach should be viewed with caution. This is because the assumed relationship between the electric and magnetic fields is true only for uniformly illuminated cylindrical structures and hence can be expected to be reasonably valid in regions only far away from the junction, while in the region around the junction serious errors may result which might alter the neighboring current distribution along the missile. Under such circumstances, the layered model approach should yield more accurate results. Cost of computations has precluded a more detailed analysis of the short plume model. Based on the good correspondence of the long plume model results obtained here and the long plume model results obtained in [17], it is believed that the currents on the missile under short plume model conditions would be more strongly affected by the presence of the plume.

In this work, the surface integral equation formulations used involve both the electric and magnetic field equations.

As shown in Appendix A, these problems can also be formulated in terms of the E-field alone or H-field equation alone or as a combination of both the E and H field equations to obtain a so-called combined field formulation. These approaches have been applied here only to homogeneous dielectric cylinders. However, they may be extended easily to three-dimensional bodies and may provide useful alternative approaches.

One worthwhile approach, which has not been considered here in the evaluation of methods for treating the missile/plume problem, is to couple an integral equation on the missile and plume boundaries with a finite element or finite difference solution of the fields in the inhomogeneous plume region. Such an approach, which has so far not been carried out, combines the best aspects of both the unimoment method and the surface integral equation approach and should be applicable to rather arbitrary shaped geometries and inhomogeneities. Furthermore, the approach also appears as an attractive method for analyzing coupling through apertures into the interior of missiles or other structures. In such problems, the exterior region is formulated by a surface integral equation, while the interior is formulated in terms of the appropriate wave equation. The two equations are

then coupled at the aperture with the appropriate boundary conditions.

APPENDIX A

SURFACE CURRENT FORMULATIONS FOR
DIELECTRIC SCATTERING PROBLEMS

Scattering by homogeneous dielectric bodies can be formulated via the surface equivalence principle. Application of the boundary conditions leads to a set of four integral equations involving the two unknown equivalent surface currents \bar{J} and \bar{M} . However, under suitable conditions, only two of the equations are sufficient to determine \bar{J} and \bar{M} . Thus various combinations of these four equations can be used, each combination leading to a different type of formulation. Some of the more important choices are described by Mautz and Harrington [10]. One common choice of the combination leads to the so-called PMCHW formulation described in [10]. Mautz and Harrington also point out that the so-called Müller formulation is related to the PMCHW formulation in that both approaches are special cases of a "combined field formulation." We consider here those combinations and further point out some features of combinations other than those considered in [10]. For the sake of

clarity and completeness, some of the material in [10] is repeated here.

A.1 Surface Integral Equation Formulation

Fig. A.1 depicts the homogeneous scatterer illuminated by an incident field $(\bar{E}^{inc}, \bar{H}^{inc})$. The body parameters are denoted by (μ_d, ϵ_d) , the fields inside, by (\bar{E}_d, \bar{H}_d) . The body is immersed in a medium characterized by parameters (μ_e, ϵ_e) . The straightforward application of the equivalence principle leads to the exterior and interior equivalences shown in Figs. A.2 and A.3 respectively. Equating to zero the tangential components of the null fields appearing in Figs. A.2 and A.3 leads to the following equations:

$$-\hat{n} \times \bar{E}_e^-(\bar{J}, \bar{M}) = \hat{n} \times \bar{E}^{inc}, \quad (A.1)$$

$$-\hat{n} \times \bar{H}_e^-(\bar{J}, \bar{M}) = \hat{n} \times \bar{H}^{inc}, \quad (A.2)$$

$$-\hat{n} \times \bar{E}_d^+(\bar{J}, \bar{M}) = 0, \quad (A.3)$$

$$-\hat{n} \times \bar{H}_d^+(\bar{J}, \bar{M}) = 0, \quad (A.4)$$

where \bar{E}_i, \bar{H}_i are the electric and magnetic fields due to \bar{J} and \bar{M} radiating in a medium (μ_i, ϵ_i) and $\bar{+}$ indicates

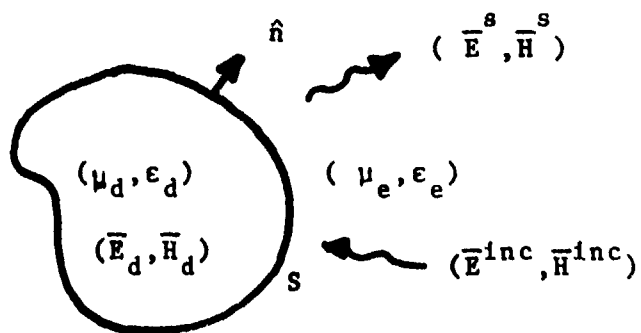


Figure A.1. A homogeneous dielectric scatterer.

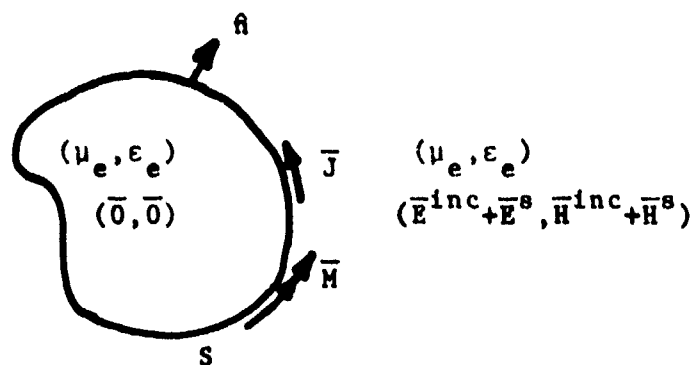


Figure A.2. External equivalence.

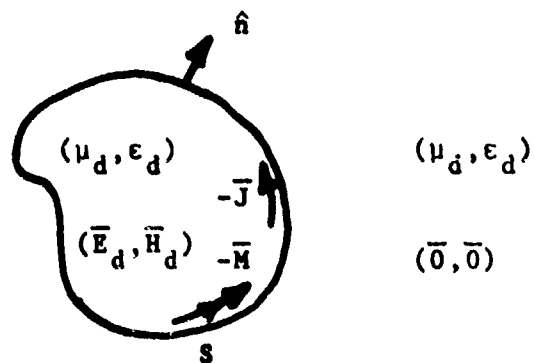


Figure A.3. Internal equivalence.

evaluation of the fields just inside and outside S , respectively. We note that (A.1) - (A.4) is a set of four equations in the two unknowns \bar{J} and \bar{M} . We need to reduce the number of equations to two and this can be done by appropriately selecting or combining the four equations in various ways. Some of the various possible combinations of (A.1) - (A.4) are as follows:

$$(a) \quad -\hat{n} \times (\bar{E}_e^- + \alpha \bar{E}_d^+) = \hat{n} \times \bar{E}^{inc}, \quad (A.5)$$

$$-\hat{n} \times (\bar{H}_e^- + \beta \bar{H}_d^+) = \hat{n} \times \bar{H}^{inc}, \quad (A.6)$$

$$(b) \quad -\hat{n} \times \bar{H}_e^- = \hat{n} \times \bar{H}^{inc}, \quad (A.7)$$

$$-\hat{n} \times \bar{H}_d^+ = 0, \quad (A.8)$$

$$(c) \quad -\hat{n} \times \bar{E}_e^- = \hat{n} \times \bar{E}^{inc}, \quad (A.9)$$

$$-\hat{n} \times \bar{E}_d^+ = 0, \quad (A.10)$$

$$(d) \quad -\hat{n} \times \bar{H}_e^- - \frac{\alpha}{\eta_e} \bar{E}_{e, \tan}^- = \hat{n} \times \bar{H}^{inc} + \frac{\alpha}{\eta_e} \bar{E}_{\tan}^{inc} \quad (A.11)$$

$$-\hat{n} \times \bar{H}_d^+ + \frac{\beta}{\eta_d} \bar{E}_{d, \tan}^+ = 0, \quad (A.12)$$

where α and β are arbitrary complex constants. The first type of combination in (a) above has been considered by Mautz and Harrington [10]. As they have pointed out, the choice of $\alpha = \beta = 1$ leads to the PMCHW formulation, while the choice of $\alpha = -(\epsilon_d/\epsilon_e)$, $\beta = -(\mu_d/\mu_e)$ leads to the Müller formulation. We designate combination (b) as the H-field formulation (HFIE), combination (c), the F-field formulation (EFIE), while (d) is called the combined field formulation (CFIE). It should be noted that the CFIE formulation presented here in (d) is different from the formulation (a) above, which was also called a "combined field formulation" by Mautz and Harrington [10]. Our CFIE formulation (d) is actually a generalization of their so-called combined field formulation for perfectly conducting scatterers [19]. Note that (d) combines two types of field quantities in each equality, whereas (a) combines the same type of fields from different regions. We consider in detail the combinations (b) - (d).

A.2 H-Field Formulation

The basic equations for this type of formulation are

$$-\hat{n} \times \bar{H}_e^-(\bar{J}, \bar{M}) = \hat{n} \times \bar{H}^{inc}$$

$$-\hat{n} \times \bar{H}_d^+(\bar{J}, \bar{M}) = 0.$$

Here, we have

$$\bar{H}_i(\bar{J}, \bar{M}) = -j\omega\bar{F}_i(\bar{M}) - \nabla\phi_i^m(\bar{M}) + \frac{1}{\mu_i} \nabla \times \bar{A}_i(\bar{J}), \quad (\text{A.13})$$

$$i = d \text{ or } e,$$

where $\bar{F}_i(\bar{M})$ is the electric vector potential due to the magnetic current \bar{M} in a medium characterized by the parameters (μ_i, ϵ_i) , $\phi_i^m(\bar{M})$ is the magnetic scalar potential due to \bar{M} in a medium characterized by the parameters (μ_i, ϵ_i) and $\bar{A}_i(\bar{J})$ is the magnetic vector potential due to the electric current in a medium characterized by the parameters (μ_i, ϵ_i) . Expressing the potentials in terms of the integrals over \bar{J} and \bar{M} , one obtains

$$(L_{HE}^e + \frac{I}{2}) \bar{J} + L_{HH}^e(\bar{M}) = \hat{n} \times \bar{H}^{inc}, \quad (\text{A.14})$$

$$(L_{HE}^d - \frac{I}{2}) \bar{J} + L_{HH}^d(\bar{M}) = 0, \quad (\text{A.15})$$

where

$$L_{HE}^i = \iint_S \bar{J} \times \nabla G_i \, ds$$

$$L_{HH}^i = -j\omega\epsilon_i \iint_S \bar{M} G_i \, ds' - \nabla \iint_S \frac{(\nabla' \cdot \bar{M})}{(-j\omega)} \frac{G_i}{\epsilon_i} \, ds' ,$$

$$i = d, e,$$

where G_i is the appropriate homogeneous Green's function for the medium with the parameters (μ_i, ϵ_i) . The notation for the operators above is as follows: the first subscript refers to the evaluation of the type of field, which in this case is the H-field, while the second subscript refers to the type of source, either electric (indicated by E), or magnetic (indicated by H). The superscripts d and e refer to the medium characterized by (μ_d, ϵ_d) and (μ_e, ϵ_e) , respectively. The factor $I/2$, where I denotes the identity operator, results from the evaluation of $\nabla \times \bar{A}$ on the surface of the scatterer. One may now use (A.14) and (A.15) to solve for \bar{J} and \bar{M} via moment method. An alternative approach would be to use (A.15) to express \bar{M} in terms of \bar{J} as

$$\bar{M} = (L_{HH}^d)^{-1} \left(\frac{I}{2} - L_{HE}^d \right) \bar{J} . \quad (A.16)$$

Using (A.16) in (A.14), one then obtains

$$\left[\frac{I}{2} + L_{HE}^e + L_{HH}^e (L_{HH}^d)^{-1} \left(\frac{I}{2} - L_{HE}^d \right) \right] \bar{J} = \hat{n} \times \bar{H}^{inc}. \quad (A.17)$$

Equation (A.17) can be used to solve for \bar{J} . Having determined \bar{J} , \bar{M} can then be obtained from (A.16). We point out that by storing the matrix $(L_{HH}^d)^{-1} \left(\frac{I}{2} - L_{HE}^d \right)$, which is computed in the process of determining \bar{J} , one may compute \bar{M} directly once \bar{J} has been determined.

It should be noted that expressing \bar{M} in terms of \bar{J} , as in (A.16), presupposes the existence of $(L_{HH}^d)^{-1}$. However, it can be shown (see [10]) that L_{HH}^d does not possess an inverse at frequencies corresponding to resonant frequencies of a conducting cavity formed by the closed surface S and filled with a material having electrical parameters (μ_d, ϵ_d) . One may, however, solve for \bar{J} and \bar{M} from (A.14) and (A.15) simultaneously at such frequencies [10]. We introduce here a terminology to describe these two approaches. Whenever \bar{J} and \bar{M} are simultaneously solved as in (A.14) and (A.15), we call the approach the two current formulation, while the use of (A.16) and (A.17), in which one solves for one current at a time, is called the single current formulation.

A.3 E-Field Formulation

The basic equations in this approach are

$$-\hat{n} \times \bar{E}_e^- = \hat{n} \times \bar{E}^{inc}$$

$$-\hat{n} \times \bar{E}_d^+ = 0.$$

Here we have

$$E_i = -j\omega\bar{A}_i(\bar{J}) - \nabla\phi_i^e(\bar{J}) - \frac{1}{\epsilon_i} \nabla \times \bar{F}_i(\bar{M}). \quad (A.18)$$

$i = d \text{ or } e.$

Expressing the potentials in terms of the currents, we have

$$L_{EE}^e(\bar{J}) + \left(\frac{1}{2} + L_{EH}^e \right) \bar{M} = \hat{n} \times \bar{E}^{inc}, \quad (A.19)$$

$$L_{EE}^d(\bar{J}) + \left(L_{EH}^d - \frac{1}{2} \right) \bar{M} = 0, \quad (A.20)$$

where

$$L_{EE}^i(\bar{J}) = -j\omega\mu_i \iint_S \bar{J}G_i ds' - \nabla \iint_S \frac{(\nabla' \cdot \bar{J})}{(-j\omega)} \frac{G_i}{\mu_i} ds',$$

$$L_{EH}^i(\bar{M}) = \iint_S \bar{M} \times \nabla G_i \, ds' ,$$

with the notations for the operators paralleling that of the H-field formulation. Proceeding in a manner similar to the H-field formulation, one obtains the single current E-field formulation as

$$\left[\frac{I}{2} + L_{EH}^e + L_{EE}^e (L_{EE}^d)^{-1} \left(\frac{I}{2} - L_{EH}^d \right) \right] \bar{M} = \hat{n} \times \bar{E}^{inc} , \quad (A.21)$$

with

$$\bar{J} = (L_{EE}^d)^{-1} \left(\frac{I}{2} - L_{EH}^d \right) \bar{M} . \quad (A.22)$$

As in the case of the H-field formulation, the single current E-field formulation fails at the interior resonant cavity frequencies. However, as before, one may adopt the two current approach of solving for \bar{J} and \bar{M} simultaneously from (A.19) and (A.20) at such frequencies.

A.4 Combined Field Formulation

The basic equations in this formulation are

$$-\hat{n} \times \bar{H}_e^- - \frac{\alpha}{\eta_e} \bar{E}_{e,tan}^- = \hat{n} \times \bar{H}^{inc} + \frac{\alpha}{\eta_e} \bar{E}_{tan}^{inc} ,$$

$$-\hat{n} \times \bar{H}_d^+ + \frac{\beta}{\eta_d} \bar{E}_{d,\tan}^+ = 0 ,$$

where η_e and η_d are the characteristic impedances of the exterior and interior medium respectively. Expressing the fields in terms of the currents \bar{J} and \bar{M} , we obtain the following equations:

$$\begin{aligned} & \left[\frac{I}{2} + L_{HE}^e + \frac{\alpha}{\eta_e} L_{EE}^e \right] \bar{J} + \left[L_{HH}^e + \frac{\alpha}{\eta_e} \left(\frac{I}{2} + L_{EH}^e \right) \right] \bar{M} \\ & = \hat{n} \times \bar{H}^{inc} + \frac{\alpha}{\eta_e} \bar{E}_{\tan}^{inc} , \end{aligned} \quad (A.23)$$

$$\left[-\frac{I}{2} + L_{HE}^d + \frac{\beta}{\eta_d} L_{EE}^d \right] \bar{J} + \left[L_{HH}^d - \frac{\beta}{\eta_d} \left(\frac{I}{2} - L_{EH}^d \right) \right] \bar{M} = 0, \quad (A.24)$$

where the operators are defined as before. A feature of this formulation is that the fields have been combined in a manner identical to that of the combined field formulation for conducting bodies proposed by Mautz and Harrington [19]. This fact makes it relatively easy to incorporate a solution procedure for both a dielectric object and a conducting object within the same computer program. This can be easily seen by noting that (A.23) becomes the combined field integral equation for a conducting scatterer [19], if one simply retains only terms involving the electric current on the

left hand side of the equation. Following [10], the permissible values of α and β can be determined by considering for what values of α and β the homogeneous equations

$$-\hat{n} \times \bar{H}_e^- - \frac{\alpha}{\eta_e} \bar{E}_{e,\text{tan}}^- = 0, \quad (\text{A.25})$$

$$-\hat{n} \times \bar{H}_d^+ + \frac{\beta}{\eta_d} \bar{E}_{d,\text{tan}}^+ = 0, \quad (\text{A.26})$$

have only the trivial solution. The first step in doing this is to show that $\bar{E}_{e,\text{tan}}^-$, $\bar{H}_{e,\text{tan}}^-$, $\bar{E}_{d,\text{tan}}^+$ and $\bar{H}_{d,\text{tan}}^+$ are all zero. For this, we consider first the complex power flow into the interior of surface S in the equivalent problem (A.25):

$$\begin{aligned} P_e &= \iint_S \bar{E}_e^- \times \bar{H}_e^{-*} \cdot (-\hat{n}) \, ds \\ &= \iint_S \bar{E}_e^- \cdot (\hat{n} \times \bar{H}_e^{-*}) \, ds \\ &= - \left(\frac{\alpha}{\eta_e} \right)^* \iint_S |\bar{E}_{e,\text{tan}}^-|^2 \, ds \\ &\quad - \left(\frac{\alpha}{\eta_e} \right)^* \iint_S |\bar{H}_{e,\text{tan}}^-|^2 \, ds, \quad (\text{A.27}) \\ &= - \frac{\iint_S |\bar{E}_{e,\text{tan}}^-|^2 \, ds + \iint_S |\bar{H}_{e,\text{tan}}^-|^2 \, ds}{|\alpha/\eta_e|^2} \end{aligned}$$

where (A.25) has been used in (A.27). We consider two cases:

- (1) The medium with parameters μ_e , ϵ_e is lossless. Then $\text{Re}(P_e) = 0$. But from (A.27), if $\text{Re}(\frac{\alpha}{\eta_e}) \neq 0$, we note $\bar{E}_{e,\text{tan}}^- = \bar{H}_{e,\text{tan}}^- = 0$.
- (2) The medium with parameters μ_e , ϵ_e is lossy. If $\text{Re}(P_e) = 0$, then by the uniqueness theorem [13], $\bar{E}_e = \bar{H}_e = 0$ interior to S . If we assume $\text{Re}(P_e) > 0$, we conclude $\bar{E}_{e,\text{tan}}^- = \bar{H}_{e,\text{tan}}^- = \bar{0}$. If $\text{Re}(\frac{\alpha}{\eta_e}) = 0$, then $\text{Re}(P_e) = 0$, and, as above, we obtain $\bar{E}_{e,\text{tan}}^- = \bar{H}_{e,\text{tan}}^- = 0$.

The argument above is also valid for the perfect conductor case and extends the allowable values of $\frac{\alpha}{\eta_e}$ beyond those considered in [19].

Next consider the complex power flow into the exterior of S in the equivalent problem (A.26):

$$\begin{aligned}
P_d &= \iint_S \bar{E}_d^+ \times \bar{H}_d^{+*} \cdot \hat{n} \, ds \\
&= - \iint_S \bar{E}_d^+ \cdot (\hat{n} \times \bar{H}_d^+)^* \, ds \\
&= - \left(\frac{\beta}{\eta_d} \right)^* \iint_S |\bar{E}_{d,\tan}^+|^2 \, ds \\
&\quad - \left(\frac{\beta}{\eta_d} \right)^* \iint_S |\bar{H}_{d,\tan}^+|^2 \, ds \\
&= \frac{\iint_S |\bar{E}_{d,\tan}^+|^2 \, ds + \iint_S |\bar{H}_{d,\tan}^+|^2 \, ds}{\left| \frac{\beta}{\eta_d} \right|^2} \quad , \quad (A.28)
\end{aligned}$$

where (A.26) has been used to obtain (A.28).

If $\text{Re}(P_d) = 0$, then $\bar{E}_d = \bar{H}_d = \bar{0}$ by the uniqueness theorem [13]. Thus, assume $\text{Re}(P_d) > 0$. Then if we choose $\text{Re}\left(\frac{\beta}{\eta_d}\right) > 0$, we conclude $\bar{E}_{d,\tan}^+ = \bar{H}_{d,\tan}^+ = \bar{0}$ from (A.28). Further, if $\text{Re}\left(\frac{\beta}{\eta_d}\right) = 0$, we have $\text{Re}(P_d) = 0$ and from the above argument $\bar{E}_d = \bar{H}_d = \bar{0}$.

To show next that $\bar{E}_{e,\tan}^- = \bar{E}_{d,\tan}^+ = \bar{H}_{e,\tan}^- = \bar{H}_{d,\tan}^+ = 0$ implies $\bar{J} = \bar{M} = 0$, we consider the exterior equivalence shown in Fig. A.4, wherein $\bar{E}_{e,\tan}^- = \bar{H}_{e,\tan}^- = \bar{0}$, but where we assume \bar{E}_e, \bar{H}_e outside the scatterer to be non-zero. Similarly for

the interior equivalence shown in Fig. A.5, we have $\bar{E}_{d,tan}^+$
 $= \bar{H}_{d,tan}^+ = 0$, but we assume \bar{E}_d, \bar{H}_d interior to the scatterer
to be non-zero. Since the interior fields in Fig. A-4 are
zero, we may change the internal medium to (μ_d, ϵ_d) (see Fig.
A.6). Similarly, in Fig. A.5, the exterior fields are zero
so that we may change the exterior medium to (μ_e, ϵ_e) (See
Fig. A.7). We note, however, that Figs. A.6 and A.7 depict
identical situations with regard to sources and media except
for the change in the sign of the sources. Hence, except
for the sign, the fields radiated by the currents should be
the same in both figures. Hence $(\bar{E}_e, \bar{H}_e) = (\bar{E}_d, \bar{H}_d) = (\bar{0}, \bar{0})$,
which implies, in turn, that

$$\bar{J} = \hat{n} \times \bar{H}_e^+ = \bar{0}$$

$$\bar{M} = -\hat{n} \times \bar{E}_e^+ = \bar{0}$$

Thus we have shown that (A.25) and (A.26) possess only
trivial solutions and hence that the solutions of (A.23) and
(A.24) are unique.

One may present a circuit analogy which helps to explain
the conditions on α and β . Referring to Figs. A.8 and A.9,
we may think of $Y_s^e = \frac{\alpha}{\eta_e}$ and $Y_s^d = \frac{\alpha}{\eta_d}$ as surface impedances

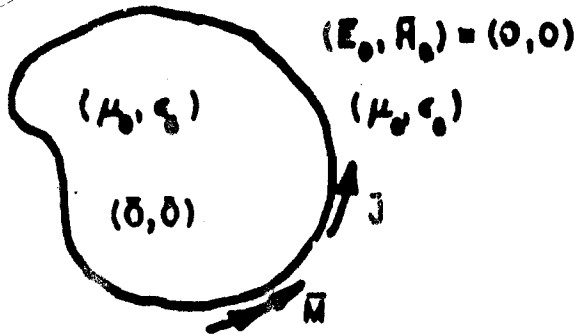


Figure A.4. Exterior equivalence with assumed non-zero fields in the exterior region.

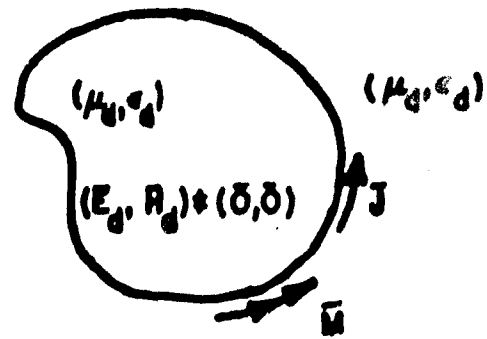


Figure A.5. Interior equivalence with assumed non-zero fields in the interior region.

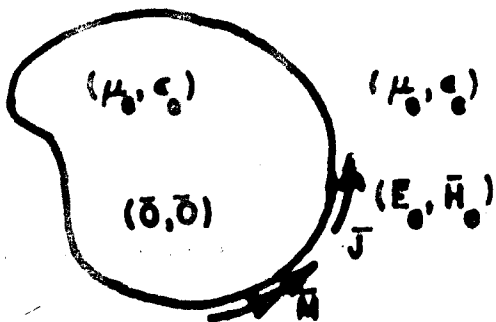


Figure A.6. Exterior equivalence with interior medium parameters (μ_d, ϵ_d) .

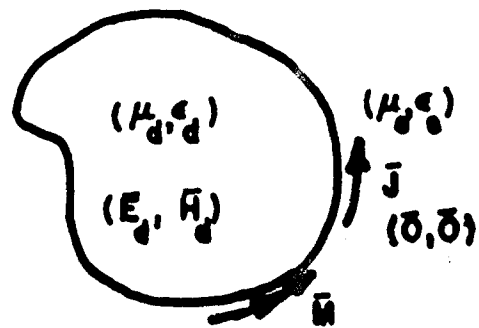


Figure A.7. Interior equivalence with exterior medium parameters (μ_0, ϵ_0) .

and (A.25) and (A.26) as surface impedance boundary conditions. The problem of determining whether or not there exist non-trivial solutions to (A.25) and (A.26) is thus one of deciding whether or not the internal or external regions can support a resonance when the region is bounded by the surface impedance Y_s^e or Y_s^d , respectively. For example, in the external resonance problem, since there is always some loss due to radiation, then if the surface is reactive or has a small loss ($\text{Re}(Y_s^e) \geq 0$), there can be no resonances. For the internal problem, if the medium is lossless, then no resonances are possible if $\text{Re}(Y_s^e) \neq 0$, since the surface is either lossy ($\text{Re}(Y_s^e) > 0$) and therefore the fields are damped, or supplies power to the interior region ($\text{Re}(Y_s^e) < 0$) and therefore the fields grow with time since there is no corresponding absorption mechanism. In the lossy case, however, we may not have internal resonances if $\text{Re}(Y_s^e) \geq 0$ because of internal and surface losses.

A.5 Application of Various Surface Integral Formulations to TM Scattering by Dielectric Cylinders

To illustrate some of the foregoing observations, we use the method of moments with some of the various formulations discussed here to solve scattering from a homogeneous dielectric cylinder excited in the TM polarization. Assuming

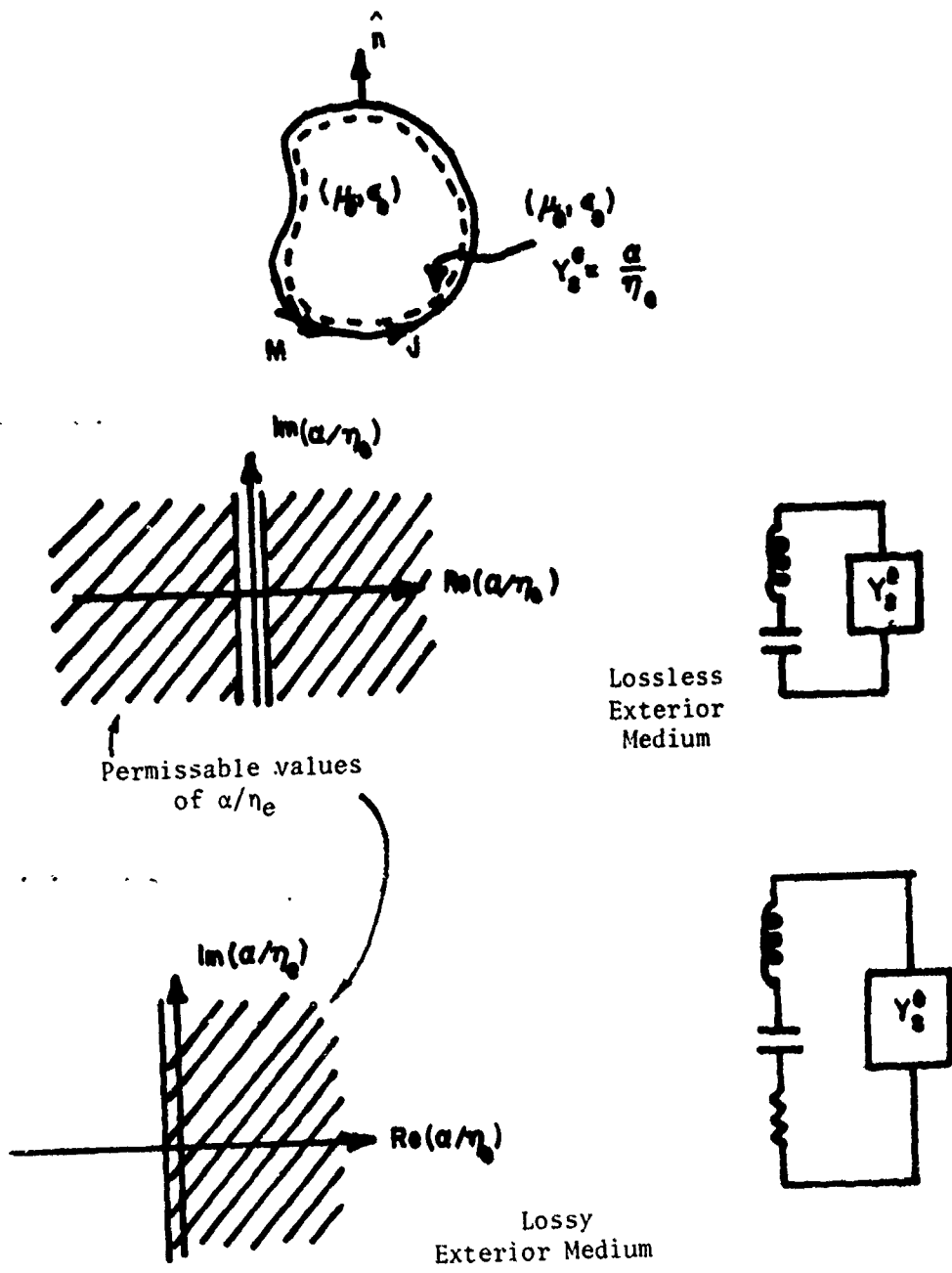


Figure A.8. Circuit analogy and permissible values of a/η_e for exterior equivalence.

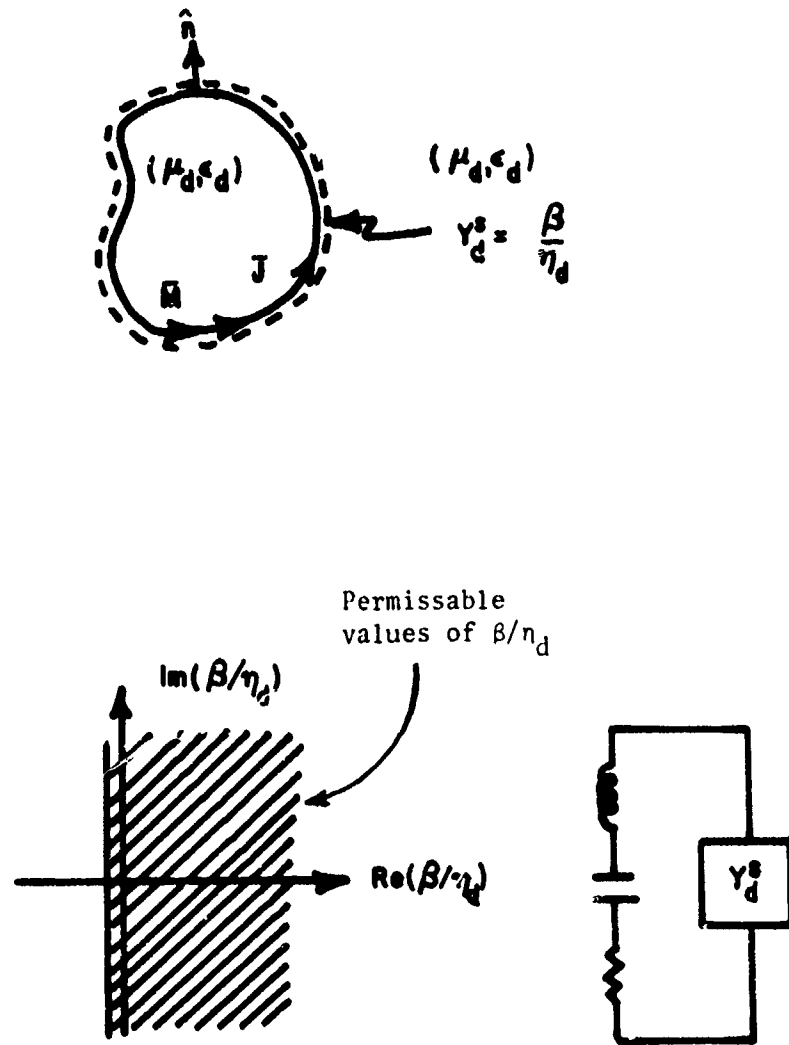


Figure A.9. Circuit analogy and permissible values of β/η_d for interior equivalence.

that the axis of the cylinder is along the z-direction (Fig. A. 10), we have

$$\bar{J} = J_z \hat{z} , \quad (\text{A.29})$$

$$\bar{M} = M_\tau \hat{\tau} , \quad (\text{A.30})$$

We note also that $\nabla' \cdot \bar{J} = 0$, since the cylinder is infinite in the z-direction. The various operators can now be written as

$$L_{EE}^i(\bar{J}) = \frac{\omega}{4} \int_C J_z \mu_1 H_0^{(2)}(k_1 |\bar{\rho} - \bar{\rho}'|) dc' , \quad (\text{A.31})$$

$$L_{EH}^i(\bar{M}) = \frac{1}{4j} \int_C M_\tau \frac{\partial}{\partial n'} H_0^{(2)}(k_1 |\bar{\rho} - \bar{\rho}'|) dc' , \quad (\text{A.32})$$

$$L_{HE}^i(\bar{J}) = \frac{1}{4j} \int_C J_z \frac{\partial}{\partial n} H_0^{(2)}(k_1 |\bar{\rho} - \bar{\rho}'|) dc' , \quad (\text{A.33})$$

$$\begin{aligned} L_{HH}^i(\bar{M}) &= \frac{\omega}{4} \int_C M_\tau \epsilon_1 H_0^{(2)}(k_1 |\bar{\rho} - \bar{\rho}'|) dc' \\ &+ \frac{1}{4\omega} \frac{\partial}{\partial \tau} \int_C \frac{\partial M_\tau}{\partial \tau} \frac{H_0^{(2)}(k_1 |\bar{\rho} - \bar{\rho}'|)}{\mu_1} dc' , \end{aligned} \quad (\text{A.34})$$

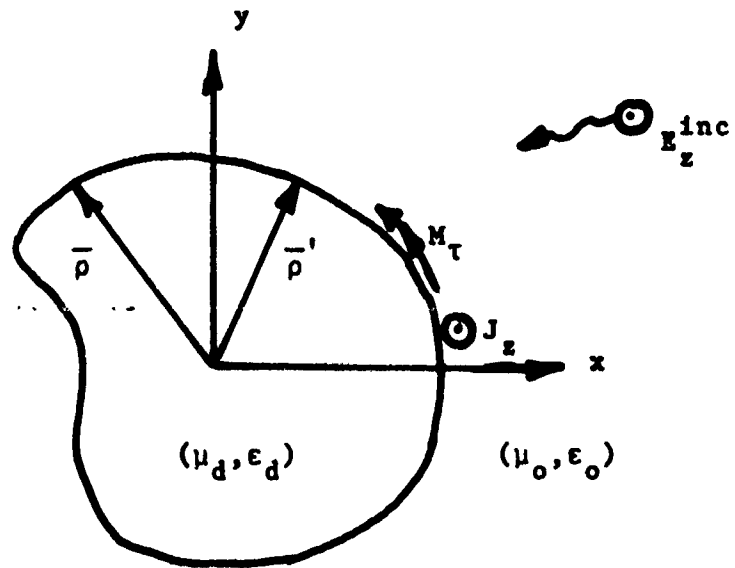


Figure A.10. Geometry of a homogeneous dielectric cylindrical scatterer.

where the two dimensional Green's function $\frac{1}{4j} H_0^{(2)}(k_i |\bar{\rho} - \bar{\rho}'|)$ for the medium with parameters (μ_i, ϵ_i) has been used, and $k_i = \omega \sqrt{\mu_i \epsilon_i}$, $i = d$ or e . $H_0^{(2)}(x)$ is the Hankel's function of second kind and zero order, $\bar{\rho}$ and $\bar{\rho}'$ correspond to field and source points, respectively.

In order to numerically approximate these operators, we divide the contour of the cylinder into a number of straight-line segments as shown in Fig. A.11. Pulse function basis sets are used to represent each of the currents over the subdomains. Thus the current is expanded as

$$J_z(t) = \sum_{n=1}^N J_n p_n(t) \quad , \quad (A.35a)$$

$$M_T(t) = \sum_{n=1}^N M_n p_n(t) \quad , \quad (A.35b)$$

where

$$p_n(t) = \begin{cases} 1, & t_{n-\frac{1}{2}} \leq t \leq t_{n+\frac{1}{2}} \\ 0, & \text{otherwise} \end{cases} \quad , \quad (A.36)$$

and t is the arc length along the cylinder contour. Using (A.35), the vector potential contributions in (A.31) - (A.34)

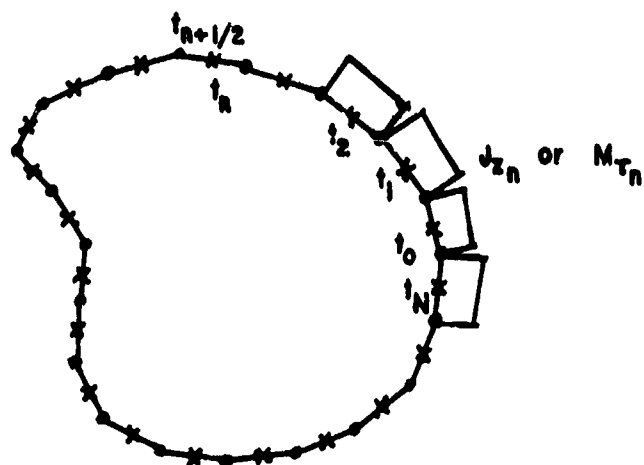


Figure A.11. Linear segmentation of the cross-section of the cylinder.

can be computed. In order to compute the scalar potential, we use a scheme similar to that of Glisson [11], wherein a pulse representation of the charge is derived from a finite difference approximation of the continuity equation. Thus we have

$$\rho_m(t) = \frac{j}{\omega} \frac{\partial M}{\partial \tau} = \frac{j}{\omega} \sum_{n=1}^{N+1} \frac{M_n - M_{n-1}}{t_n} p_{n-\frac{1}{2}}(t) \quad , \quad (\text{A.37})$$

where the charge pulses are defined as

$$p_{n-\frac{1}{2}}(t) = \begin{cases} 1, & t_{n-1} \leq t \leq t_n \\ 0, & \text{otherwise} \end{cases} \quad . \quad (\text{A.38})$$

A point matching testing procedure is used to evaluate the operators at the center of current pulses. The gradient term in (A.34) is evaluated by a finite differencing procedure as in [11]. By defining the "total" arc points, t_n of the contour to be at possible bends, the fields will always be matched away from points wherein fields may be singular. With the above expansion and testing procedures, the various operators may be approximated as follows:

$$[L_{EE}^i]_{mn} = \left\{ \begin{array}{l} \frac{\omega}{4} \int_{t_{n-\frac{1}{2}}}^{t_{n+\frac{1}{2}}} H_0^{(2)}(k_i |\bar{\rho} - \bar{\rho}'|) dc', \quad m \neq n \\ \\ \frac{\omega \mu_i}{2} \left[1 - j \frac{2}{\pi} \ln \left(\frac{\gamma k_i}{2} \right) \right] [t_{n+\frac{1}{2}} - t_{n-\frac{1}{2}}] \\ \\ - \frac{j \omega \mu_i}{2\pi} \left\{ t_n \ln \frac{(t_n - t_{n-\frac{1}{2}})}{(t_{n+\frac{1}{2}} - t_n)} + t_{n+\frac{1}{2}} [1 - \ln(t_n - t_{n-\frac{1}{2}})] \right. \\ \\ \left. - t_{n+\frac{1}{2}} [1 - \ln(t_{n+\frac{1}{2}} - t_n)] \right\}, \quad m = n \end{array} \right.$$

$$[L_{EH}^i]_{mn} = \left\{ \begin{array}{l} - \frac{1}{4j} \int_{t_{n-\frac{1}{2}}}^{t_{n+\frac{1}{2}}} k_i H_1^{(2)}(k_i |\bar{\rho}_m - \bar{\rho}'_n| \cos(\hat{n}', \bar{\rho}_m - \bar{\rho}'_n)) dc', \\ \\ 0, \quad m = n \end{array} \right. \quad m \neq n$$

$$[L_{HE}^i]_{mn} = \left\{ \begin{array}{l} - \frac{1}{4j} \int_{t_{n-\frac{1}{2}}}^{t_{n+\frac{1}{2}}} k_i H_1^{(2)}(k_i |\bar{\rho}_m - \bar{\rho}'_n| \cos(\hat{n}, \bar{\rho}_m - \bar{\rho}'_n)) dc', \\ \\ 0, \quad m = n \end{array} \right. \quad m \neq n$$

$$\begin{aligned}
 [L_{HH}^i]_{mn} = & \left\{ \begin{aligned}
 & \left[\frac{\omega}{4} \int_{t_{n-\frac{1}{2}}}^{t_{n+\frac{1}{2}}} \epsilon_i H_o^{(2)}(k_i |\bar{\rho}_m - \bar{\rho}'_n|) dc' \right] \\
 & + \frac{1}{(\Delta_m + \Delta_{m+1})} \left\{ \frac{1}{\Delta_n} \int_{t_{n-1}}^n \left[\frac{H_o^{(2)}(k_i |\bar{\rho}_{m+\frac{1}{2}} - \bar{\rho}'_n|)}{\mu_i} \right. \right. \\
 & - \left. \left. \frac{H_o^{(2)}(k_i |\bar{\rho}_{m-\frac{1}{2}} - \bar{\rho}'_n|)}{\mu_i} \right] dc' \right. \\
 & - \frac{1}{\Delta_{n+1}} \int_{t_n}^{t_{n+1}} \left[\frac{H_o^{(2)}(k_i |\bar{\rho}_{m+\frac{1}{2}} - \bar{\rho}'_n|)}{\mu_i} \right. \\
 & \left. \left. - \frac{H_o^{(2)}(k_i |\bar{\rho}_{m-\frac{1}{2}} - \bar{\rho}'_n|)}{\mu_i} \right] dc' \right\} , m \neq n \\
 & C_1 - C_2 + C_3 + C_4 + C_5 + C_6 , m = n,
 \end{aligned} \right.
 \end{aligned}$$

where

$$C_1 = \frac{\omega}{4} \left[\epsilon_i \left(1 - j \frac{2}{\pi} \ln \frac{\gamma k_i}{2} \right) \right] [t_{n+\frac{1}{2}} - t_{n-\frac{1}{2}}]$$

$$\begin{aligned}
 C_2 = & - \frac{j\omega}{2\pi} \epsilon_i \left\{ t_n \ln \left(\frac{t_n - t_{n-\frac{1}{2}}}{t_{n+\frac{1}{2}} - t_n} \right) + t_{n-\frac{1}{2}} [1 - \ln(t_n - t_{n-\frac{1}{2}})] \right. \\
 & \left. - t_{n+\frac{1}{2}} [1 - \ln(t_{n+\frac{1}{2}} - t_n)] \right\}
 \end{aligned}$$

$$C_3 = \frac{1}{4\omega\mu_0\Delta_n} \int_{t_{n-1}}^{t_n} H_0^{(2)}(k_1 |\bar{\rho}_{n+\frac{1}{2}} - \bar{\rho}'_n|) dc'$$

$$C_4 = \frac{1}{4\omega\mu_0\Delta_{n+1}} \int_{t_n}^{t_{n+1}} H_0^{(2)}(k_1 |\bar{\rho}_{n-\frac{1}{2}} - \bar{\rho}'_n|) dc'$$

$$C_5 = -\frac{1}{4\omega\mu_1} \left(1 - j \frac{2}{\pi} \ell_n \frac{\gamma k_1}{2}\right) + \frac{j}{2\pi\omega\mu_0} \left(\ell_n \frac{\Delta_n}{2} - 1\right)$$

$$C_6 = -\frac{1}{4\omega\mu_1} \left(1 - j \frac{2}{\pi} \ell_n \frac{\gamma k_1}{2}\right) + \frac{j}{2\pi\omega\mu_0} \left(\ell_n \frac{\Delta_{n+1}}{2} - 1\right).$$

Computer program subroutines for the evaluation of each of the operators L_{EE} , L_{EH} , L_{HE} and L_{HH} were written and combined in the appropriate manner depending on the type of formulation used. In Fig. A.12 is shown the currents on a circular cylinder as found by the various methods. Also shown is the exact eigenfunction solution. Fig. A.13 depicts the currents on a square cylinder of side $2a$. Since the single current formulation leads to erroneous results at the resonant frequencies of the interior region, a plot of the determinant of the moment matrix vs. ka is shown in Fig. A.14. We note that both E and H types of formulations indicate a sharp dip in the value of the determinant at the

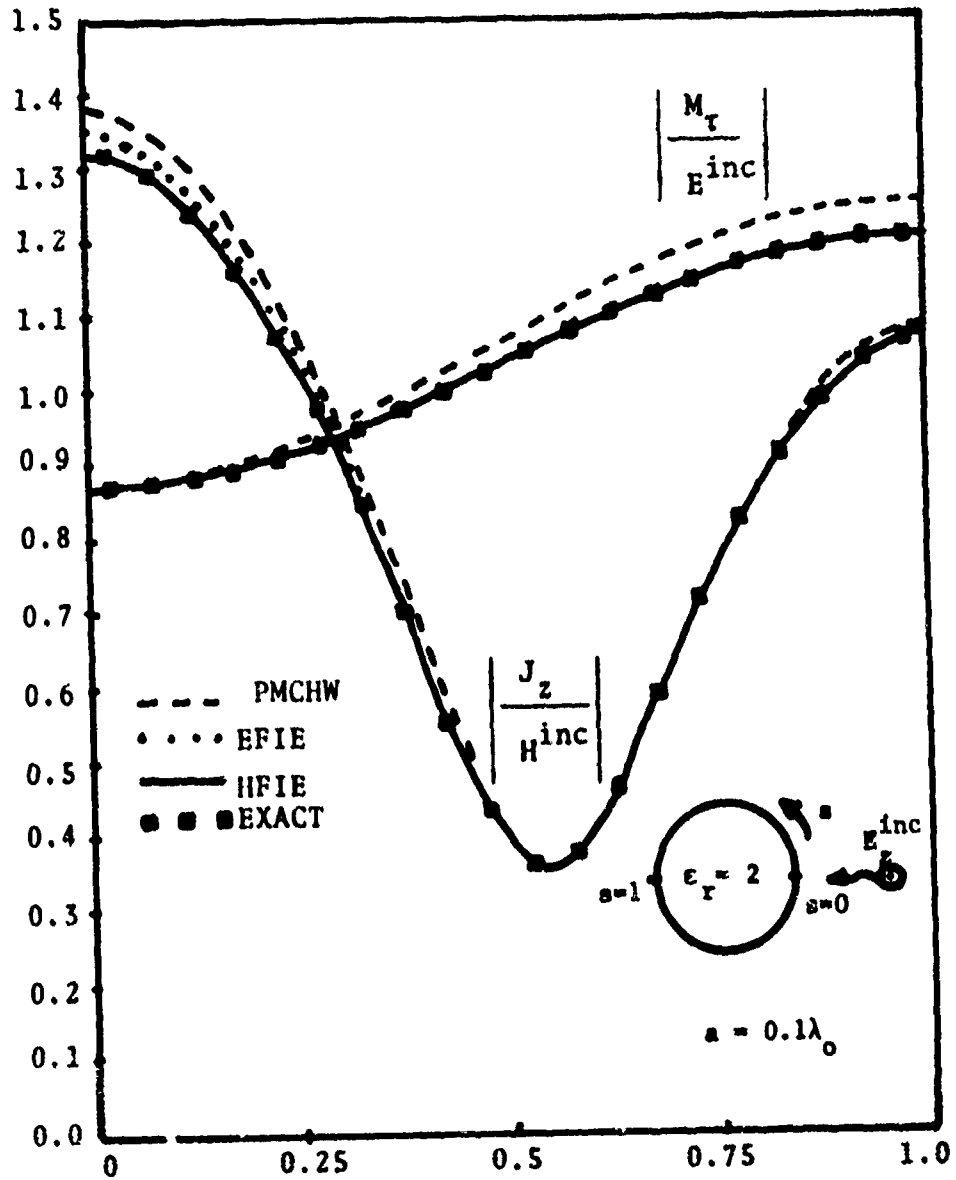


Figure 7.12. Electric and magnetic current distribution along a circular cylinder excited by a TM polarized incident wave, $a = 0.1\lambda_0$, $\epsilon_r = 2.0$.

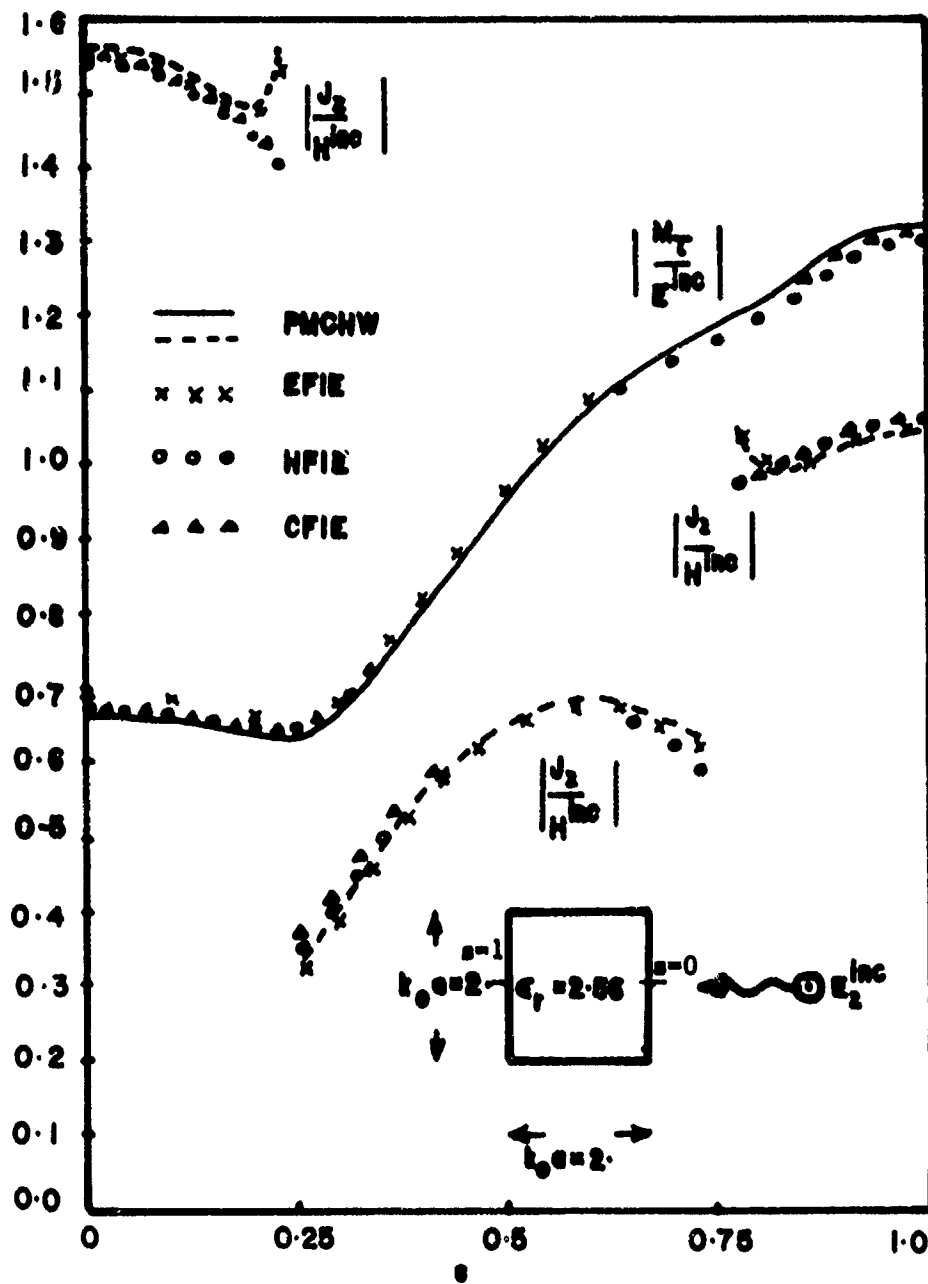


Figure A.13. Electric and magnetic current distribution along a square cylinder excited by a TM wave.

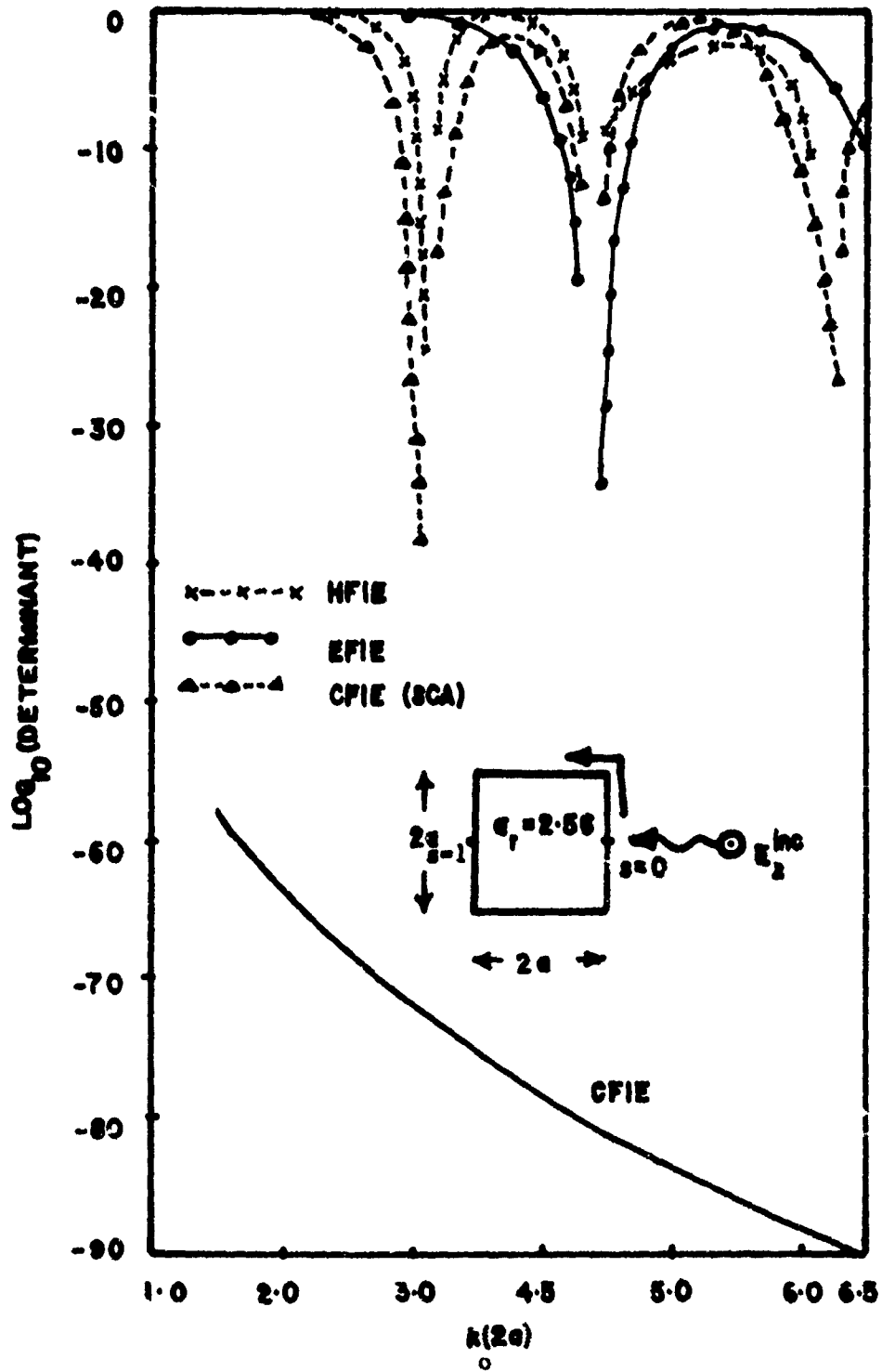


Figure A.14. Determinant of the moment matrix vs. $k_0(2a)$

resonant frequencies, which are the cut off frequencies for modes of the square waveguide filled with a dielectric with $\epsilon_r = 2.56$. The combined field formulation when solved by the single current approach, also shows the resonance effect. This is because the operators on \bar{J} and \bar{M} , which otherwise could be used to express \bar{J} in terms of \bar{M} or vice versa, do not possess an inverse at these resonant frequencies. However, when one solves (A.23) and (A.24) simultaneously one avoids this difficulty as shown by the plot of the determinant of the CFIE matrix.

REFERENCES

- [1] R. F. Harrington, *Field Computation by Moment Methods*, New York: Macmillan, 1968.
- [2] P. C. Waterman, "Scattering by Dielectric Obstacles," *Alta Frequenza*, vol. 38, (Speciale), p. 348, 1969.
- [3] K. K. Mei, "Unimoment Method of Solving Antenna and Scattering Problems," *IEEE Trans. Antennas and Propagation*, vol. AP-22, pp. 760-766, Nov. 1974.
- [4] R. J. Pogorzelski, "On the Numerical Computation of Scattering from Inhomogeneous Penetrable Objects," *IEEE Trans. Antennas and Propagation*, vol. AP-26, pp. 616-618, July 1978.
- [5] B. Peterson and S. Ström, "T-matrix Formulation of Electromagnetic Scattering from Multilayered Scatterers," *Physical Review D*, vol. 10, pp. 2670-2684, 15 October 1974.
- [6] S. Ström, "T Matrix for Electromagnetic Scattering from an Arbitrary Number of Scatterers with Continuously Varying Electromagnetic Properties," *Physical Review D*, vol. 10, pp. 2685-2690, 15 October 1974.
- [7] S. K. Chang and K. K. Mei, "Application of the Unimoment Method to Electromagnetic Scattering of Dielectric Cylinders," *IEEE Trans. Antennas and Propagation*, vol. AP-24, pp. 35-41, Jan. 1976.
- [8] M. A. Morgan, "Numerical Computation of Electromagnetic Scattering by Inhomogeneous Dielectric Bodies of Revolution," Ph.D. Dissertation, University of California, Berkely, California, 1976.
- [9] O. C. Zienkiewicz, *The Finite Element Method in Engineering Science*, London: McGraw Hill, 1971.

- [10] J. R. Mautz and R. F. Harrington, "Electromagnetic Scattering from a Homogeneous Body of Revolution, Report TR-77-10, Department of Electrical and Computer Engineering, Syracuse University, Syracuse, New York, November 1977.
- [11] A. W. Glisson, Jr., "On the Development of Numerical Techniques for Treating Arbitrarily-Shaped Surfaces," Ph.D. Dissertation, University of Mississippi, University, Mississippi, June 1978.
- [12] Y. Chang and R. F. Harrington, "A Surface Formulation for Characteristic Modes of Material Bodies," Technical Report No. 2, Contract No. N00014-67-A-0378-0006 for the Department of the Navy, Syracuse University, Syracuse, New York, October 1974.
- [13] R. F. Harrington, *Time Harmonic Electromagnetic Fields*, New York: McGraw Hill, 1961.
- [14] T. K. Wu, "Electromagnetic Scattering from Arbitrarily-Shaped Lossy Dielectric Bodies," Ph.D. Dissertation, University of Mississippi, University, Mississippi, May 1976.
- [15] R. W. P. King and T. T. Wu, *The Scattering and Diffraction of Waves*, Harvard Press, Cambridge, Mass., 1959.
- [16] A. W. Glisson, Jr., Private Communication.
- [17] T. K. Wu, D. R. Wilton and L. L. Tsai, "Effects of Various Exhaust Plume Models on Missile Skin Currents," Technical Report under preparation for the Rome Air Development Center under the Post-Doctoral Program Grant No. GIT 8-E-21-626.
- [18] J. D. Nordgard and G. S. Smith, "A Plasma Model of Missile Exhaust Plumes," Report RADC-TR-77-144 for Rome Air Development Center, Georgia Institute of Technology, Atlanta, Georgia, April, 1977, A040057.
- [19] J. R. Mautz and R. F. Harrington, "H-Field, E-Field and Combined-Field Solutions for Conducting Bodies of Revolution," *AEU*, vol. 32. no. 4, pp. 157-164, April, 1978.



MISSION
of
Rome Air Development Center

RADC plans and executes research, development, test and selected acquisition programs in support of Command, Control Communications and Intelligence (C³I) activities. Technical and engineering support within areas of technical competence is provided to ESD Program Offices (POs) and other ESD elements. The principal technical mission areas are communications, electromagnetic guidance and control, surveillance of ground and aerospace objects, intelligence data collection and handling, information system technology, ionospheric propagation, solid state sciences, microwave physics and electronic reliability, maintainability and compatibility.